



UNIVERSITÉ DE STRASBOURG

ÉCOLE DOCTORALE PHYSIQUE ET CHIMIE PHYSIQUE (ED 182)

ICS UPR-22 CNRS

THÈSE présentée par :

Georges WEBER

soutenue le : 17 septembre 2012

pour obtenir le grade de : **Docteur de l'université de Strasbourg**

Discipline/ Spécialité : Physique

**Modifications photo-induites de
membranes modèles**

THÈSE dirigée par :

M. CHARITAT Thierry

Professeur, Université de Strasbourg

RAPPORTEURS :

Mme. BASSEREAU Patricia

Professeur, Institut Curie, Paris

M. RAMSEYER Christophe

Professeur, Université de Franche-Comté

AUTRES MEMBRES DU JURY :

M. MELY Yves

Professeur, Université de Strasbourg

M. BAGATOLLI Luis

Professeur, University of Southern Denmark

Photo-induced modifications of model membranes

Dissertation by

Georges Weber

September 17, 2012

PhD committee:

President:	M. Yves MÉLY
Rapporteur:	Mme. Patricia BASSEREAU
Rapporteur:	M. Christophe RAMSEYER
Examiner:	M. Luis BAGATOLLI
Supervisor:	M. Thierry CHARITAT
Invited member:	M. André SCHRODER
Invited member:	M. Carlos MARQUES

Acknowledgments

I would like to express here my deepest appreciation to all those that helped and supported me, thus contributing to the completion of my PhD.

This PhD work emerged from a collaboration between the Institut Charles Sadron (ICS) in Strasbourg and the São-Paulo University in Brazil. I would like to thank Jean-François Legrand and Jean-Michel Guenet, the successive directors of the ICS, for having given me the opportunity to work in their laboratory. I am deeply thankful to Maurício Baptista for inviting me to spend two weeks in his group in Brazil.

I would like to thank my PhD committee for the interest they showed in my work: Yves Mély who presided over my jury, Patricia Bassereau and Christophe Ramseyer for having accepted to be examiners of my thesis and Luis Bagatolli for his enthusiastic comments.

As if one was not enough, I got the chance to have three supervisors during my thesis: Thierry Charitat, Carlos Marques and André Schroder. I want to thank them for the trust and freedom they accorded me during these three years but also for their support, their ideas and the fruitful discussions that guided me through my research; it was the perfect balance. I learned a lot during these years about membranes, oxidation, experimental techniques...

and also about rugby: I (and my washing machine) thank the “Tuesday lunch time” rugby team for the chance to let off some steam, always in a clean way! I also really appreciated the babyfoot sessions with Magalie, Pierre, Thierry, Vincent... and leave my place to the “Nintendo” generation now.

Thanks to all colleagues from M³, and to all the people from ICS that contributed to the work or to the fun (or both) in this three years. Especially my office colleagues: Andreas, Constantin and Jean, as well as Philippe, Laure, Arnaud, Martin and the many others I had the pleasure to meet.

A special thanks to Maurício and his team in São-Paulo: Helena, Chris, Isabel... for their warm welcome and the experiments performed together. Thanks to Adjaci for the Chlorin-12 molecule which I played with during my thesis and also for showing me the Brazilian countryside!

And of course, infinite thanks go to my family for their kind support in every way. Special thanks to my parents, Sophie, Aurélie, Freddy, Denise, Jean-Marc and Marguerite, who made my PhD celebration a full success.

Contents

Introduction	1
1 State of the art	5
1.1 Light-Matter interaction	5
1.1.1 Absorption of light	5
1.1.2 De-excitation processes	11
1.1.3 Energy Transfer	13
1.2 Oxidation in living systems	15
1.2.1 Lipid peroxidation: natural consequences of life with oxygen .	15
1.2.2 Effects on membrane physical properties and protein function	16
1.2.3 Cell defense mechanisms	17
1.3 Photodynamic therapy	18
1.3.1 Clinical status	18
1.3.2 Biological targets	20
1.3.3 Photosensitizers, light sources and tissue optics	21
1.3.4 Mechanisms	23
1.3.5 PDT Dosimetry	27
1.3.6 Future developments	30
1.3.7 Conclusion	32

1.4	Effects on membranes	33
1.4.1	Different oxidation pathways	33
1.4.2	Membrane integrity and permeation	36
1.4.3	Modification in preferred lipid area	40
1.4.4	Oxidation efficiency	43
1.4.5	Other studies in the field	44
1.5	Conclusion	45
2	Systems and techniques	47
2.1	Membranes	47
2.1.1	Amphiphilic molecules	49
2.1.2	Self-Assembly	51
2.2	Model systems	54
2.2.1	Lipid monolayers	54
2.2.2	The lipid bilayer	55
2.3	Bilayer properties and micropipette experiments	58
2.3.1	Lipids on the move	58
2.3.2	Membrane permeability	59
2.3.3	Membrane deformation modes	59
2.3.4	Micropipette suction experiments	64
2.4	Microscopy	69
2.4.1	Experimental setup	69
2.4.2	Power measurement by chemical actinometry	69
2.4.3	Data analysis	71
3	Chlorin-12: A new photosensitizer	75
3.1	Photophysical and photochemical properties	76

3.1.1	Triplet state lifetime	76
3.1.2	Singlet Oxygen Luminescence (SOL) measurement	77
3.2	Chlorin-12 anchored in membranes	77
3.2.1	Homogeneous incorporation	77
3.2.2	Singlet oxygen production	79
3.2.3	Chlorin-12 diffusion coefficient in fluid membranes	80
3.3	Behavior under light exposure	81
3.3.1	PS chemical modification and photobleaching	82
3.3.2	Re-absorption model	86
3.3.3	Discussion	89
3.3.4	Singlet oxygen quantum yield	91
3.4	Conclusions	91
4	Quantifying photo-oxidation in lipid bilayers	93
4.1	Hydroperoxidation of Giant Unilamellar Vesicles	93
4.2	Molecular area increase	95
4.2.1	Experimental setup	95
4.2.2	Control Experiments	95
4.2.3	Full lipid conversion	98
4.2.4	Discussion	100
4.3	Chlorin-12 concentration and irradiation power dependence	101
4.3.1	Chlorin-12 concentration dependence	101
4.3.2	Irradiation power dependence and singlet oxygen depletion	101
4.4	Efficiency of the hydroperoxidation reaction	103
4.4.1	Efficiency per unsaturated bond: a well defined binary process	104
4.4.2	Comparison with bulk reaction constants	105

4.4.3	Evolution at high Chlorin-12 contents	106
4.5	Modifications of the mechanical properties of the membrane	107
4.5.1	Preliminary observations	108
4.5.2	Stretching modulus evolution upon oxidation	109
4.5.3	Discussion	110
4.6	Conclusion	111
5	Complementary studies	113
5.1	Effect of a singlet oxygen quencher	113
5.1.1	Bulk quencher inefficient against surface generated $^1\text{O}_2$	114
5.1.2	Triplet state lifetime	115
5.1.3	Singlet oxygen Lifetime	116
5.1.4	Simple model based on diffusion	117
5.1.5	Singlet oxygen distribution under continuous irradiation	119
5.1.6	Conclusion	121
5.2	A monolayer study	122
5.2.1	Isotherms of POPC/POPC-OOH mixtures	122
5.2.2	Lipids at air-water interface: isotherm evolution	124
5.2.3	Conclusion	128
	General conclusion	129
	General conclusion	129
	Appendix	133
A.1	Analysis of the FRAP under microscope	133
A.2	Synthesized molecules	135
A.2.1	Photosensitizer	135

A.2.2	Hydroperoxidized lipid POPC-OOH	137
A.3	Microscope filters	138
A.4	Vesicles formation	139
A.4.1	GUV electroformation	139
A.4.2	Liposome extrusion	139

Introduction

Lipid oxidation plays a central role in the life of the eukariotic cells, where it is a direct consequence of the reactive oxygen species generated by mitochondrial respiration, but also by many other processes such as inflammation, catalysis by peroxisomal oxidases, virus phagocytosis, ultraviolet and ionic irradiation, to name only a few [1–3]. A controlled amount of oxidized lipids is required for cell signaling, cell maturation and differentiation and cell apoptosis. However, the products of lipid oxidation, if uncontrolled, can have a deleterious effect on the functioning of the cell, and are known to be involved in a variety of diseases including Parkinson’s and Alzheimer’s neuro-degenerations, hypertension and cancer [4, 5].

Lipid oxidation plays also a key role in Photodynamic Therapy (PDT), a technique clinically used in pathologies such as skin or oesophagus cancer, where tumors are destroyed by intense light-induced tissue oxidation [6–8]. The method relies on the administration of a photosensitizer molecule that is suitable to induce the formation of singlet oxygen ($^1\text{O}_2$), a powerful oxidizing agent, able to cause necrosis or apoptosis in cancer cells [9]. Cell membranes and especially unsaturated phospholipids are the prime targets of $^1\text{O}_2$. However, the fundamental mechanisms by which lipid oxidation influences the structure of the lipid self-assembled bilayer are still poorly understood. As several experiments report modifications on permeability, fluidity, packing order, bilayer thickness and vesicle destruction [10–16], there is no consensus among all these observations and elucidation of the molecular basis of cell signaling under lipid oxidation is therefore compromised. Furtherance has also been hindered by the extended complexity of the possible oxidation pathways, as unsatisfactory identification of the proper mechanisms leads to apparently contradictory conclusions from similar experiments.

Our contribution to research in this area is based on the central intuition that progress can only be achieved in new biomimetic membrane systems where the

spatial localization of the oxidation events might be controlled and monitored. Accordingly, we have developed new photosensitizer agents [17] that can be anchored in Giant Unilamellar Vesicles (GUVs). It is important to stress that progress in the control of the spatial distribution of oxidation allows also for a selection of the oxidation pathways, as we show in this study for the particular case of hydroperoxidation. In association with new tools for the quantification of the oxidation events, these new models have provided a complete scenario for the hydroperoxidation mechanisms, from the production of the oxidant species to the final chemical and physical modifications induced on the self-assembled bilayers.

In a first chapter we review the basic concepts of light interaction with molecules. Then, we discuss the importance of oxidation in living systems and explain how PDT can be used to treat several cancers and the different underlying mechanisms involved. Afterwards, we focus on oxidation of lipid membranes exclusively and make a review of the latest experiments and simulations in that field.

In the second chapter, we describe the cell membrane and the model system used, the phospholipid bilayer, mainly as a GUV. In particular we give an overview on its characteristics, i.e. lipid movements, membrane permeability and mechanical properties. Eventually, the different techniques used in this work to control and probe the GUVs are described, especially the combination of the micropipette setup with a precise fluorescence detection method and further data analysis.

The third chapter studies the new photosensitizer, Chlorin-12, that we synthesized in collaboration with M. Baptista, USP, Brazil. Its photophysical and photochemical properties, as well as its complex behavior under light irradiation are investigated for different system sizes and under various experimental conditions.

In chapter four we show that GUVs are able to survive full hydroperoxidation, showing that membrane integrity can be preserved under these oxidation conditions. Our experimental setup allows to measure the relative area increase produced upon peroxidation, the associated change in mechanical properties of the membrane and also the hydroperoxidation efficiency, all of them with good precisions.

In a fifth chapter, the effect of a $^1\text{O}_2$ quencher, sodium azide, is studied in our systems and a simple model allows us to explain the reason of its inefficiency. Finally,

we attempt a comparison of the relative area increase measured in lipid bilayers with the one observed on monolayers at water-air interface. Subsequently, the stability of unsaturated monolayers is studied at the interface, under different controlled atmospheres.

Chapter 1

State of the art

1.1 Light-Matter interaction

1.1.1 Absorption of light

Light can be described as an electromagnetic wave or, alternatively, as a beam of photon particles, each of them having a given energy $E = h\nu$ (Fig. 1.1), where ν is the frequency of the wave and h the Planck's constant. Thus, absorption of light in molecules is governed by quantum laws. The energy states of molecules have an intrinsic discrete nature, with a finite number only of available energy levels.

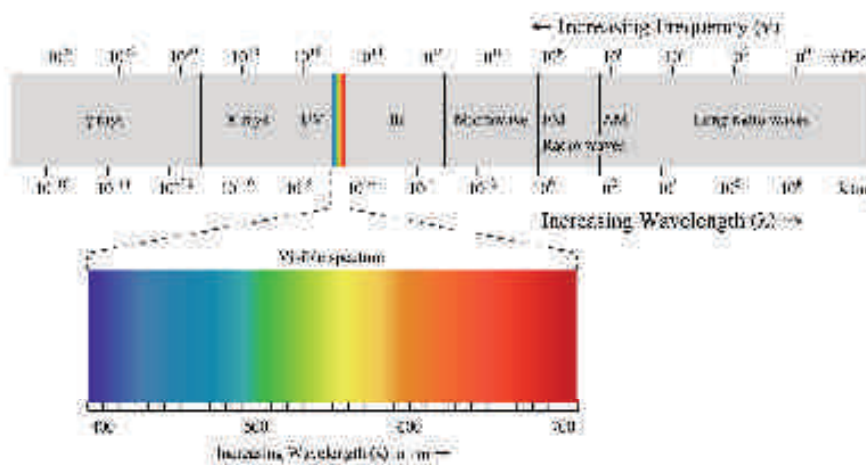


Figure 1.1: The electromagnetic spectrum.

Experimental observations

Optical radiation can be divided in different categories according to the wavelength. Visible light ranges from 400 to 800 nm. Radiation of shorter wavelength than visible light are described as ultraviolet (UV) and those having a longer wavelength as infrared (IR). The UV and IR bands are divided into sub-bands which are indicative of their interactions with biological macromolecules [7].

UV-C (200 nm - 290 nm) is strongly absorbed by cellular constituents, mainly proteins, nucleic acids and lipids. This band includes radiation strongly absorbed by DNA (Fig. 1.2).

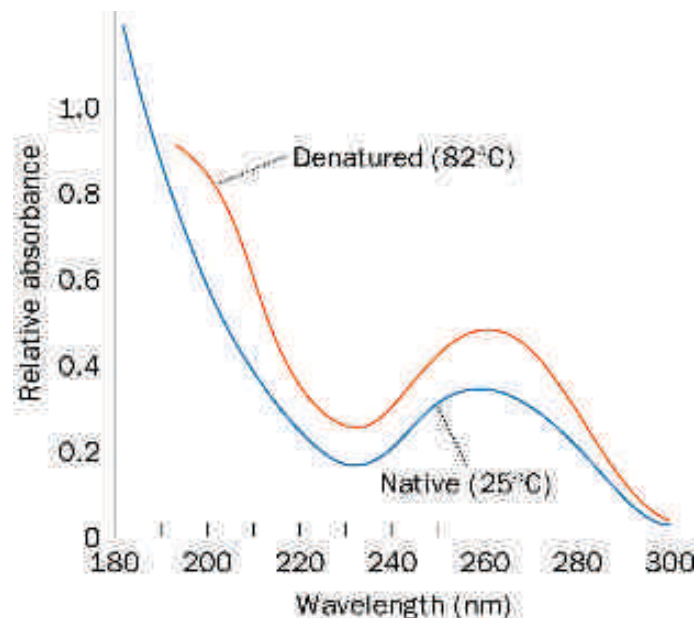


Figure 1.2: Absorption spectra of DNA. The main absorption peak is located around 260 nm (source: siumed.edu).

UV-B (290 nm - 320 nm) is absorbed mostly by aromatic amino acids and nucleic acids. The responses of skin to UV-B include vitamin-D production, erythema, hyper-pigmentation, and skin cancer induction. UV-A (320 nm - 400 nm) is weakly absorbed by cellular constituents.

Similarly, the IR spectrum is divided into sub-bands. IR-A (0.76 μm - 1.4 μm) is an optical window with minimal attenuation in tissues. IR-B (1.4 μm - 3 μm)

is absorbed mostly by water and bone. IR-C ($3 \mu\text{m} - 1000 \mu\text{m}$) is very strongly absorbed by tissue water.

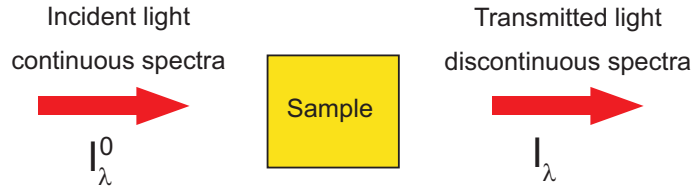


Figure 1.3: Principle of an absorption spectra measurement.

Experimentally, the light absorbed by a medium at a wavelength λ is characterized by the absorbance $A(\lambda)$ (Fig. 1.3), defined as:

$$A(\lambda) = \log \frac{I_{\lambda}^0}{I_{\lambda}}$$

where I_{λ}^0 and I_{λ} are the intensities of the beams entering and leaving the absorbing medium respectively.

In many cases, the absorbance of a sample follows the Beer-Lambert law:

$$A(\lambda) = \epsilon(\lambda)lc$$

where $\epsilon(\lambda)$ is the molar extinction coefficient ($\text{L mol}^{-1} \text{cm}^{-1}$), c the concentration (mol L^{-1}) and l the absorbing path length (cm).

A quantum description

In classical mechanics, it is possible to simultaneously determine the position and the impulsion of a particle. However in quantum mechanics, the uncertainty principle of Heisenberg states that knowing one of these two quantities precisely, yields a large uncertainty on the second quantity. This is accounted for by the following relation:

$$\Delta x \Delta p_x \simeq h.$$

In order to overcome this limitation, the electrons can not be described anymore in a classical manner. Thus, a so-called wave function $\Psi(x, y, z, t)$ is assigned to an electron so that $\Psi^* \Psi$ is the probability density of presence of an electron and $dP = |\Psi(x, y, z)|^2 dx dy dz$ is the probability to find an electron in the volume $d\tau = dx dy dz$.

Solving the Schrödinger wave equation $H\Psi = E\Psi$ is restricted to the hydrogen atom case. In the case of non hydrogenoid atoms or molecules, it is limited by the mathematical complexity associated with the multibody problem. The couples (E_i, Ψ_i) are respectively the eigenvalues and the eigenvectors of the equation. Thus, Ψ_i is an atomic orbital (AO) with an associated energy E_i . For symmetry reasons, these orbitals are given in spherical coordinates and can be separated in a radial (R) and an angular part (Y). They are defined by quantum numbers, as follows:

$$\Psi_{n,l,m_l}(r, \theta, \phi) = R_{n,l}(r) Y_{l,m_l}(\theta, \phi)$$

where:

- n is the principal electronic shell number. It is an integer number $n = 0, 1, 2, 3, \dots$ which corresponds to the energy level;
- l is the associated angular momentum, so that $0 \leq l \leq n - 1$. $l = 0, 1, 2, \dots$ corresponds respectively to s, p, d, ... the shape of the orbital (see Fig. 1.4);
- m_l is the quantum magnetic number, which is the projection of l on the reference axis (Oz) taking integer values from $-l$ to $+l$, so that $-l \leq m_l \leq +l$. For each value of l , there are $2l+1$ values of m_l . The energy levels are degenerated.

The behavior of a hydrogen atom in a magnetic field shows two possible states for the electron. There is an additional quantum number, the spin (s) of the electron, which can take two values $s = +1/2$ or $s = -1/2$.

The AOs are filled starting from the lowest energy, according to the Klechkowsky's rule, and respecting the Pauli exclusion principle, which assumes that two electrons

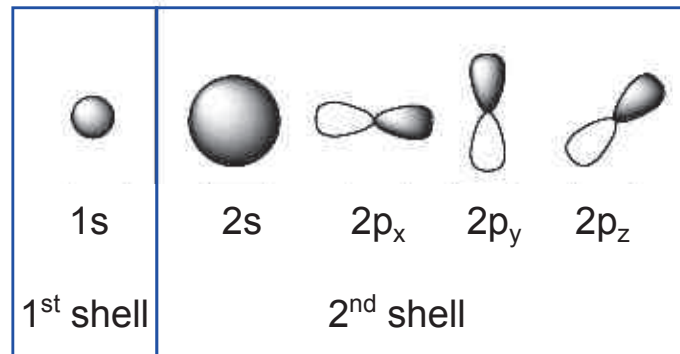


Figure 1.4: Scheme of the atomic orbitals s and p for $n = 1$ and 2 (source: adapted from chemwiki.ucdavis.edu).

can not be described by the same quantum numbers (n, l, m_l, s). Additionally, Hund's rule states that the most stable arrangements of electrons in orbitals of equal energy is the one with the greatest number of parallel spins.

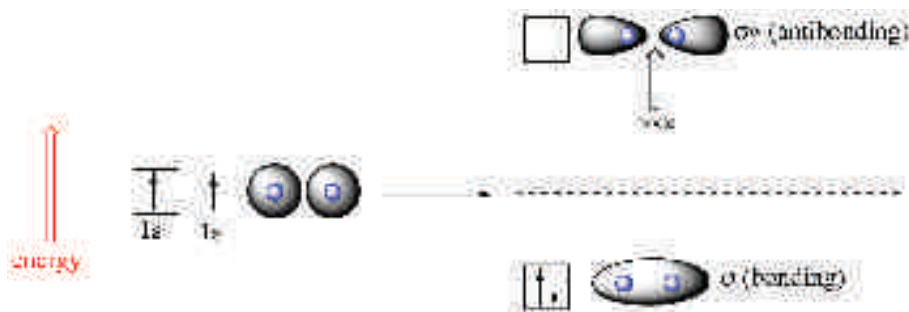


Figure 1.5: MO obtained from two AOs in the case of H_2 (source: chemwiki.ucdavis.edu).

Putting different atoms together in order to describe molecular orbitals (MO) is possible. The essential properties of covalent bonding are explained by combining the outer shell AOs from two atoms. A σ bond can be formed either from two s AOs or from one s and one p_x atomic orbital. In the simple case of the H_2 molecule, the two $1s$ orbitals combine to form two completely new orbitals, describing the location of an electron pair around two nuclei: one of lower energy than either of the two isolated AOs, referred as a σ bonding orbital, and another one of higher energy than the two AO, called σ^* which is an antibonding MO (see Fig. 1.5).

Here, electrons are represented as waves. If two electrons combine, they can form constructive or destructive interferences, which correspond respectively to bonding

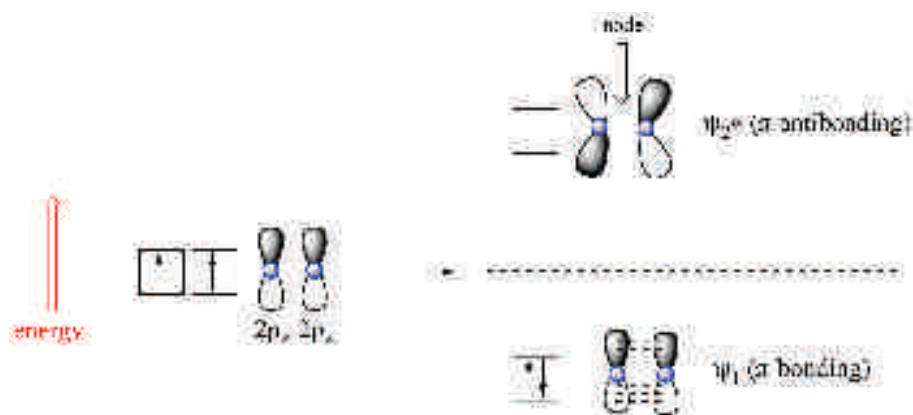


Figure 1.6: MO obtained from two AOs in the case of ethene (source: chemwiki.ucdavis.edu).

and antibonding orbitals. A π bond is made from the lateral overlap of two p_y (or two p_z) AOs. In ethene, for example, the two $2p_z$ AOs can combine to form a lower energy π bonding MO and a higher energy π^* antibonding MO (see Fig. 1.6).

By absorption of a photon of energy $h\nu = E_1 - E_0$, an electronic transition can occur from S_0 to S_1 , consisting of the promotion of a ground state electron to an unoccupied orbital. Different transitions, e.g. $\sigma \rightarrow \sigma^*$ or $\pi \rightarrow \pi^*$, can occur depending on the energy available. Thus absorption of a photon drives the molecule into an excited state. This phenomenon is very fast, typically in the order of 10^{-15} s.



Figure 1.7: Schematic representation of the ground state S_0 , singlet excited state S_1 and triplet excited state T_1 .

A singlet or a triplet state can form when one electron is excited to a higher energy level. In an excited singlet state, the electron is promoted in the same spin orientation as it was in the ground state (paired), whereas in a triplet excited state, the electron that is promoted has the same spin orientation as the other unpaired electron. The difference between the spins of ground state, excited singlet, and ex-

cited triplet is shown in Fig. 1.7. Singlet and triplet states can be derived using the multiplicity, $2S + 1$, where S is the total spin angular momentum (sum of all the electron spins).

1.1.2 De-excitation processes

Once a molecule is in an excited state, several possibilities are available for returning to its ground state. The Jablonski diagram (Fig. 1.8) is a convenient tool to visualize in a simple way the possible processes: photon absorption, internal conversion, fluorescence, intersystem crossing, phosphorescence...

Jablonski diagram

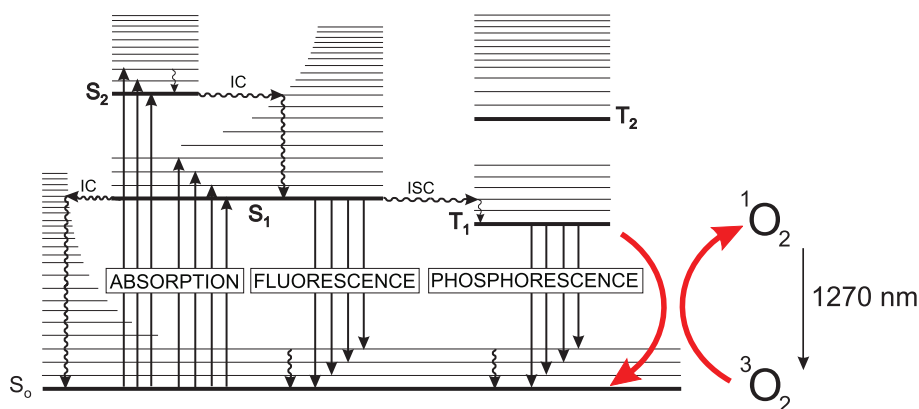


Figure 1.8: Jablonski diagram (adapted from [18]).

Internal conversion is a non-radiative transition between two electronic states of the same spin multiplicity. After light absorption, there is often vibrational relaxation towards the lowest vibrational level of the final electronic state. The timescale of IC is 10^{-13} - 10^{-11} s.

Fluorescence is the emission of a photon while decaying from S_1 to S_0 . The emitted photon always has a lower energy than the absorbed one. The emission of a photon is as fast as absorption (10^{-15} s). However, excited molecules can stay in S_1 a few tens of picoseconds to a few hundreds of nanoseconds, depending on the

molecule and the medium.

Intersystem crossing is a third possible de-excitation process from S_1 towards T_1 . It is a non-radiative process that can be fast enough to compete with other pathways like fluorescence. Crossing between states of different multiplicity is in principle forbidden, but spin-orbit coupling can be large enough to make it possible. The lifetime of T_1 being much longer than that of S_1 , this excited state has a higher probability of undergoing reactions such as with molecular dioxygen, thus creating an excited singlet oxygen species as further explained below.

Phosphorescence is only observed at low temperatures and/or in a rigid medium. In solution at room temperature, non radiative de-excitation is predominant.

Lifetimes and quantum yields

The rate constants for the different processes can be defined as follows:

For the singlet state:

- k_f : rate constant for radiative deactivation $S_1 \rightarrow S_0$ with fluorescence emission;
- k_{ic} : rate constant for internal conversion $S_1 \rightarrow S_0$;
- k_{isc} : rate constant for intersystem crossing $S_1 \rightarrow T_1$.

Thus, we can write a the non-radiative deactivation constant: $k_{nr}^S = k_{ic} + k_{isc}$.

For the triplet state:

- k_p : rate constant for radiative deactivation $T_1 \rightarrow S_0$ with phosphorescence emission;
- k_{nr}^T : rate constant for non-radiative deactivation $T_1 \rightarrow S_0$.

The fluorescence quantum yield, which represents the fraction of molecules returning to ground state by fluorescence emission, can then be expressed as follows:

$$\Phi_F = \frac{k_f}{k_f + k_{nr}^S}.$$

1.1.3 Energy Transfer

Another possibility to relax from an excited state to the ground state is energy transfer. Energy transfer is involved in quenching reactions or in FRET (Förster resonant energy transfer).

Quenching

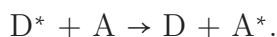
The term quenching describes the inhibition of photophysical or photochemical processes in the presence of additional species. There are different pathways, e.g. in physical quenching the excitation energy is dissipated harmlessly as heat and the original species is restored. On the other hand, the products of chemical quenching are different chemical species. Many types of quenching have been identified.

For example, physical quenching lead to loss of excitation energy:



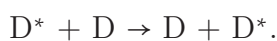
The acceptor (A) in these reaction may be an unexcited donor (D) molecule. This process is called self-quenching.

Intermolecular energy transfer is a model of physical quenching process in which the excitation energy of a donor is transferred to an acceptor:



This reaction requires downhill energetics and spin conservation.

If the donor and acceptor are identical, we have homotransfer:



When the process repeats itself so that energy migrates over several molecules,

the phenomena is called energy migration.

An example of energy transfer: singlet oxygen generation

Due to the long lifetime of the T_1 state, the excited molecule can interact with other molecules present in the medium. An energy transfer can then occur between T_1 and molecular oxygen for example. The molecule goes back to its ground state by exciting molecular oxygen 3O_2 to singlet oxygen 1O_2 , which is a very reactive species (see Fig. 1.8).

Name	Energy (kJ.mol ⁻¹)	Lifetime	Electronic configuration	
	155	$\leq 10^{-9}$ s	↑	↓
1O_2	94	$\simeq 10 \mu s$	↑↓	
3O_2	0	∞	↑	↑

Table 1.1: Oxygen excited states.

Förster resonant energy transfer

Various mechanisms of energy transfer have been identified. Long range dipole-dipole interaction is especially important because excitation energy can hop across intermolecular distances of several nanometers. Förster theory shows that the energy transfer efficiency (*Eff*) decreases with the sixth power of the intermolecular distance (r_{DA}) [19].

$$Eff = \frac{R_0^6}{R_0^6 + r_{DA}^6}$$

where R_0 is the Förster distance, between 10 and 100 Å. The detailed theory shows that R_0 depends on the fluorescence efficiency and lifetime of the donor, the absorption of the acceptor, and the overlap between the donor fluorescence spectra and the acceptor absorption spectra.

Thus, R_0 can be estimated as follows [18]:

$$R_0^6 = \frac{9000(\ln 10)\kappa^2\Phi_D^0}{128\pi^5 N_A n^4} \int_0^\infty I_D(\lambda)\epsilon_A(\lambda)\lambda^4 d\lambda$$

where κ^2 is the orientational factor, Φ_D^0 the fluorescence quantum yield of the donor in the absence of transfer, n the refractive index of the medium in the wavelength range where the overlap is important, $I_D(\lambda)$ is the normalized fluorescence spectra of the donor and $\epsilon_A(\lambda)$ is the molar extinction coefficient of the acceptor.

1.2 Oxidation in living systems

1.2.1 Lipid peroxidation: natural consequences of life with oxygen

Reactive oxygen species (ROS) are naturally produced in eukaryotic cells during mitochondrial respiration, catalysis by peroxisomal oxidases, and electron transport in endoplasmic reticulum. They play important roles in cell maturation and differentiation, eicosanoid synthesis which is a signaling molecule,... [20]. Although these ROS are natural products of cell metabolism, if their generation gets uncontrolled, they can lead to damage of biomolecules (lipids, proteins, DNA) as well as of macromolecular assemblies (biological membranes) [2].

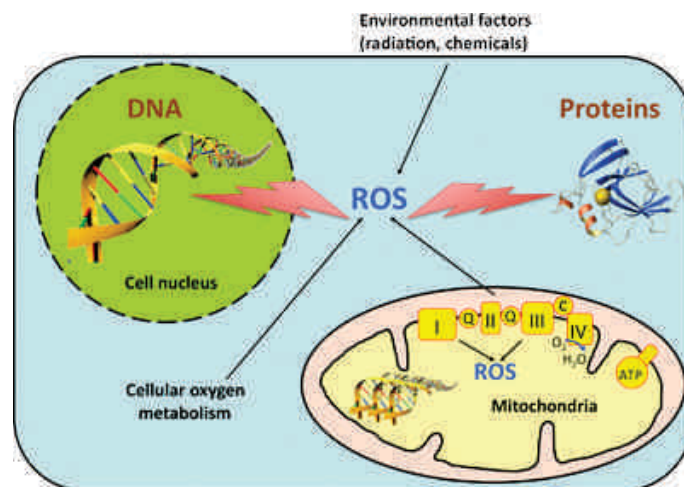


Figure 1.9: ROS targets in living systems (source: <http://nmr.fli-leibniz.de>).

1.2.2 Effects on membrane physical properties and protein function

Oxidation of the biological material can lead to deleterious effects on cells. Formation of oxidation products introduces a polar part into the lipid bilayer chains and, as a result, can disrupt the non-covalent bonds (van der Waals interactions) that help membrane stabilization. Many effects are described in the literature. Oxidation products can alter membrane packing, affect lipid-lipid and lipid-protein interactions. All of these modifications can compromise membrane integrity. Effects on membrane fluidity have been intensively studied. However, there is no agreement yet whether lipid peroxidation increases or decreases membrane fluidity [10, 21–24]. Controversy stands from the differences between analyses techniques which probe different regions of the membrane, and from the large variety of lipid compositions of the membrane.

Peroxidized membranes can also alter their affinity with proteins. Drobnies et al. [23] showed that disordering from oxidation of phospholipids facilitates insertion of CTP, phosphocholine cytidylyltransferase in the membrane. In contrast, protein kinase C is inhibited upon membrane oxidation [25].

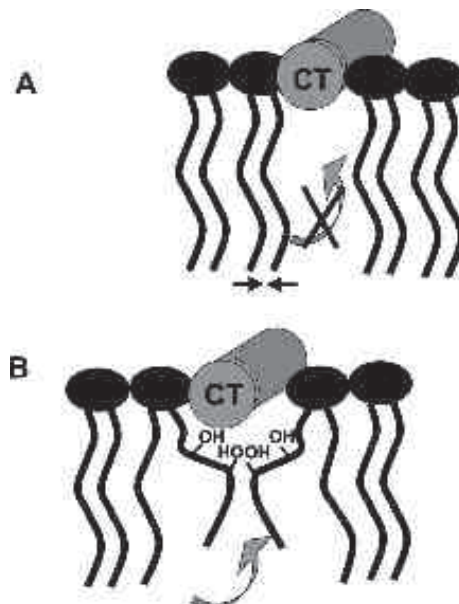


Figure 1.10: A peroxidized membrane showing a different affinity to protein insertion compared to its non peroxidized analog [25].

1.2.3 Cell defense mechanisms

Cells have a large defense system to protect against unwanted oxidation reactions. Low molecular weight antioxidants and enzymatic antioxidants are generally matched to the production of ROS [2]. The first line of defense is made from lipophilic chain-breaking, free radical scavengers (vitamine E derivatives, α -TOH,...) [26]. If oxidation is further sustained, several enzymes are able to repair the oxidized lipid chains. The coupling of Phospholipase A₂ (PLA₂) and glutathione peroxidase (GPx) is one of the most effective solutions. The first one can hydrolyse oxidized lipids easier than non oxidized ones. Their increased area per molecule makes them more accessible for PLA₂ [27]. Then, GPx reduces the OOH group to an inoffensive OH, which can not undergo chain reactions anymore. Finally, acyltransferase grafts a new chain [28].

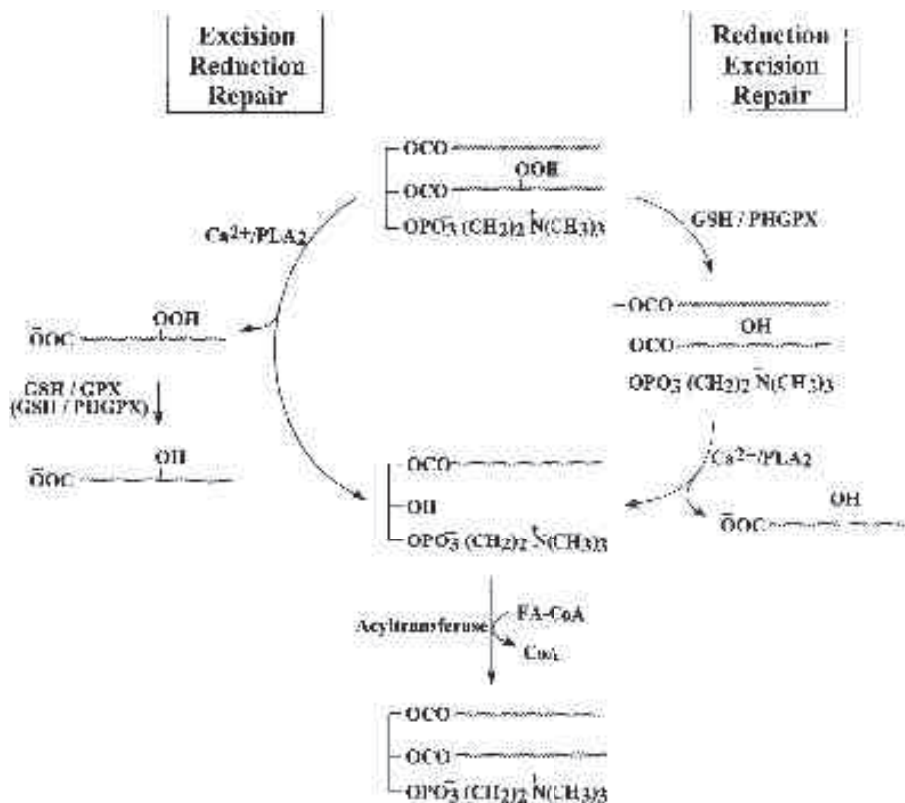


Figure 1.11: Proposed pathways of protection against the deleterious effects of phospholipid hydroperoxides. The Excision/Reduction/Repair pathway involves consecutive action of PLA₂, GPx, and an acyltransferase; whereas the Reduction/Excision/Repair pathway involves consecutive action of phospholipid hydroperoxide glutathione peroxidase, PLA₂, and an acyltransferase [28].

1.3 Photodynamic therapy

Photodynamic therapy (PDT) uses light-activated drugs, photosensitizers (PS), to treat several diseases like cancer, age-macular degenerations and antibiotic resistant infections. PDT has also been used to treat various solid tumors. The method relies on the administration of a photosensitizer molecule that is suitable to induce the formation of reactive oxygen species (ROS), powerful oxidizing agents that are able to destroy cancer cells (Fig. 1.12).

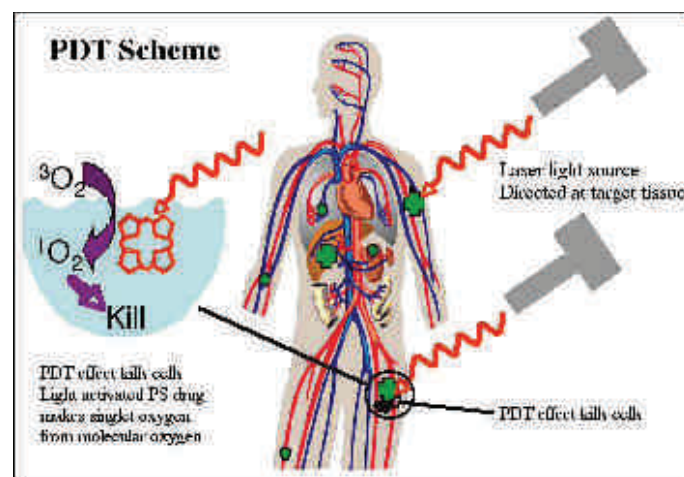


Figure 1.12: Scheme representing the principle of photodynamic therapy (source: <http://trialx.com>).

For practical purposes, PDT dosimetry is really important but somehow complex due to the dynamic nature of the three essential components: light, PS and oxygen. Considerable progress have been made in that technique in the last years, thanks to instrumentation able to measure the evolution of these components and to adjust their concentrations.

1.3.1 Clinical status

The first substantial animal and human tumors have been studied and treated in the late 70s by Dougherty et al. [29]. Nowadays, this technique succeeded in treating several cancers. The first tumor site approved for treatment was the bladder cancer, with transurethral light delivery [30]. Then, bronchial and esophagus cancer treatments showed good results. Presently, there are many tries on head, neck and pancreatic cancer. The treatment of skin tumors, particularly basal cell carcinoma,

is very efficient. However, other alternatives like excision, having high success rates, are preferred.

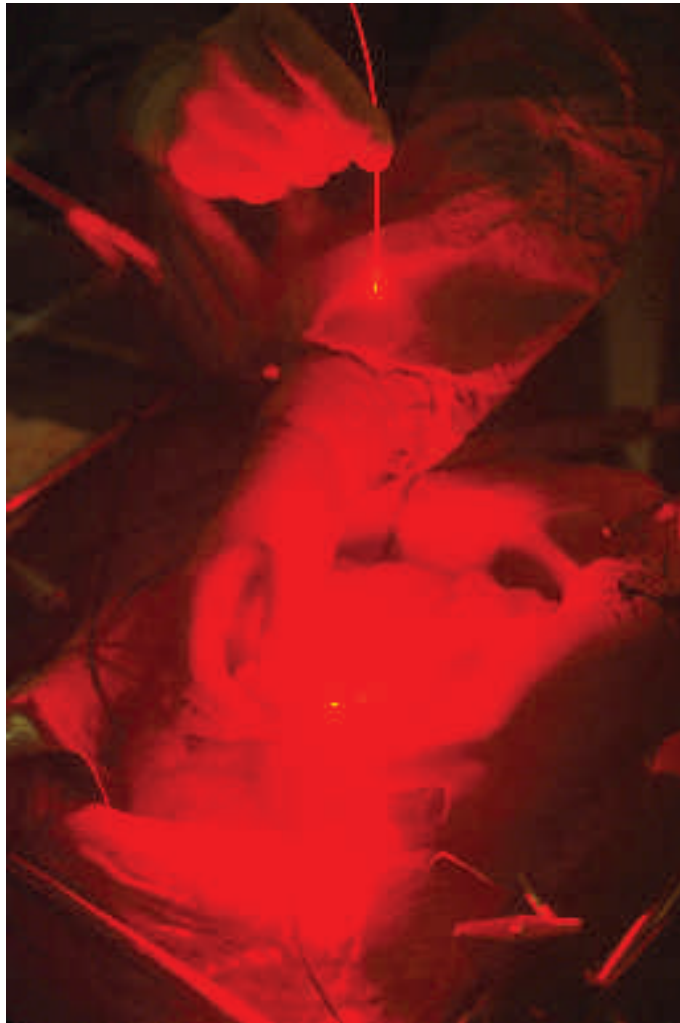


Figure 1.13: Patient being treated by PDT. After administration of the PS (photofrin) and concentration in cancer cells, the activation is done by a red laser beam positioned at the tumor site (source: National Cancer Institute).

PDT has recently also been used in the treatment of localized infections, when bacterial strains resist to antibiotics. Macular degeneration, which causes the loss of central vision due to growth of abnormal blood vessels can also be treated thanks to PDT [31].

1.3.2 Biological targets

Main PDT targets in mammalian tissues are either the cell itself or the blood vessels leading to tissue ischemia and a resultant target cell death.

Two types of cell death have been identified in photosensitization of mammalian cells (Fig. 1.14) [7]. One possibility involves generalized necrosis induced by cell membrane lysis followed by release of the inner constituents of the cell. Interaction of lysosomal enzymes with neighbor cells results in tissue inflammation. A second possibility of cell death involves apoptosis. It is characterized by a specific pattern of chromatin fragmentation and conversion of cells to apoptotic bodies, which are rapidly eliminated by phagocytic cells, minimizing inflammation [7].

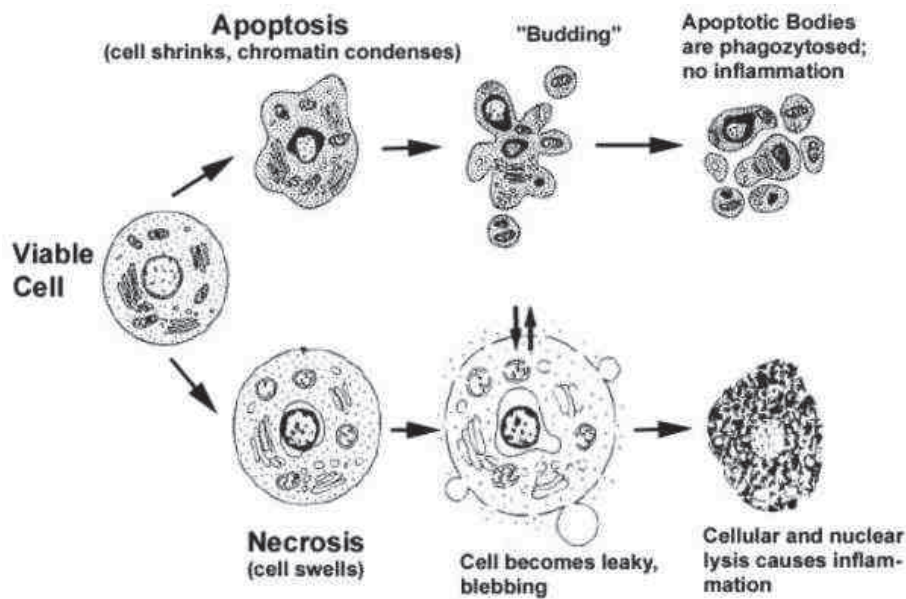


Figure 1.14: Scheme of the 2 scenarios leading to cell death: Apoptosis and necrosis [32].

Active research focuses on understanding the pathways to apoptotic cell death rather than necrosis, in order to avoid as much as possible tissue inflammation. Oxygen is the only ingredient required in PDT which is already present in the living systems. Thus, improvement of the PDT can only be done by tuning the two other constituents: the light source and the photosensitizer.

1.3.3 Photosensitizers, light sources and tissue optics

Light sources and tissue optics

The three main classes of clinical PDT light sources are lasers, LEDs and filtered lamps. Laser has the advantage of high efficiency coupling into single optical fibers for an endoscopic light delivery. It is monochromatic, thus it will only suit for a specific PS. Filtered lamps have the advantage to be easily tunable in their output wavelength. However, they can not be efficiently coupled with optical fibers [31].

To carry out a successful PDT, it is necessary to make sure that the light reaches the diseased tissue. Presence of microscopic inhomogeneities (cell organelles, macromolecules,...) makes tissues turbid and a fraction of the light is scattered. Another fraction is absorbed by tissue chromophores such as hemoglobin, myoglobin and cytochromes. Thus, the total attenuation coefficient can be expressed like $\mu_t = \mu_s + \mu_a$.

The scattering coefficient, μ_s is difficult to estimate. The complex architecture of tissues results in variations of the refractive index on many different length scales. Fractal models and, above all, experimental knowledge were quite successful to predict scattering behavior [33].

The absorption coefficient is determined by the concentration of light-absorbing molecules and expressed as: $\mu_a = \sum_k C_k \sigma_k$, where C_k is the molecular concentration of chromophore k and σ_k is its molecular absorption cross-section. Absorption coefficients of the main molecules present in tissues show an optical window, wavelength range where the light penetrates deeper in the tissues (Fig. 1.15). Red light and near-infrared light are the most efficient wavelengths.

The photosensitizers

A photosensitizer needs to absorb enough light to be efficient. Since the beginning of PDT, different PS have been used. The essential criteria for a useful PDT drug are:

- High absorption at wavelength in the range of $\simeq 700$ -850 nm;

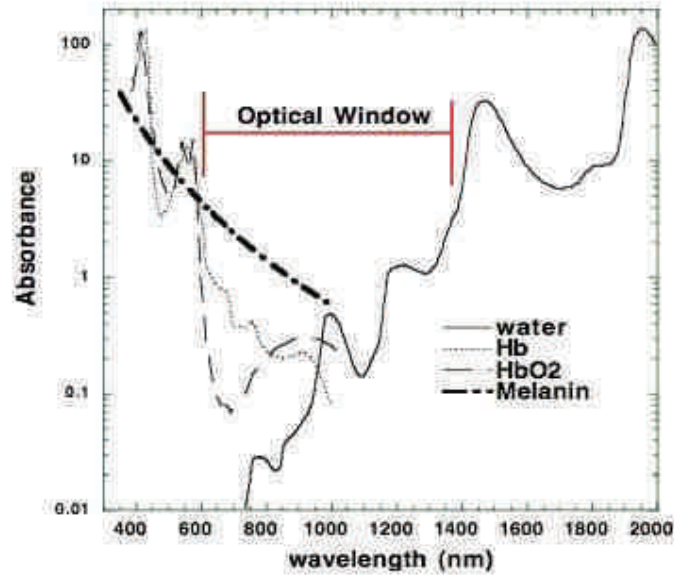


Figure 1.15: Absorption of the different molecules (hemoglobin, melanin, water) involved in tissue optics. The region where the most light can pass through is called the optical window. It is located in the red light and near infra-red (source: <http://www.photobiology.info>).

- High $^1\text{O}_2$ quantum yield but also fluorescence for monitoring;
- Photobleaching adapted to the treatment;
- Low dark toxicity;
- Uptake and retention by tumors.

Nowadays, the most efficient drugs are porphyrin analogs made of tetrapyrrole ring structures. The reference and most clinically used PS is Photofrin (Axcan, Quebec, Canada) which is a mixture of many porphyrin molecules derived from blood. It has a large Soret band at 400 nm and smaller Q-bands at longer wavelengths. However, this PS is retained for a long time in the body, leading to photosensitivity for several weeks and its absorbance spectra is not within tissue optical window. Chlorins (Fig. 1.16) are reduced porphyrins characterized by a strong enhancement of the far-red absorption band.

Such basic molecules are chemically modified by grafting different groups in order to modify their properties, especially solubility in different mediums or ability to be retained by various targets. Lipophilic drugs can pass through cell membranes. The

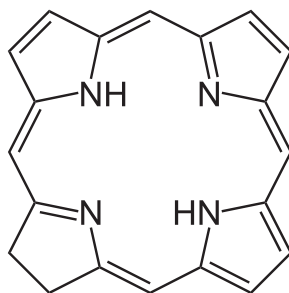


Figure 1.16: Chemical structure of a chlorin molecule.

hydrophilic drugs need to be bound to serum proteins in order to reach their targets and the hydrophobic ones may be administered via a carrier promoting solubility in water, such as an emulsion, surfactant micelles, and liposomes [7].

1.3.4 Mechanisms

The absorption of a photon of energy $h\nu$ brings the PS to an excited state S_1^* , without changing its spin. By intern conversion, the molecule goes down to its first singlet excited state S_1 . Then, there are two possibilities for the photosensitizer, either decaying to the fundamental state with emission of a photon of lower energy, a process called fluorescence with characteristic times 10^{-9} to 10^{-8} s, or intersystem crossing that brings the PS to a more stable state T_1 , the triplet state, with an increased lifetime of about 10^{-4} to 1 s. The return to ground state from triplet state is called phosphorescence. However, the long lifetime of this state allows the PS molecule to interact with the environment and to generate reactive species by two different schemes.

Type I reaction. By electron or hydrogen transfer with a neighbor molecule, the triplet state can induce radical species formation and a chain reaction.

Type II reaction. The triplet state transfers directly its energy to oxygen 3O_2 , leading to an excited state called singlet oxygen (1O_2).

Both types of reaction can be present. PS irradiation generates 1O_2 that can hydroperoxidize a first lipid, by a type II process. If there are traces of metallic ions in the medium, a chain reaction can start, leading to radical reactions (type I) (Fig. 1.17).

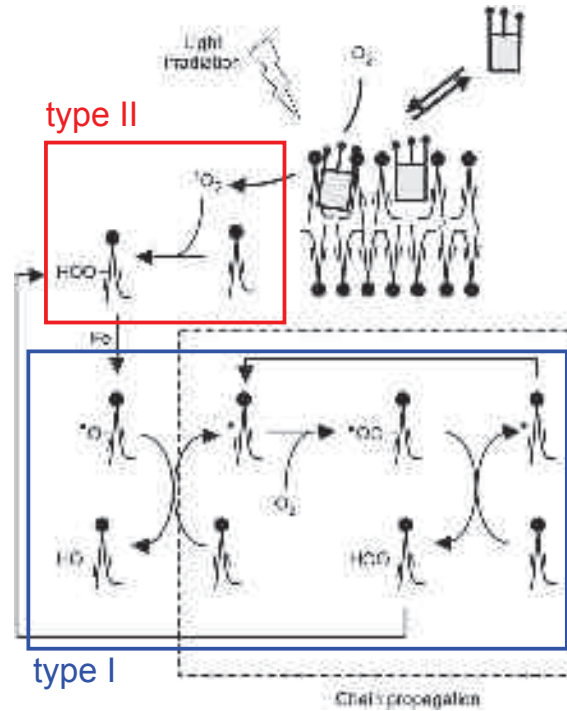


Figure 1.17: Scheme of the lipid photo-oxidation process in a membrane (adapted from Heuvingh et al. [16]). Hydroperoxidation through $^1\text{O}_2$ is the so-called type II mechanism. If there is a presence of iron ions, a chain reaction can be mediated and the hydroperoxidation is type I.

Singlet oxygen lifetimes

Singlet oxygen $^1\text{O}_2$, a very reactive species that oxidizes efficiently cell membranes, has a lifetime of about $4 \mu\text{s}$ in water. Given a diffusion coefficient in water $D_w = 2 \cdot 10^{-9} \text{ m}^2 \text{ s}^{-1}$ [34, 35], $^1\text{O}_2$ spans a distance $\sim 100 \text{ nm}$ in solution before it decays. The singlet oxygen lifetime in the absence of chemical reactions depends also on the solvent. By the use of deuterated solvents, $^1\text{O}_2$ lifetime can be increased by a factor 10 (Table 1.2).

Solvent	H ₂ O	EtOH	CCl ₄	D ₂ O	Living Cells	Air, 1 atm
τ (μs)	4	12	700	30	≈ 0.2	≈ 76000

Table 1.2: Singlet oxygen lifetime in different solvents.

Kinetic analysis

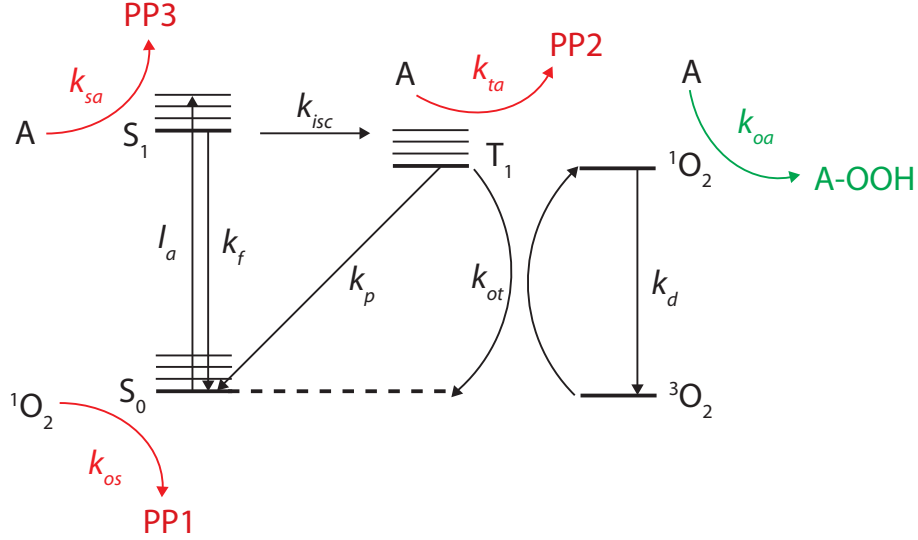


Figure 1.18: Jablonski diagram presenting the different steps for type I reaction leading to the hydroperoxide form (A-OOH) and also diverse parasite reactions leading to PS modification to photoproducts (PP1,PP2,PP3).

Several models have been proposed to describe the kinetics of the singlet oxygen mediated type I reaction. In his PhD thesis [36], Finlay incorporated the possibility for excited PS states (S₁ and T₁) to react with cellular targets (A) and for singlet oxygen to react with both A and S₀, leading to the following equations:

$$\frac{d[S_0]}{dt} = -I_a + k_f[S_1] + k_p[T_1] + k_{ot}[T_1][{}^3O_2] - k_{os}[S_0][{}^1O_2] \quad (1.1)$$

$$\frac{d[S_1]}{dt} = I_a - k_f[S_1] - k_{isc}[S_1] - k_{sa}[A][S_1] \quad (1.2)$$

$$\frac{d[T_1]}{dt} = k_{isc}[S_1] - k_p[T_1] - k_{ot}[T_1][{}^3O_2] - k_{ta}[A][T_1] \quad (1.3)$$

$$\frac{d[{}^3O_2]}{dt} = -S_{\Delta}k_{ot}[T_1][{}^3O_2] + k_d[{}^1O_2] \quad (1.4)$$

$$\frac{d[{}^1O_2]}{dt} = S_{\Delta}k_{ot}[T_1][{}^3O_2] - k_d[{}^1O_2] - k_{oa}[A][{}^1O_2] - k_{os}[S_0][{}^1O_2] \quad (1.5)$$

where the different terms are defined in Table 1.3.

Symbol	Definition	Units
I_a	rate of photon absorption	$M s^{-1}$
S_Δ	fraction of T_1 - 3O_2 reactions leading to 1O_2	
$[S_0]$	PS ground state	M
$[S_1]$	PS singlet excited state	M
$[T_1]$	PS triplet excited state	M
$[^3O_2]$	oxygen triplet state	M
$[^1O_2]$	oxygen singlet state	M
$[A]$	target molecules	M
k_f	$S_1 \rightarrow S_0$	s^{-1}
k_p	$T_1 \rightarrow S_0$	s^{-1}
k_{isc}	$S_1 \rightarrow T_1$	s^{-1}
k_d	$^1O_2 \rightarrow ^3O_2$	s^{-1}
k_{ot}	rate constant 3O_2 with T_1	$M^{-1} s^{-1}$
k_{os}	rate constant 1O_2 with S_0	$M^{-1} s^{-1}$
k_{oa}	rate constant 1O_2 with A	$M^{-1} s^{-1}$
k_{sa}	rate constant S_1 with A	$M^{-1} s^{-1}$
k_{ta}	rate constant T_1 with A	$M^{-1} s^{-1}$

Table 1.3: Notations, definitions and units used in kinetics analysis.

Simplification of equations 1.1-1.5 can be done by noticing that the lifetime of S_1 is too short (~ 10 ns) to react significantly with A, so that the term $k_{sa}[A][S_1]$ can be neglected. Additionally, S_1 , T_1 and 1O_2 are fast in the stationary regime, so that their time variations are zero. The following expressions can then be extracted:

$$[S_1] = \frac{I_a}{k_f + k_{isc}} \quad (1.6)$$

$$[T_1] = \frac{k_{isc}[S_1]}{k_p + k_{ot}[^3O_2] + k_{ta}[A]} \quad (1.7)$$

$$[^1O_2] = \frac{S_\Delta k_{ot}[T_1][^3O_2]}{k_d + k_{oa}[A] + k_{os}[S_0]} \quad (1.8)$$

Assuming that the PS concentration is much lower than the cellular targets, $k_{os}[S_0] \ll k_{oa}[A]$ and by replacing these terms in equation 1, one ends up with:

$$\frac{d[S_0]}{dt} = -k_{ta}[A][T_1] - k_{os}[S_0][^1O_2] \quad (1.9)$$

where only reactions of T_1 on A and 1O_2 on S_0 are responsible for decrease in PS concentration.

1.3.5 PDT Dosimetry

First of all, it is essential to be able to quantify light irradiation impinging diseased tissues. Knowing irradiation conditions and optical tissue properties, one can estimate the light fluence, which is defined as the total number of photons that intersect a unit area in a specific time interval. An alternative method is to measure it directly, using optical fibers modified in order to collect light over a large solid angle [37]. However, calibration of such isotropic detectors is challenging, since the response is not the same in air and tissue, due to the refractive index mismatch.

Photosensitizer detection

Once the irradiation light fluence rate has been determined, the next step is to follow the PS concentration in the target tissue. An ideal method would be non invasive and provide a 3D dynamic map of concentration. Most of the PS are fluorescent, typically with a quantum yield of a few percent, and one can then use this property to set up optical methods based on fluorescence measurements. Unfortunately, such a method will give an average concentration over some tissue volume rather than a comprehensive map. Emission will also depend on the local environment of the PS and the light will have to travel in the tissue over a certain distance, where it can be re-absorbed, before reaching the detector. However, if the propagation distance can be reduced by delivering the light and collecting the fluorescence through the same optical fiber, the measurement errors can be minimized. According to Diamond et al. [38], if the fiber diameter is smaller than $200 \mu m$, the concentration errors due to tissue absorption and scattering is less than 10 %.

For non-fluorescent PS, absorption spectroscopy can be used [39]. The advantage is that the method is less sensitive to changes in the PS environment. Thanks to this method, the quantity of oxy- and deoxy-hemoglobin, which is linked to the tissue

oxygen content, can be measured. Hence, it is possible to access O_2 concentration. Again, the information is obtained over a large tissue volume and is not able to detect local regions of hypoxia (suppression of oxygen supply).

Indirect singlet oxygen measurements

Evolution of emitted light by the PS with time gives access to its photobleaching behavior. Several mechanisms can play a role in PS bleaching, e.g. singlet oxygen reaction with PS ground state or PS triplet state reaction with cellular molecules (see equation 1.9). Considering only singlet oxygen reactions on PS ground state, Dysart et al. [40] showed that change in S_0 can be expressed by the following differential equation:

$$\frac{d[S_0]}{dt} = -k_{os}([S_0] + \gamma)[^1O_2]$$

where k_{os} is the bimolecular reaction rate between 1O_2 and S_0 , γ accounts for a reaction of a 1O_2 molecule with the PS from which it was generated.

Rearranging the equation to solve for $[^1O_2]$ and integrating over time gives the following expression for the total number of 1O_2 generated during the treatment between $t=0$ and $t=T$.

$$Dose = \frac{1}{\tau_\Delta} \int_0^T [^1O_2] dt = \frac{1}{\tau_\Delta k_{os}} \log_e \frac{[S_0]_{t=0} + \gamma}{[S_0]_{t=T} + \gamma} \quad (1.10)$$

where τ_Δ is the 1O_2 lifetime in the tissue.

This equation is valid even if fluence changes or oxygen depletion occur during the treatment. To quantify singlet oxygen generation, the knowledge of $[S_0]_{t=0}$, $[S_0]_{t=T}$, γ , τ_Δ and k_{os} is required.

However, photobleaching seldom exhibits such an easy behavior and different pathways are usually involved. In conclusion, much more needs to be done to establish validity for different PS and to demonstrate a clear correlation between implicit

dose and relevant biological outcome.

Direct singlet oxygen detection

It is possible to perform direct single oxygen measurements by detecting the weak luminescence emitted at 1270 nm when singlet oxygen returns to ground-state via a classically forbidden transition. After laser pulse excitation, singlet oxygen decay can be recorded. The amount of light is directly proportional to the instantaneous concentration of singlet oxygen in the media. Such experiment is challenging in vivo because singlet oxygen reacts so fast that its concentration is in the picomolar range and the signal is very weak. The early and strongest part of the time resolved signal is difficult to separate from confounding sources of luminescence, system noise and other artifacts, and is therefore gated out [41, 42].

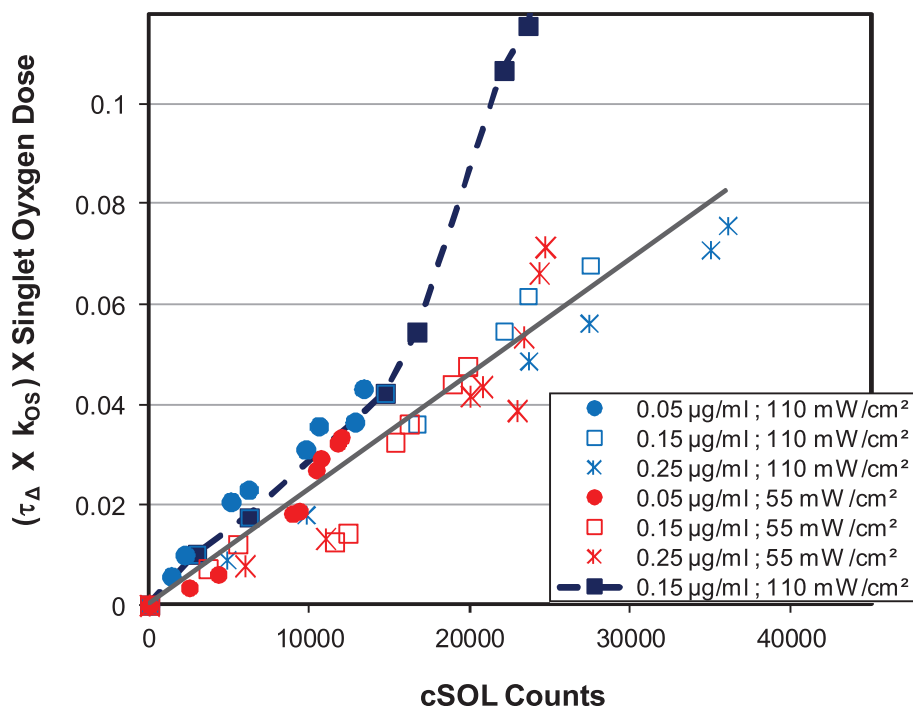


Figure 1.19: Singlet oxygen dose derived from photobleaching analysis as a function of cSOL counts. The deviation from linearity for the dashed curve corresponds to oxygen depletion in the medium [43].

A recent study by Jarvi et al. [43] shows new insights in dosimetry by doing a simultaneous singlet oxygen luminescence (SOL) and PS photobleaching. A clear

proportionality between the singlet oxygen dose derived from photobleaching analysis (Eq. 1.10) and the cumulative singlet oxygen luminescence (cSOL) is demonstrated (Fig. 1.19). The proportionality is only maintained as long as there is no oxygen depletion in the cell medium. As the cells are very concentrated, almost all singlet oxygens chemically react ($\eta \sim 1$), leading often to a depletion of $^3\text{O}_2$. The depletion is easily detected, as the curve deviates from linearity (dashed curve).

Several techniques and models have been developed in order to match the concentration of the PDT actors as well as the external parameters, e.g. light irradiation, to have a more efficient therapy. Avoiding O_2 depletion is truly important in that sens. However, a more powerful treatment is not necessarily the best solution in PDT.

Apoptosis/Necrosis

It has been repeatedly shown that if treatment times are increased whereas fluence rates are decreased, cell killing mechanisms are shifted from necrosis to apoptosis. A possible explanation could be that cell repair and molecular responses to oxidative stress become more important [44].

Indeed, a long time is required to achieve cell death by apoptosis. If the membrane is strongly oxidized, membrane lysis leading to necrotic death will occur before cell signaling pathways activate the family of pro-apoptotic proteins (Fig. 1.20). Some reports have shown that Bcl and Caspase play important roles to drive the cell death to apoptosis [45].

1.3.6 Future developments

Two-photon PDT

A way to get rid of some technical limitations would be to make two-photons PDT. A large amount of PS have their Soret band around 400 nm, a wavelength where light is mainly absorbed by tissue. Fig. 1.21 shows two different possibilities to overcome this limitation: resonant and two-color absorption.

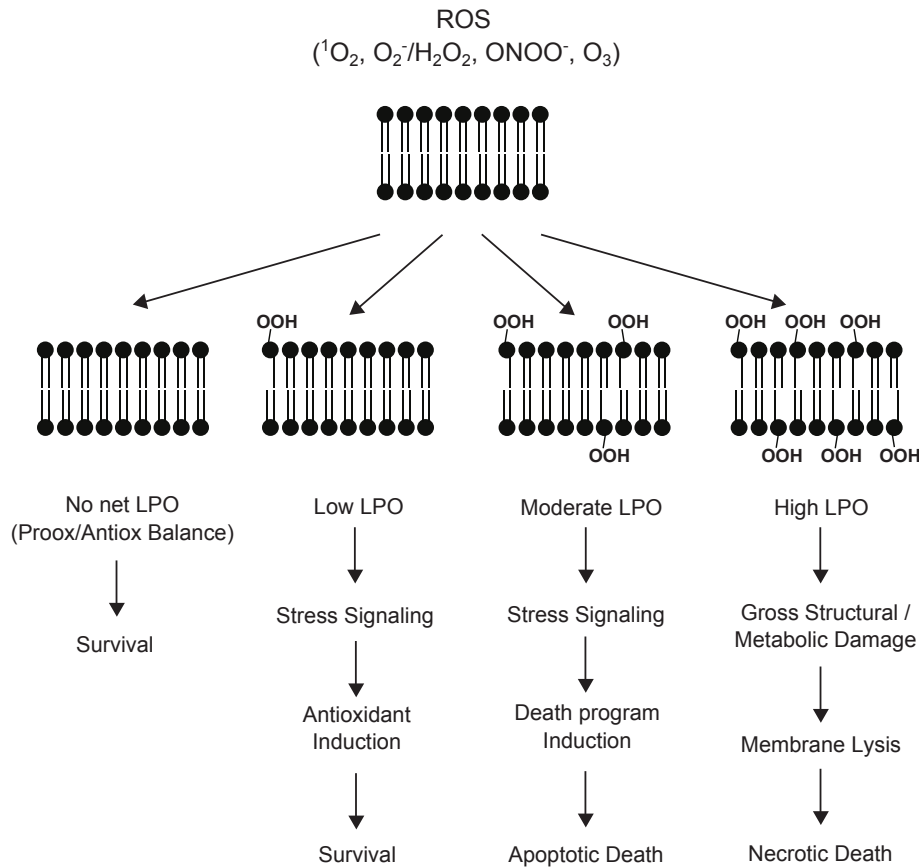


Figure 1.20: Diagram representing the different levels of membrane peroxidation and possible consequences in signal transduction. Responses may range from no effect to antioxidant induction, apoptotic cell death and finally necrotic death as the peroxidation increases. Transition from one phase to another may occur as some (undefined) threshold of damage is exceeded [28].

The first method relies on exposure of the PS to a short pulse in the near-infrared light (λ_{NIR}). Absorption of two photons of λ_{NIR} results in the same photophysical and photochemical processes (e.g. generation of singlet oxygen). In order to be effectively simultaneous, the light pulse must be shorter than ~ 100 fs. Pulsed light generates high instantaneous power, without heating the tissue too much. The first advantage is that the light penetrates deeper in tissue, allowing extended possibilities of treatment [46]. An other advantage is the quadratic dependence of two-photon absorption probability that can be exploited to achieve a spatial confinement of the PDT and limit the effects on nearby healthy tissue [47].

The second method involves two light pulses of different wavelength. The first

one will excite the PS and lead to triplet states generation. The second one will then excite the triplet state to a higher excited state that can directly interact with biological molecules. The main advantage of this method is that it works even in hypoxic conditions, which is particularly relevant to PDT of solid tumors.

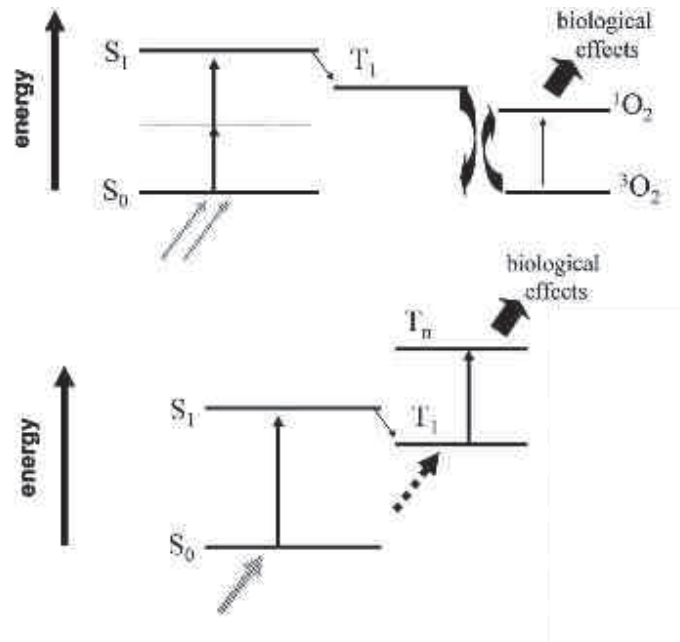


Figure 1.21: Scheme of two-photon PDT. Resonant process (on top) and two-color absorption (bottom)(adapted from Smith et al. [46]).

Molecular beacons

The concept of molecular beacons is based on FRET [48]. A quencher linked to the PS prevents singlet oxygen generation (Fig. 1.22). Upon interaction with the target, the linker can be broken so that the PS and the quencher separate, allowing PDT to occur. This possibility of activating the PS or not will be really useful for achieving a high level of target specificity and avoid damaging of non-target tissues.

1.3.7 Conclusion

PDT is a clinically used technique that treats several types of cancer. It is widely used nowadays and shows very good results on diseased tissues, limiting the nearby

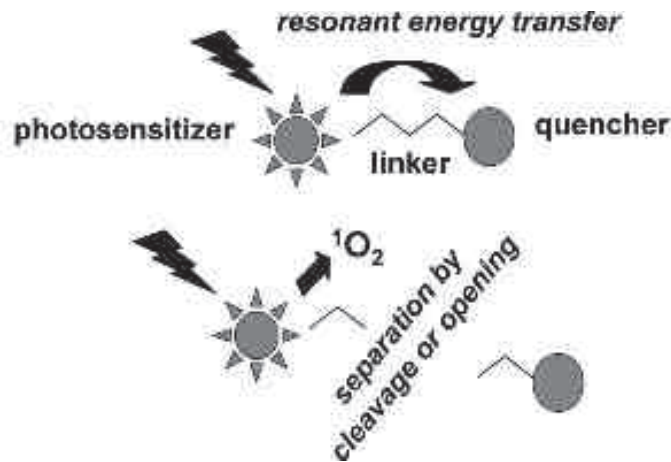


Figure 1.22: Concept of molecular beacons. Cleavage of the linker between PS and its quencher enables PDT [31].

healthy tissue damage thanks to a high target specificity. Therefore, there are significant efforts in applied research to improve treatments as well as in fundamental research to better understand the underlying mechanisms. As the generated ROS can react with several cellular constituents, it has been shown that interactions with membranes is an important step towards apoptotic cell death.

1.4 Effects on membranes

Unsaturated phospholipids, glycolipids and cholesterol in cell membranes are prominent targets of oxidant attack. Resulting lipid peroxidation can become a degenerative process that perturbs the structure and integrity of the target systems, often leading to cytopathological consequences [2].

1.4.1 Different oxidation pathways

ROS lead to different oxidized products. In the case of oxidation of cholesterol, Geiger et al. [49] showed that type I and type II reactions do not lead to the same oxidized molecules (see Fig. 2.4). Such differences could probably also happen with phospholipids.

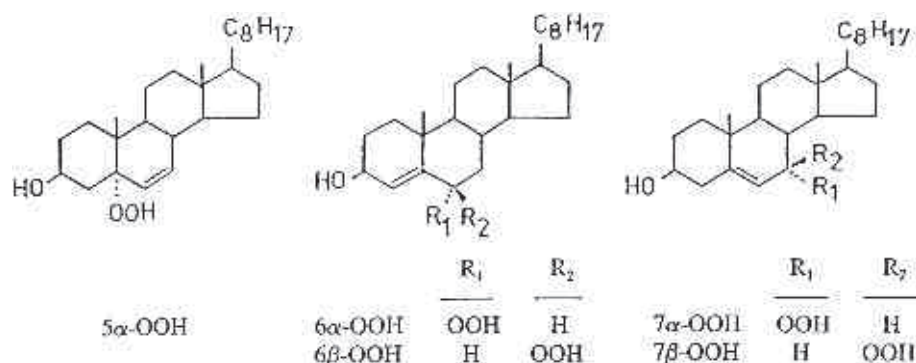


Figure 1.23: Structures of cholesterol hydroperoxide species generated by singlet oxygen attack on cholesterol ($5\alpha\text{-OOH}$, $6\alpha\text{-OOH}$, $6\beta\text{-OOH}$) and by free radical attack on cholesterol ($7\alpha\text{-OOH}$, $7\beta\text{-OOH}$) [49].

A unique characteristic of singlet oxygen generated hydroperoxides is that in absence of reductants and metal catalysts, they accumulate linearly without lag as a function of singlet oxygen production. Using POPC, there are only two different molecules that can be produced, depending on which side of the double bond the reaction takes place. Fig. 1.24 shows the two possibilities.

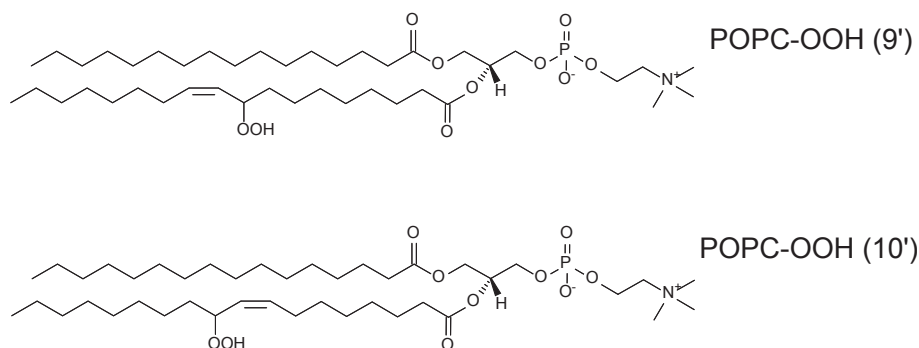


Figure 1.24: Products of the reaction of $^1\text{O}_2$ on POPC.

In the presence of traces of catalysts, e.g., Fe^{2+} , the photo-oxidation of lipidic systems results in a myriad of secondary products [50]: for mono-unsaturated chains, cleavage of the carbon chain near the initial position of the unsaturation occurs and resulting by-products like alcohols, aldehydes, ketones and lactones are formed.

Ozone reaction on phospholipids has been widely studied over the last fifteen years [51–53]. These studies are essentially done with monolayers on a Langmuir trough under an atmosphere of O_3 in O_2 . The reactions, in this case, are completely

different. Indeed, there is the formation of ozonide evolving in a Criegee intermediate leading to the oxidized form. It can be either an aldehyde or an acid [53], depending on the reaction conditions (acid or basic subphase, concentration of O_3). Wadia et al. [51] could, with their experimental setup, measure the nonanal molecules generated from lipid chain cleavage, leaving the interface towards the gas phase. Traces of the second Criegee intermediate have also been measured [53].

If the target phospholipid is POPC, which is to our knowledge the case in all the studies reported in literature, the main oxidation products obtained are shown in Fig. 1.25. Both of these lipids have the rest of the initially unsaturated chain cut.

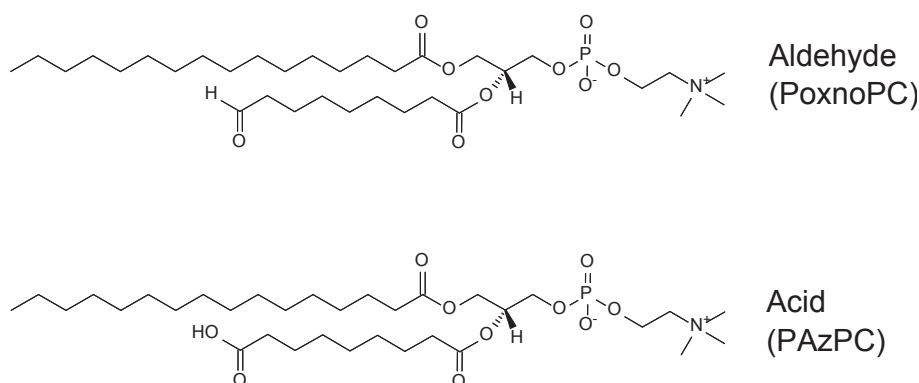


Figure 1.25: Products of the reaction of O_3 on POPC.

A recent study by Thompson et al. [52] confirmed the presence of the second Criegee intermediate. Both head and palmitoyl chain of POPC were isotopically marked in that study. Neutron scattering experiments showed that the heads stayed at the interface, whereas the palmitoyl chains (or at least part of them) left the interface. To explain these experimental facts, hypothesis of radical OH species production were formulated, leading to cleavage of both chains, even the saturated ones.

All these products and by-products are obtained from a relatively simple lipid (POPC). For more complex lipids, different molecules can be obtained with different yields and the resulting system will be more complex.

Only type II mechanisms lead to “clean” reactions, that means only hydroperoxide products, without any chain cleaved by-product. These hydroperoxide species, probably because of their high instability, were not much studied yet. It is unfortunate that many articles and reviews still express the idea that all peroxidation

reactions are mediated by radical species in nature, notwithstanding the fact that singlet oxygen peroxidation does not involve radicals.

1.4.2 Membrane integrity and permeation

In the last years, a substantial amount of work has been published on membrane oxidation in different geometries (monolayer, bilayer) with different photosensitizers, different phospholipids,... Many parameters have been varied and the modification of different properties has been evaluated.

Chain cleavage

A key feature in applied PDT is how membrane integrity is affected upon irradiation. Indeed, apoptotic cell death is induced by signaling molecules. Therefore, the oxidation should be controlled and membrane lysis avoided. There are many studies where membrane integrity is highly compromised and vesicles are destroyed. Caetano et al. studied the effect of Methylene Blue (MB), in solution, on giant vesicles made of DOPC [11]. They showed that above a certain threshold of MB ($\approx 100 \mu\text{M}$), DOPC giant vesicles show a large area increase, pore formations and finally membrane disruption. Cutting of the lipid chains at initial unsaturation location was proposed as the most probable scenario.

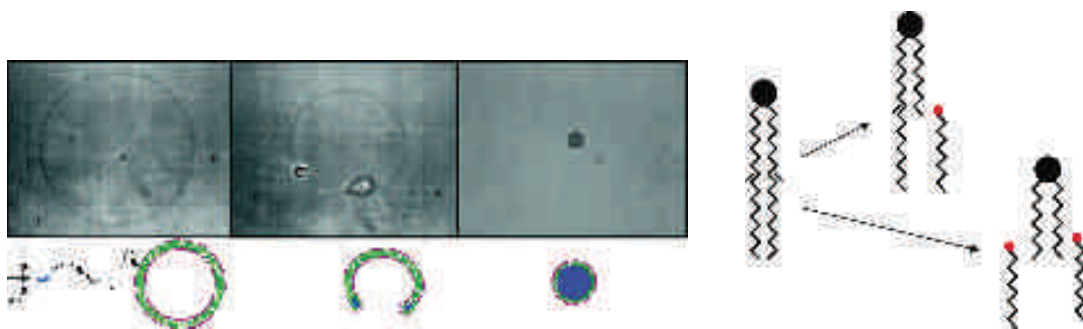


Figure 1.26: Scenario of vesicle destruction upon reaction with MB under irradiation. Cutting of the phospholipid chains is the cause of the phenomena [11].

Others studies by Heuvingh et al. [16] reported oxidation of GUVs made of DOPC by a chlorin photosensitizer at a concentration of $50 \mu\text{M}$. These concentra-

tion was under the critical threshold given above. In these experiments, thanks to phase-contrast imaging, vesicle permeation has been recorded and showed an increase upon oxidation. Time within membrane lysis has also been analysed as a function of membrane tension (fixed by a micropipette setup). For higher tension applied, lysis occurred within a shorter time, whereas all other parameters are kept constant. Again, type I reaction were hypothesized, governed by chain propagation. Their last experiments focused on introducing cholesterol within the DOPC bilayers [54] and showed that with increased amount of cholesterol, the effect of membrane permeation can be lowered.

Cwiklik et al. [55] recently studied pore formation in oxidized DOPC bilayers by numerical simulations. Four couples of oxidative products were investigated, with different cleavage locations, and chain removal. According to these results, products with only one oxidized chain lead to pore formation (Fig. 1.27), whereas products where both chains are cleaved perturb more strongly the bilayer, that is destroyed within 10 ns.

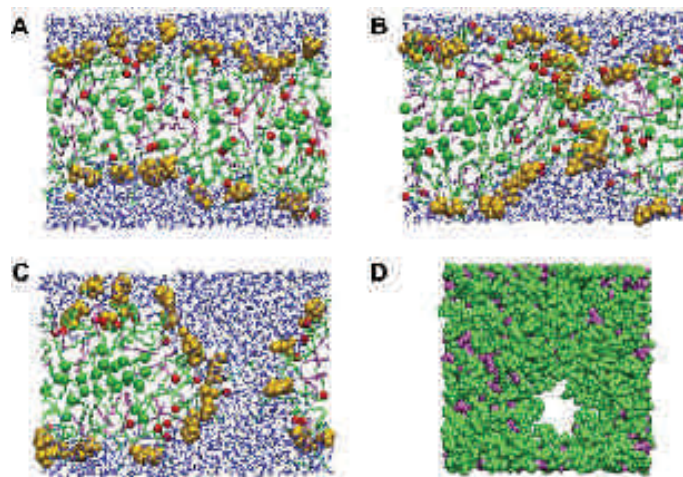


Figure 1.27: Formation of a pore in an oxidized DOPC bilayer. Side-view cross-sections made at the center of the pore using snapshots taken at 10, 40 and 110 ns are presented in (A), (B) and (C), respectively. Plot (D) depicts the top-view of the system at 110 ns upon oxidation, note the pore visible as the white region [55].

Hydroperoxidized lipids

Wong-Ekkabut et al. [56] investigated the effect of lipid peroxidation on the properties of 1-palmitoyl-2-linoleoyl-sn-glycero-3-phosphatidylcholine (PLPC) lipid bilayers using molecular dynamics simulations. They focused on four main oxidation products of linoleic acid with either a hydroperoxide or an aldehyde group: 9-trans, cis-hydroperoxide linoleic acid, 13-trans, cis-hydroperoxide linoleic acid, 9-oxo-nonanoic acid, and 12-oxo-9-dodecenoic acid (see Fig. 1.28). These oxidized chains replaced the sn-2 linoleate chain.

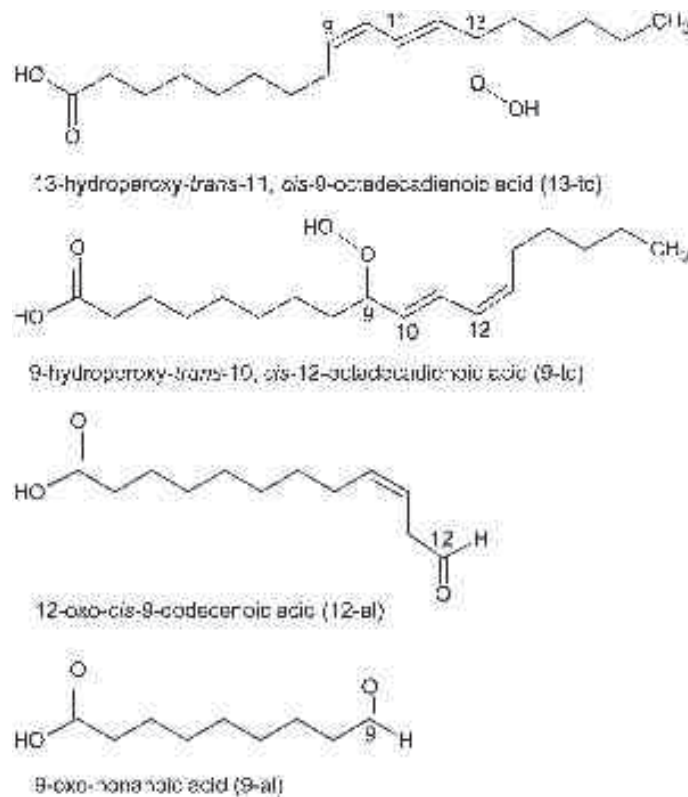


Figure 1.28: Oxidation products of linoleic acid considered in the work of Wong-Ekkabut [56]

This study is the first one where hydroperoxides were considered as oxidation products. Membrane permeation could be evaluated as a function of the fraction of oxidized phospholipids and its content in the membrane. Values are displayed in Fig. 1.29.

According to the simulations, increasing oxidized lipid fraction in the membrane leads to a higher membrane permeability.

Lipid bilayer	Concentration of oxidized lipids (%)	Permeability of water ($\times 10^{-5}$ cm/s)
PLPC	0	1.6 ± 0.5
PLPC with 9-tc	11.1	3.3 ± 0.6
	50	11.6 ± 4.5
PLPC with 13-tc	11.1	2.1 ± 0.8
	50	92 ± 40
PLPC with 9-af	11.1	3.2 ± 1.9
	50	16.1 ± 4.7
PLPC with 12-af	11.1	4.0 ± 2.2
	50	66 ± 32

Figure 1.29: Water permeability through PLPC bilayers containing four different oxidized lipids (concentrations of 11.1% and 50%) [56]

Recently, experiments with anchored photosensitizers have been done. Riske et al. [57] have shown that a porphyrin derivative grafted to two PE phospholipids can be anchored in giant unilamellar vesicles and thus generate singlet oxygen species in the immediate vicinity of the bilayer. Contrary to other model lipid bilayers where changes in permeability and vesicle destruction were studied [10–16], light induced oxidation in this case did not disrupt the membrane, showing that such a photosensitization method did not lead to any reaction between the triplet state of the porphyrin sensitizers and the chain double bonds. Anchoring of the photosensitizers on the membrane provided thus a reliable pathway to the exclusive formation of hydroperoxide products, leading to bilayer area increase while keeping the vesicle integrity.

Comparison of these observations with simulations of Wong-Ekkabut shows some similarities about membrane permeation behavior. Indeed, 9-tc molecule in the simulation is the closest oxidation product from Riske’s experiment and this product is the one with the smallest increased simulated permeation.

According to the recent literature, membrane permeation and integrity upon oxidation depends on lipid composition and oxidation method. Photosensitizers dispersed in the bulk, that can bind to the membrane lead preferentially to cleaved phospholipids and thus to membrane permeation. When oxidation is very strong,

above a certain threshold, membrane integrity can be compromised and vesicle destruction has been reported. On the other hand, by using anchored photosensitizers, membrane permeation is not or only slightly increased and the vesicle integrity is kept. This point needs to be further studied to acquire a better understanding of the mechanisms involved.

1.4.3 Modification in preferred lipid area

Area increase

Phospholipid oxidation changes drastically the lipid structure. Whether the chain is cut or not, an hydrophilic group appears close to the position of the initial unsaturation. Migration of this hydrophilic group towards the water interface is more energetically favorable and the average area per molecule is thus increased (See Fig. 1.30).

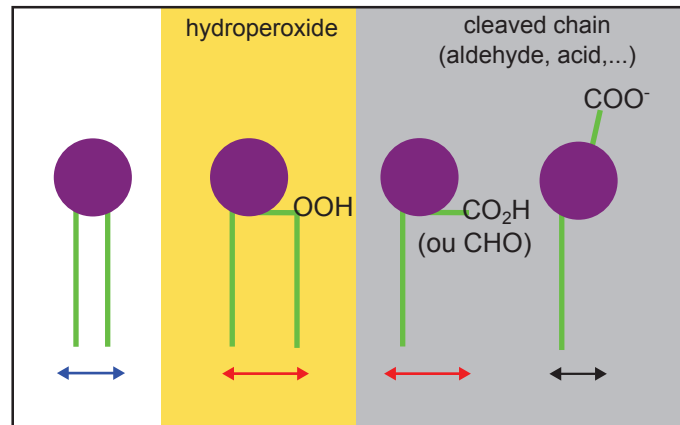


Figure 1.30: Scheme of the different structures of the possible oxidized lipids. Hydroperoxidized or cleaved lipids show an area increase. Anionic carboxyl group leads to chain reversal and thus to a smaller area per lipid.

Macroscopically, the vesicle area increase is a common observation in several experiments. Riske et al. [57] measured the area increase in POPC GUVs using an electric field to deform the vesicle (Fig. 1.31). However, the quantitative determination of the molecular area per lipid changes induced by hydroperoxidation was prevented by photosensitizer aggregation, a consequence of the planar structure of porphyrins.



Figure 1.31: Irradiation of a GUV containing $X_{porph} = 0.03$ in the presence of an AC field (10 V, 1 MHz), which induces prolate deformation. The electric field direction is indicated on the left and the irradiation time on top of each snapshot. The scale bar represents 20 μm [57].

In the simulation paper of Wong-Ekkabut et al. [56], the increase of area per lipid for the different oxidation products considered was estimated for concentrations ranging from 2.8% to 50% of each oxidation product. Fig. 1.32 shows the area increase per lipid as a function of the concentration of oxidized lipids. A linear increase, which is almost similar for the different products, is observed. A recent paper from Khandelia et al. [58] confirmed these values for the aldehyde form (PoxnoPC), whereas a complete acyl chain reversal is observed for the anionic carboxyl form, leading to a smaller area per molecule.

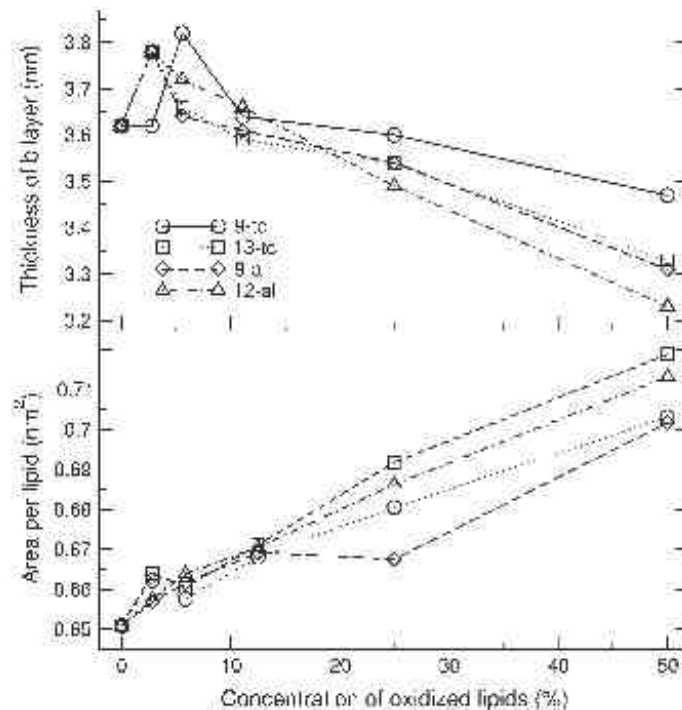


Figure 1.32: The thickness and area per lipid of lipid bilayer, containing various concentrations of each oxidized lipid [56].

In addition to area increase, a membrane thinning of 10 % has been observed for a bilayer containing 50 % of oxidized products (Fig. 1.32).

Membrane destabilization

In some cases, the oxidized phospholipids are not able to stay at the interface and migrate to the bulk solution, e.g. by forming micelles. Also shrinking of vesicles has also been evoked in some studies [11]. Liljeblad et al. [59] have demonstrated that monolayers made from phospholipids having both chains unsaturated become unstable when exposed to the laboratory atmosphere. After an initial increase, the area per lipid decreased with time at air exposure, proving that the oxidized phospholipids left the interface. This observation has been confirmed by simulations from Khabiri et al. [60]. Monolayers containing DOPC and one of its oxidation product, which has only one chain modified to the aldehyde form, were studied. Area increased with the fraction of oxidized lipids until a certain threshold. Above 75 % of oxidized lipids, the oxidized DOPC molecules left the interface and formed micelles in the aqueous subphase (Fig. 1.33).

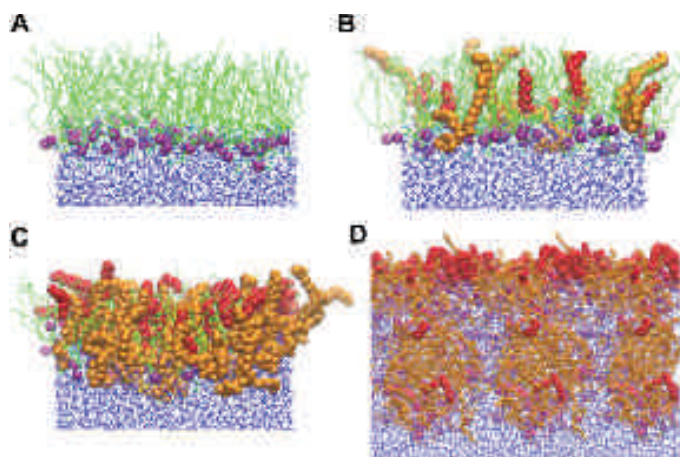


Figure 1.33: Simulated DOPC monolayer upon increased oxidation. Representative snapshots of equilibrated monolayer with 0%, 10%, 50% and 100% (in A-D, accordingly) of oxidation. Micelle formation has been showed to form at high oxidation level [60].

A striking fact is the difference in relative area increase in monolayers compared to bilayers. Van den Berg et al. [27] reported a difference between PLPC and its oxidized forms (PLPC-OOH and PLPC-OH), which is around 50%. In bilayers, all simulations up to now showed an area increase under 20%.

1.4.4 Oxidation efficiency

In concentrated cell medium like biological tissues, all singlet oxygen generated by the photosensitizer is able to react with a target. However, in single vesicle experiments or in dilute liposomes, a large part of singlet oxygens decay, because of their short lifetime ($\approx 4 \mu\text{s}$ in water), before reacting. In order to achieve an improved efficiency, a possibility is to bring the singlet oxygen source close to the reaction site.

Comparative studies

Mojzisova et al. [61] measured relative efficiencies for three different photosensitizers: *meso*-tetra(3-hydroxyphenyl)chlorin (*m*-THPC), chlorin e6 (Ce6) and *meso*-tetraphenylchlorin substituted by two adjacent sulfonated groups (TPCS_{2a}) compared in solution and when incorporated in dioleoyl-*sn*-phosphatidylcholine (DOPC) liposomes. In solution, all of them have the same quantum yield of singlet oxygen production ($\phi_{\Delta} \approx 0.65$).

The measure of efficiency was done by investigating the photo-induced membrane permeation thanks to entrapped carboxyfluorescein release. The relative efficiency was shown to be *m*-THPC > TPCS_{2a} > Ce6 in agreement with the depth of incorporation of the PS in the membrane. TPCS_{2a} and Ce6, thanks to their negatively charged chains, anchor near the water-lipid interface, whereas *m*-THPC anchors at a deeper position. This method only allows for a comparison between photosensitizers, but does not provide for a quantitative evaluation of efficiency.

The group of Ehrenberg [62–65] investigated the localization and photophysical properties of synthetically derived chlorins in artificial membranes, with the goal of designing more effective photosensitizers for photodynamic therapy (PDT).

The studied chlorins incorporate substituents (Fig. 1.34) of varying lipophilicity at the C₅-*meso*-position (H to C₅H₁₁), while the C₁₃- and C₁₇- positions have carboxylate anchoring groups tethered to the tetrapyrrole by alkyl chains (CH₂)_n (n = 1-3).

The depth of insertion of the PS in the membrane was assessed by two fluorescence-quenching techniques: by iodide ions from the aqueous phase and by using the

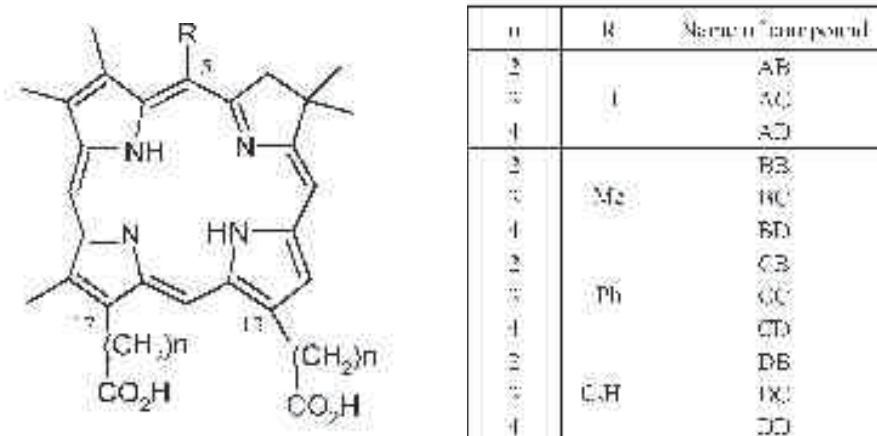


Figure 1.34: Different molecules used by Ehrenberg et al. [62–65]. By varying the different groups, different anchoring depth can be achieved in the membrane.

parallax method with spin-probe-labeled lipids anchored in the membrane. It was found that as n increases, the chromophoric part of the molecule, and thus the $^1\text{O}_2$ generation site, is located deeper in the bilayer. These results demonstrated that longer side chains lead to a larger affinity for artificial membranes and also caused the tetrapyrrole ring to be localized deeper in the bilayer. This location lead to a higher effective quantum yield for the reaction of singlet oxygen with its chemical target 9,10-dimethylanthracene (DMA) [66].

Quantitative measurement

Different assays for estimating in a quantitative manner the hydroperoxidation efficiency have been undertaken. In the study of Caetano et al. [11], a value of about one chain scission per 25 $^1\text{O}_2$ molecules reaching the membrane surface was estimated. More recently Riske et al. [57] calculated a value of 1 singlet oxygen over 270, that would actually react with a double bond. These values are very different and not really precise, so that better measurements would be welcome here.

1.4.5 Other studies in the field

Since model systems allow to work on basic systems, easy to handle and to drive out of equilibrium, a lot of different studies emerge these days. Heuvingh et al. [16]

used Chlorin e6 to mark only the inner or the outer leaflet of the vesicle bilayer. By doing so, preferential oxidation of one leaflet lead to an asymmetric curvature between the two monolayers and induced more specifically vesicle budding (inward or outward).

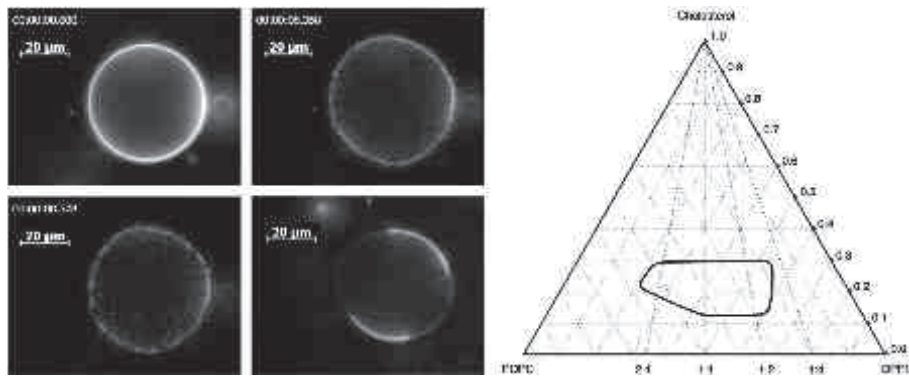


Figure 1.35: Left: Photo-induced phase separation in a vesicle made from POPC, DPPC and cholesterol. Right: ternary phase diagram of the system, the surrounded zone defines the region of phase separation.

Haluska et al. [67] used photo-induced oxidation to trigger phase separation in mixed vesicles. Vesicles made of a mixture of POPC, DPPC and cholesterol were formed, using concentrations where no phase separation is observed. Under irradiation, POPC and cholesterol were oxidized, changing the phase diagram of the system and shifting it to a region where phase separation is predicted (Fig. 1.35).

Photosensitizer containing vesicles can also be used for targeted delivery of drugs via encapsulation and subsequent light-induced release from liposomes. Several studies have been performed in this direction [68].

1.5 Conclusion

In this chapter we have introduced the reactive oxygen species (ROS) that are naturally produced in eukaryotic cells, where their role can be either beneficial or deleterious, depending on ROS concentration and on the conditions of the cell environment. Lipid oxidation products carry usually polar moieties and, as a result, can disrupt the non-covalent bonds (vdW interactions) that help lipid bilayer stabilization, altering membrane packing and affecting lipid-lipid and lipid-protein interactions.

Biomolecular oxidation is at play in photodynamic therapy (PDT), a medical technique that uses light-activated drugs, photosensitizers, to treat several diseases. The method relies on the administration of a photosensitizer molecule that is suitable to induce the formation of reactive oxygen species, powerful oxidizing agents that are able to destroy cancer cells. Active research focuses on the understanding of the pathways to apoptotic cell death rather than necrosis, in order to avoid as much as possible tissue inflammation.

The main photophysical mechanisms for generation of oxidative species are known. Light absorption by the photosensitizer generates excited triplet states, leading to reactive oxygen species. Two mechanisms are possible: by electron or hydrogen transfer with a neighbor molecule, the triplet state can induce radical species formation and a chain reaction (type I); the triplet state transfers directly its energy to oxygen $^3\text{O}_2$, leading to an excited state called singlet oxygen ($^1\text{O}_2$) (type II).

However, the physical transformations induced by ROS on lipid bilayers are still poorly understood. Depending on different parameters like the mechanism involved and the presence or not of other molecules, several oxidation products can be produced, mainly chain cleaved lipids or hydroperoxides. Although the first ones are well studied and often compromise membrane integrity, little is known on hydroperoxidized membranes, probably because of their high instability. It is unfortunate that many articles and reviews still express the idea that all peroxidation reactions are mediated by radical species in nature, notwithstanding the fact that singlet oxygen peroxidation does not involve radicals. Unsatisfactory identification of the proper mechanisms could explain why reports on membrane modifications upon oxidation are controversial and a new effort is clearly needed to clarify the mechanisms of lipid bilayer oxidation.

Model systems are widely used to mimic the cell membrane and have proved one's worth. However, the techniques to investigate the induced effects on vesicles show some limitations. Electric field deformation of membranes requires ionic asymmetry across the membrane. Pore formation easily breaks this asymmetry, limiting the scope of the technique and new methods need to be sought. In this PhD work, we will control the photosensitizer spatial distribution by anchoring a new chlorin molecule in the membrane, and will micromanipulate GUV systems under an optical microscope to quantify the oxidation effects.

Chapter 2

Systems and techniques

Phospholipid bilayers are simple biomimetic models of cell membranes. In this chapter we will briefly describe the cell membrane and its basic constituents, before reviewing the most common experimental model systems. In the third part, we will describe the physical properties of these systems, as well as the techniques that we will use to control and probe the bilayer properties. The last part of the chapter focuses on microscopy techniques and describes our imaging setup, the irradiation power measurements and data analysis.

2.1 Membranes

Membranes are essential components of living systems, separating the cytoplasm from the external environment, but also surrounding the cell organelles. The matrix of the cell membrane is a phospholipid bilayer and contains proteins and other molecules (Fig. 2.1). Membranes, which are only 5 nm thick, are much more than only boundaries. Indeed, they have a functional role, regulating the passage between the internal and the external medium, maintaining concentration gradients and hosting metabolic and biosynthetic activities like adhesion or signaling cascades.

Their composition and asymmetry changes significantly from one cell to another, depending on their function. Surprisingly even in a simple prokaryotic organism such as *Escherichia Coli* (*E. Coli*), there are as many as hundreds of phospholipid species. However, the necessity of such a large number of different lipid species is not yet

understood.

Another characteristic of membranes is their high flexibility. They are able to deform under external perturbations such as elastic or viscous stresses. Red blood cells, for example, can strongly deform when they travel through capillary vessels without losing their structural integrity [69].

Different models were made to describe membranes, like the fluid mosaic from Singer and Nicolson [70], further improved by Israelachvili [71] in 1978 and by Sackmann in 1995 including the importance of the cytoskeleton. A new aspect of cell membrane structure is presented by Simons and Ikonen [72], based on the dynamic clustering of sphingolipids and cholesterol to form rafts that move within the fluid bilayer. It is proposed that these rafts function as platforms for the attachment of proteins.

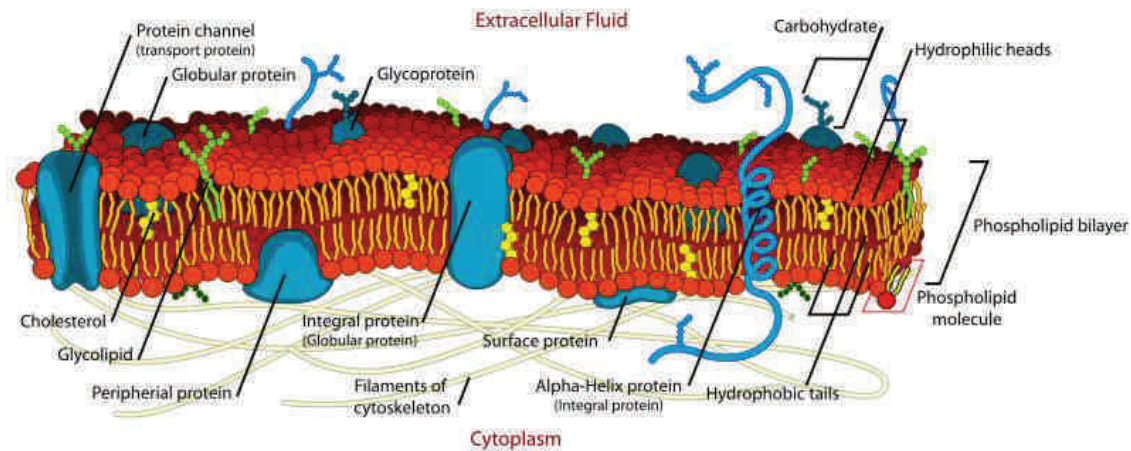


Figure 2.1: Schematic illustration of a cell membrane and its components (source: <http://cellbiology.med.unsw.edu.au>).

In the three last decades, artificial model membranes have been widely studied. The first studies on the physical properties of these intriguing 2D soft objects have now evolved to account for the presence in the membrane of molecules that provide for function. Mixed systems, made of a model lipid membrane hosting one single active moiety, such as a protein, are nowadays used to elucidate some of the complex biological functions at play during the life of a cell.

2.1.1 Amphiphilic molecules

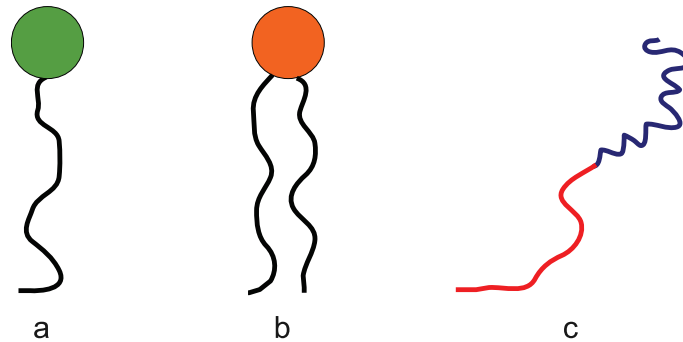


Figure 2.2: Scheme of amphiphilic molecules: (a) Molecule composed of only one aliphatic chain (e.g. SDS), (b) Molecule composed of two aliphatic chains (e.g. Phospholipids), (c) Diblock copolymer.

Amphiphilic molecules are made from a hydrophilic part and a hydrophobic one (Fig. 2.2). Thus, they show a lipophilic and a hydrophylic character. Their hydrophilic part is composed of one or more aliphatic carbon chains, saturated or not. The hydrophilic head determines in which family the molecule belongs to: ionic species, ampholytes or block copolymers... This part can be either neutral, zwitterionic, positively or negatively charged. Thanks to these properties, amphiphiles are able to absorb at interfaces.

Phospholipids

Phospholipids are the most common structural lipids in cell membranes. The glycerophospholipids are amphiphilic molecules made of a phosphate containing hydrophilic head, connected to two hydrophobic tails by a glycerol group. The carbon chain length varies between 10 and 20 methylene units and may be unsaturated. Fig. 2.3 shows four PC phospholipids: DMPC with saturated chains made of 14 carbons, DSPC with saturated chains made of 18 carbons, POPC with one saturated chain of 16 carbons and a mono-unsaturated one of 18, and DOPC with two mono-unsaturated chains of 18 carbons.

The main transition temperature (see below) decreases as the lipid carbon chains are getting shorter (Table 2.1). Presence of unsaturations also decreases this temperature but it increases the risk of phospholipid oxidation.

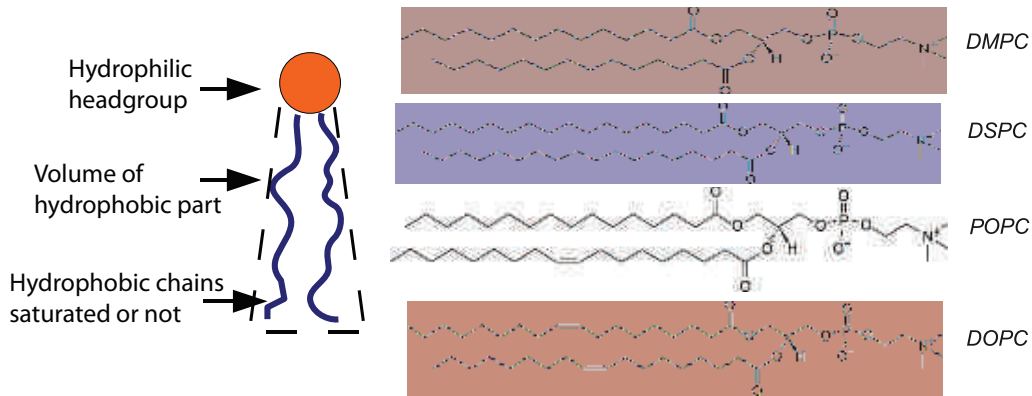


Figure 2.3: Schematic representation of a phospholipid (left). Chemical structures of four PC phospholipids, completely saturated (DMPC and DSPC), with one chain mono-unsaturated (POPC) and with the two chains mono-unsaturated (DOPC).

Notation	number of carbons	number of unsaturated chains	T_m
DSPC	18/18	0	55°C
DMPC	14/14	0	23°C
POPC	18/16	1	-2°C
DOPC	18/18	2	-20°C

Table 2.1: Characteristics of common phospholipids: chain length, presence (or not) of unsaturations and main transition temperature.

Cholesterol

Cholesterol (Fig. 2.4) is a lipid which is very different from phospholipids. Its hydrophobic part is made of a steroid ring structure, whereas its polar head is only made from a hydroxyl (-OH) group. This molecule is almost planar and relatively rigid as the fused rings forbid rotation around C-C bonds. Its insertion in membranes modifies their physicochemical properties. Its preference for having conformationally ordered lipid chains around it increases the degree of orientational order in liquid-disordered phases, leading to membrane increased mechanical strength and lower permeability [73].

Recent studies have shown that cholesterol plays an important role in the formation of the so-called lipid rafts which can be considered as small, cholesterol enriched, liquid ordered phase micro-domains in biological membranes [74]. Some membrane

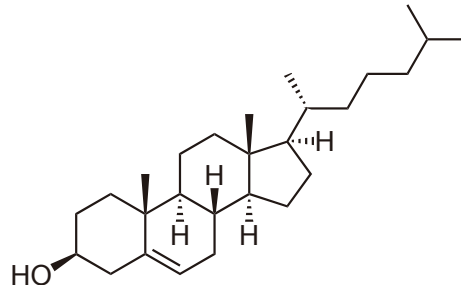


Figure 2.4: Chemical structure of cholesterol.

proteins are found to accumulate in these domains that appear to be important in cell signaling, molecular trafficking and other cellular processes.

2.1.2 Self-Assembly

When amphiphilic molecules are dispersed in water, they tend to minimize the energetically unfavorable interactions between aliphatic chains and water, by migrating for instance to the water/air interface with the hydrophilic head in the water and the hydrophobic chains in the air. In the bulk, for low concentrations, the amphiphiles are dispersed as monomers, but over a certain threshold, the critical micellar concentration ($\text{cmc} \sim 10^{-10} \text{ mol L}^{-1}$ for lipids [75]), they self-assemble to form supramolecular structures.

Such structures result from a competition between two forces: the attractive interaction between carbon chains, which tends to minimize the interface chains/water, and a repulsive interaction between the polar heads, which tends to increase the water/head contact area. Israelachvili [75] derived the total energy, showing that it exhibits a minimum at an optimal surface area a_0 (Fig. 2.5), which should not depend strongly on the chain length or the number of chains.

For a lipid with a head area a_0 , the hydrocarbon chain occupying a volume V and a chain length l , the value of the packing parameter (or structure factor) $V/(a_0l)$ indicates the type of the self-assembled structure that is formed. Simple geometry arguments give (see Fig. 2.6):

- $V/(a_0l) < 1/3$ leads to spherical micelles;
- $1/3 < V/(a_0l) < 1/2$ leads to cylindrical micelles;

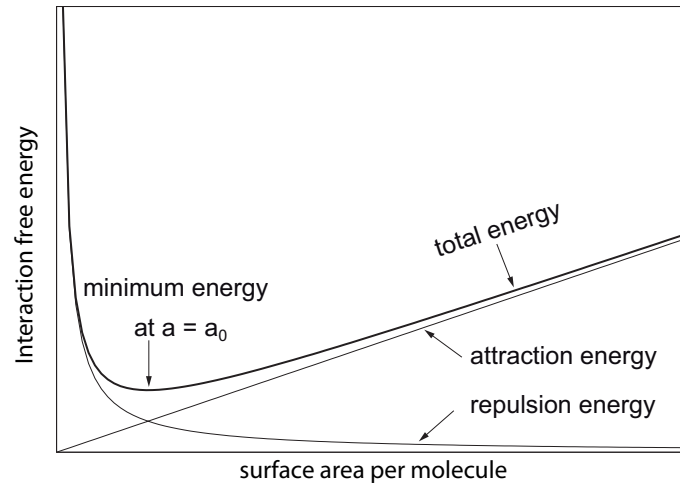


Figure 2.5: An optimal surface area a_0 is derived from the minimum of the total energy, for which the attractive energy (hydrophobic interaction between chains) and the repulsive energy (repulsion between head groups) are balanced.

- $1/2 < V/(a_0l) < 1$ leads to vesicles or bilayers;
- $V/(a_0l) > 1$ leads to inverted micelles.

In water, the “cylindrical shape” of phospholipids induces the preferred formation of structures with low radius of curvature. This leads to an aggregation into bilayers, composed of two monolayer films with opposite orientation, forming vesicles or lamellar phases. They can be regarded as essentially 2-dimensional systems with a thickness of around 5 nm and a lateral extension of the order of micrometers.

Depending on the volume occupied by the phospholipid and the temperature, the lipid mobility in bilayers changes drastically. Membrane phase transitions (Fig. 2.7) are observed [76] and the transition temperatures are specific of each lipid, depending especially on the hydrophobic tails structure.

- At very low temperatures, the molecules form a crystalline structure (phase L_c). They display a long range order and vanishing diffusion.
- Above the crystal/gel transition temperature, the bilayer is in the gel phase (phase L_β). The long range order disappears, but an orientational order still remains, as carbon chains are aligned in a condensed state. The C-C bonds have a high probability to display anti conformations, so that the thickness

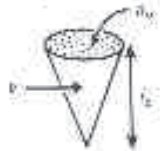
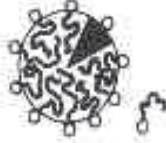

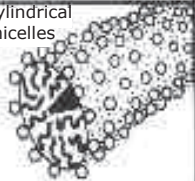

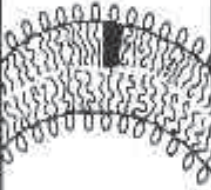



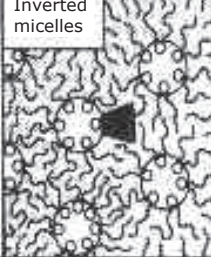
Lipid	Critical packing parameter	Critical packing shape	Structures formed
Single-chained lipids with large head-group areas : SDS in low salt	$< 1/3$	Cone 	spherical micelles 
Single-chained lipids with small head-group areas : SDS and CTAB in high salt, nonionic lipids	$1/3 \leq v$	Truncated cone 	cylindrical micelles 
Double-chained lipids with large head-group areas, fluid chains : Phosphatidyl choline, phosphatidyl serine, phosphatidyl glycerol, phosphatidyl acid, sphingomyelin,...	$1/2 \leq v < 1$	Truncated cone 	Flexible bilayers, vesicles 
Double-chained lipids with small head-group areas, anionic lipids in high salt, saturated frozen chains : phosphatidyl ethanolamine	$v \approx 1$	Cylinder 	Planar bilayers 
Double-chained lipids with small head-group areas, nonionic lipids, poly(cis) unsaturated chains, high T : unsat. phosphatidyl ethanolamine,...	$v > 1$	Inverted truncated cone or wedge 	Inverted micelles 

Figure 2.6: Different structures obtained depending on the shape of the amphiphilic molecule [75].

of the bilayer is maximal. Molecules start to diffuse with typical diffusion coefficients lower than $10^{-2} \mu\text{m}^2/\text{s}$.

- Above the gel/fluid transition temperature, also called main transition, the bilayer is in the fluid phase, L_α . A strong disorder of the chains leads to a thinning of the membrane. Lateral mobility of the lipids increases and their diffusion coefficient is about 1-10 $\mu\text{m}^2/\text{s}$.
- For some lipids, a pre-transition occurs before the main transition and a so-called ripple phase (P_β) is observed [76, 77].

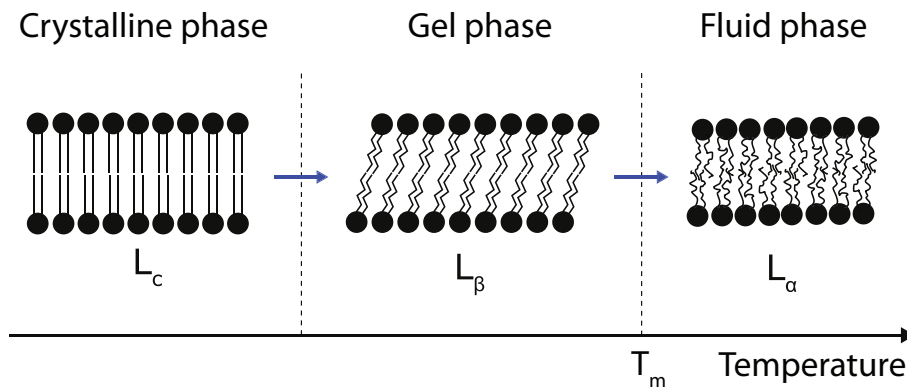


Figure 2.7: Schematic illustration of the different phases observed with temperature: crystalline, gel and fluid.

2.2 Model systems

2.2.1 Lipid monolayers

A mono-molecular layer, called Langmuir monolayer, can be obtained by spreading water insoluble amphiphiles, like phospholipids at the water-air interface. Such films can be compressed on a Langmuir balance, by tuning the area of the interface (A) thanks to a mobile barrier. The monolayer pressure (Π) can be continuously monitored upon compression, providing a measurement of the $\Pi(A)$ isotherms. Compression drives the monolayer through a 2D analogue of the well known states of matter in 3D: solid, liquid and gas.

An example of isotherm is shown in Fig. 2.8, where different states can be observed. Upon compression, at constant temperature, the monolayer undergoes several state transitions in the following order: gaseous phase, liquid expanded, liquid

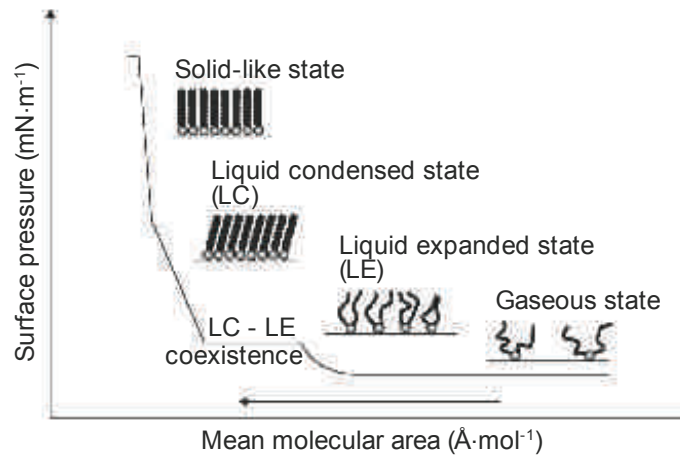


Figure 2.8: $\Pi - A$ isotherm obtained by compressing an insoluble lipid monolayer formed at an air-water interface [78]. Upon compression, the lipid monolayer state changes from gaseous state, to liquid expanded (LE), liquid condensed (LC) and finally to solid state

condensed and finally solid-like state. For higher compression, the film may eventually collapse.

This monolayer model system is a practical tool mimicking half of a real membrane and allows characterization of drug-lipid and lipid-lipid interactions at a molecular level. The main limitation of this model is the high surface tension at water-air interface, due to the large contact between carbon chains and air. Thus, surface tension is relatively high and it is difficult to achieve a comparable area per molecule as present in real membranes, where surface tension is almost zero [79].

2.2.2 The lipid bilayer

Lipid bilayers are simple models for real cell membranes. Supported bilayers can be obtained from compressed Langmuir monolayers.

Supported bilayers

The so-called Langmuir-Blodgett technique consists in the deposition of two monolayers on a substrate. This technique allows an asymmetric preparation of the bilayers (different leaflet composition). The principle is that the substrate crosses a first time the water-air interface so that a first monolayer deposits on it. A second

crossing of the interface allows the deposition of a second monolayer and thus the formation of a supported bilayer (Fig. 2.9). The depositions are done under a constant surface pressure, typically around 40 mN/m, in order to achieve preferred molecular areas comparable with real membranes and avoid any defects during deposition.



Figure 2.9: Scheme of the Langmuir-Blodgett deposition technique. The glass slide is taken out of the water subphase, inducing the deposition of a first lipid monolayer. By returning to the water phase and crossing a second time the interface, a second monolayer is deposited, leading to a supported bilayer.

Supported bilayers can also be formed by vesicle fusion. Small unilamellar vesicles (see below) are formed and put in contact with a hydrophilic substrate. They adsorb and burst on the surface leading eventually to the formation of a bilayer [80].

Such supported bilayers are very stable and stay intact even if subjected to high flow rates or vibrations. This allows them to be studied with a large spectra of techniques like Atomic Force Microscope (AFM) or Surface Force Apparatus (SFA), allowing to probe nanomechanical properties and interactions between membranes. Their 2D geometry makes them also very attractive for scattering experiments [81, 82].

Vesicles

The edges of a 2D flat membrane are energetically unfavorable due to carbon chain exposure to water. One possibility for the membrane is to close itself to form a capsule, which is called a vesicle. Vesicles can be either unilamellar (liposomes) or multilamellar, displaying an onion-like structure [83]. Different sizes exist spanning dimensions from some nanometers to tens of microns. Three main families of unilamellar systems can be distinguished:

- SUVs (Small Unilamellar Vesicles) or liposomes from 20 to 100 nm;
- LUVs (Large Unilamellar Vesicles) from 100 nm to 500 nm;
- GUVs (Giant Unilamellar Vesicles) from 500 nm to 100 μm .

The vesicles can form spontaneously by hydration of a lipid film, but sizes and shapes are usually not very well controlled. This difficulty can be solved by applying an oscillatory electric field during the hydration phase [84], leading to a large quantity of spherical GUVs (Fig. 2.10). More details about the experimental procedures for vesicle formation used in this work (GUVs and liposomes) are described in Appendix A.4.

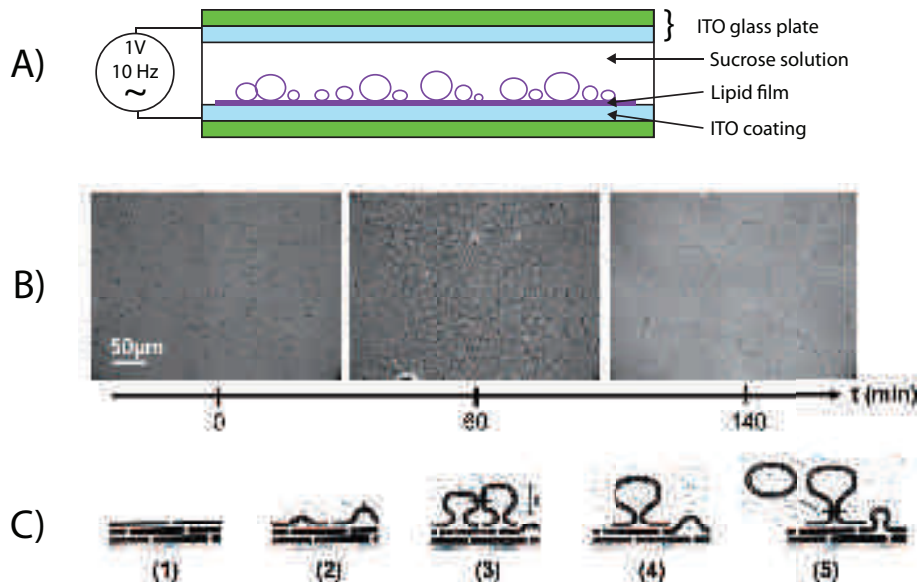


Figure 2.10: Scheme of the cross section of the electroformation chamber (A). Formation and growth of the vesicles as a function of time (B) and possible mechanism (C). After two hours, a large amount of GUVs is observed (adapted from [85]).

2.3 Bilayer properties and micropipette experiments

2.3.1 Lipids on the move

Lipid molecules in a liquid state bilayer exhibit a variety of different motions: changes of intra-molecular conformations, wobbling, protrusion out of the bilayer, diffusion [86] (see Fig. 2.11). All these motions range over an enormous time span. Conformational changes occur on the timescale of 10^{-12} s, rotations in about 10^{-9} s, and lateral diffusion over a lipid size is in the range of 10^{-6} s.

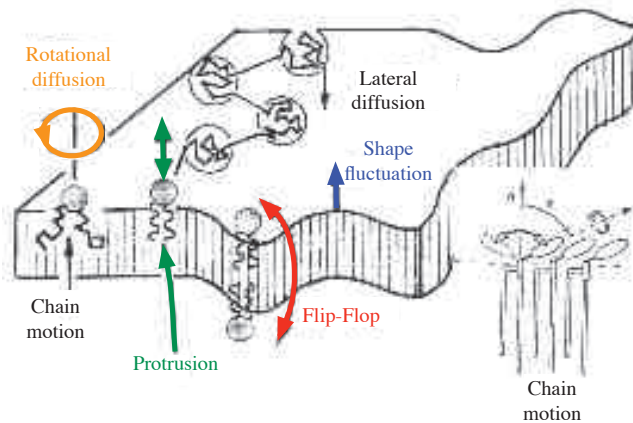


Figure 2.11: Individual lipid movement in a bilayer, chain motion, rotation along the long axis, protrusion, lateral diffusion and flip-flop [87].

The fast mobility of lipids in the membrane plane is a specificity of liquid state bilayers. Typically, the diffusion coefficient is $D \sim 1\text{-}10 \mu\text{m}^2 \text{s}^{-1}$ [88,89], so that a lipid molecule is able to explore the whole membrane, for a usual cell size, in less than 30 s. For a membrane in the gel phase, the diffusion is decreased to $D < 10^{-2} \mu\text{m}^2 \text{s}^{-1}$ [90]. The lateral diffusion of lipids can be measured by different techniques: FRAP and FRAPP (Fluorescence recovery after (patterned) photobleaching) [91], FCS (Fluorescence Correlation Spectroscopy) [92,93] or even single particle tracking [94].

Motion of molecules from one leaflet to the other one is also possible. This energetically unfavored process, called flip-flop, is relatively slow, e.g. on the timescale of several days. However, in real cells, it can be catalyzed by enzymes (flippases) and the flip-flop probability increases by 10^4 times. In synthetic membranes, it can

also be induced by the formation of a pore [95].

In addition to the previous individual modes of lipid motion, collective motion involving many lipids takes also place, like bilayer undulations, thickness fluctuations, collective diffusion of clusters in the membrane plane.

2.3.2 Membrane permeability

An important role of lipid bilayers is to act as a permeability barrier and therefore to selectively filter the various kinds of molecules. The cell uses preferentially specific membrane-bound channels to control precisely the traffic across the membrane, but depending on the molecule size and their affinity with hydrophobic chains, some molecules can directly cross the membrane. The membrane is highly permeable to water and uncharged, small molecules, while it is impermeable to ions, most polar molecules, and larger, uncharged molecules.

Gaseous molecules such as CO_2 or O_2 [96] readily dissolve in the hydrophobic chains and cross the membrane by simple diffusion. Water, as well, diffuses rapidly with a permeability between $30\text{-}150 \mu\text{m s}^{-1}$ [97], whereas sugars (glucose and sucrose) can almost not cross lipid membranes. For small ions (Na^+ , K^+ , ...), the energy barrier for crossing the bilayer is around $100 k_B T$ [86], allowing the cell to maintain its electrochemical potential.

2.3.3 Membrane deformation modes

From a macroscopic point of view, at length scales larger when compared to the molecular size, the phospholipid bilayer appears like a 2D object with interesting mechanical properties. We will present in this part the different deformation modes of the bilayer, as sketched in Fig. 2.12.

Stretching deformation

The first lateral deformation is the extension-compression. The energy (per membrane unit surface) depends quadratically on the area variation and can be written:

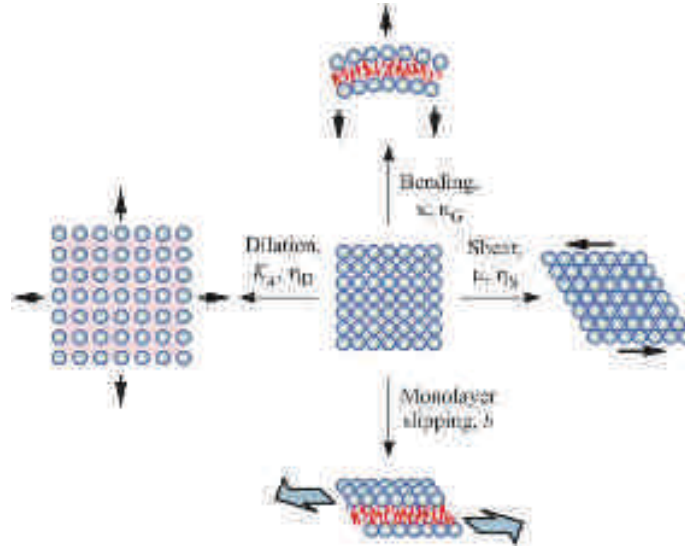


Figure 2.12: Schematic presentation of some classical modes of bilayer deformations: dilation, bending, shear, monolayer slipping; and the constants characterizing the membrane response to these deformations [98].

$$H_{ext} = \frac{1}{2} K_A \left(\frac{\Delta A}{A} \right)^2,$$

where K_A is the membrane stretching modulus.

This deformation is limited for lipid bilayers (1-2%) because of the lysis tension. For tension values higher than σ_{lysis} , a pore opens in the membrane, leading possibly to membrane destruction.

Bending deformation

In the seventies, Canham and Helfrich recalled that the following elastic energy (Eq. 2.1) is associated with the bending of an elementary surface dA characterized by its two curvatures c_1 and c_2 .

$$dH_{bend} = \left(\frac{1}{2} k_c (c_1 + c_2 - c_0)^2 + \frac{1}{2} \kappa_G c_1 c_2 \right) dA \quad (2.1)$$

Here k_c and κ_G are respectively the mean bending modulus and the gaussian bending modulus, c_0 is the spontaneous curvature of the bilayer in absence of external strain. In the case of a symmetric membrane, the two spontaneous curvatures of the monolayers compensate and the bilayer has a net zero spontaneous curvature.

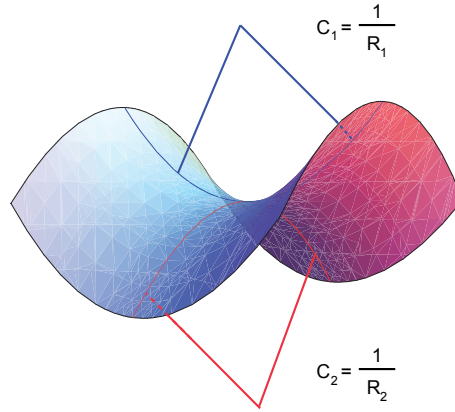


Figure 2.13: Curvatures on a 2D surface. Here the saddle form with $c_1 > 0$ and $c_2 < 0$.

The total bending energy of the membrane is the integral of dH_{bend} over the whole area of the object. According to the Gauss-Bonnet theorem, the gaussian curvature $c_1 c_2$ integrated over the whole surface of a vesicle is a topological invariant, so that it can be ignored for vesicles keeping the same topology.

Surface tension

Another important macroscopic parameter is the membrane lateral tension σ . If a membrane of area A is stretched to an area $A + \Delta A$, there is a resulting restoring force per unit length proportional to ΔA : the surface tension σ . We recover the classical definition of the surface tension: $\sigma = \partial F / \partial A$, where F is the membrane free energy. Thus, we can introduce an energy term (per unit surface) related to the surface variation for a tense membrane:

$$H_{tens} = \sigma \frac{\Delta A}{A}.$$

According to this definition for the tension, $\sigma = K_A \Delta A / A$. However, due to membrane fluctuations, the relation between the tension and the stretching of the

membrane is more subtle, involving both the stretching modulus and the bending modulus.

Thermal fluctuations

In the case of thermal fluctuations of a lipid bilayer, it is often possible to assume that the fluctuations display small amplitudes. Therefore the topology of the system is not modified and the integral of the gaussian bending modulus term is zero. Thus, it is really convenient to use the classical representation of Monge, where $u(x, y)$ is the membrane position compared to a reference plane (see Fig. 2.14).

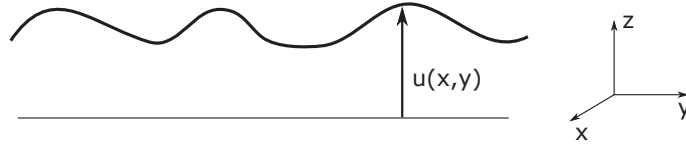


Figure 2.14: Monge representation: the height of the membrane is defined compared to a reference plan. The coordinates of the membrane are $(x, y, u(x, y))$.

The free energy of the membrane can be written as [99]:

$$F = \int \frac{1}{2} \sigma (u_x^2 + u_y^2) + \frac{1}{2} k_c (u_{xx} + u_{yy})^2 dx dy$$

where $u_i = \partial u / \partial i$ and $u_{ii} = \partial^2 u / \partial i^2$ (with $i = (x, y)$).

In Fourier space, we can define

$$u(\mathbf{q}) = \frac{1}{\sqrt{A}} \int d^2 \mathbf{r} u(\mathbf{r}) e^{-i \mathbf{q} \cdot \mathbf{r}}$$

so that

$$u(\mathbf{r}) = \frac{1}{\sqrt{A}} \sum_{\mathbf{q}} u(\mathbf{q}) e^{i \mathbf{q} \cdot \mathbf{r}}.$$

The free energy takes then the classical form of Canham-Helfrich [100, 101]

$$\begin{aligned}
 F &= \frac{1}{2} \sum_{\mathbf{q}} (\sigma q^2 + k_c q^4) |u(\mathbf{q})|^2 \\
 &= \sum_{\mathbf{q}} F_q.
 \end{aligned}$$

The different modes are quadratic and independent, the equipartition theorem thus gives for each mode $\langle F_q \rangle = k_B T/2$, so that:

$$\langle |u(\mathbf{q})|^2 \rangle = \frac{k_B T}{\sigma q^2 + k_c q^4} \quad (2.2)$$

where $\langle |u(\mathbf{q})|^2 \rangle$ is the average amplitude of the fluctuations of the Fourier mode \mathbf{q} .

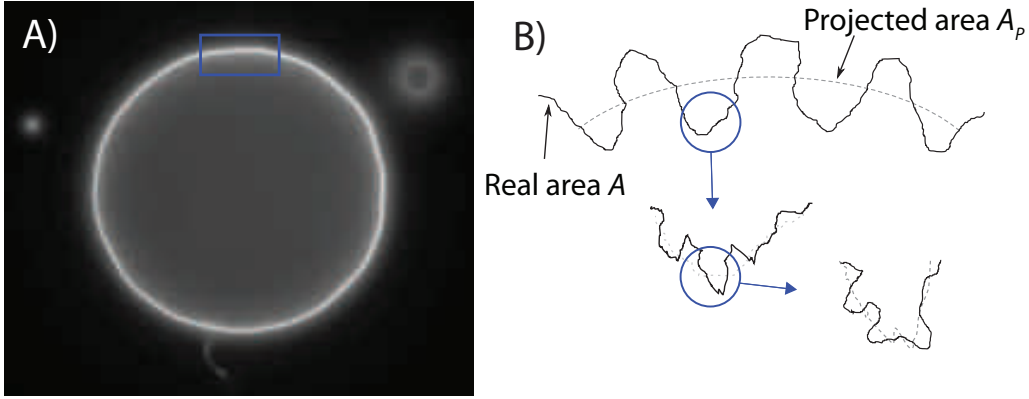


Figure 2.15: (A) Fluctuating GUV made of DOPC in fluorescence mode. (B) Schematic representation of a fluctuating membrane. The dashed line represents the projected area (A_p) and the black line the real area (A).

In the fluid phase, typical bending moduli are low, of the order of several $k_B T$, so that GUVs are largely deformable objects. Under a microscope, vesicles are not completely tense and display large fluctuations at different length scales, so that the observed area (A_p) does not correspond to the real area (A) of the vesicle (see Fig. 2.15). For each mode q , there is a surface excess $\alpha_q = \Delta A/A_q$, and thus by integrating Eq. 2.2 over all the fluctuation modes q , one can calculate the surface excess due to fluctuations [102]:

$$\begin{aligned}
 \alpha &= \frac{A - A_p}{A_p} = \frac{1}{2} \int_{q_{min}}^{q_{max}} \frac{q dq}{2\pi} \frac{k_B T}{\sigma q^2 + k_c q^4} \\
 &= \frac{k_B T}{8\pi k_c} \ln \frac{\pi^2/a^2 + \sigma/k_c}{\pi^2/L^2 + \sigma/k_c},
 \end{aligned}$$

where a is a microscopic cut-off and L the membrane size. Usually, $\pi^2/L^2 \ll \sigma/k_c \ll \pi^2/a^2$, so that the expression can be simplified, as follows:

$$\alpha = \frac{k_B T}{8\pi k_c} \ln \frac{\sigma_{max}}{\sigma},$$

where $\sigma_{max} = k_c \pi^2 / a^2$.

2.3.4 Micropipette suction experiments

This experiment consists in unfolding the GUV membrane by sucking it into a micropipette and measuring the excess area using the aspirated tongue. The aspiration is done by successive increasing values of pressure inside the micropipette. Different physical mechanisms are involved in the experiment. For small aspiration pressures, the area excess hidden in the membrane fluctuations is unfolded. When all the fluctuations are unfolded, increasing the pressure leads to stretching of the membrane. The technique allows to measure first the bending modulus k_c and then the stretching modulus K_A . There is a limit in the pressure increase where the membrane breaks. This threshold is called the lysis tension and is about 10 mN/m [97].

Several conditions need to be fulfilled in order to analyze the data correctly.

- The volume of the vesicle needs to stay constant during the experiment.
- The membrane should not adhere to the micropipette. A treatment of the pipette with β -casein avoids adhesion in our experiments.
- The temperature needs to stay constant during the experiment.
- There should be no contact with other vesicles that could act as lipid reservoirs [103].

Theory

The real area of a vesicle can not be measured by using optical imaging due to the presence of these sub-optical fluctuations. One can only access the apparent area

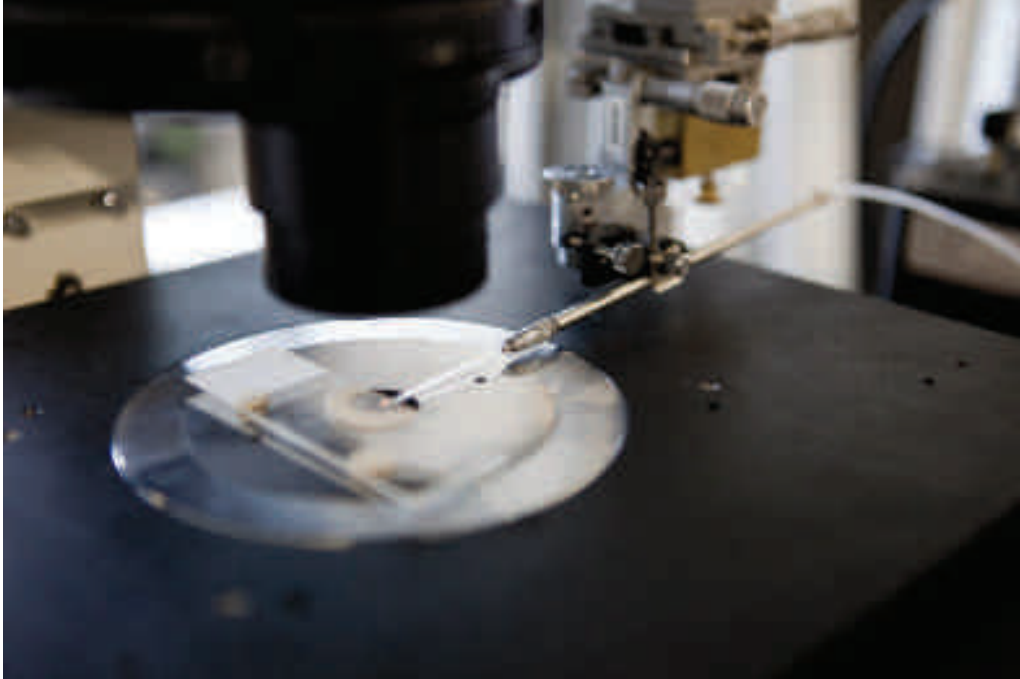


Figure 2.16: Photography of a sample under the microscope. One opened side allows the micropipette to enter into the vesicle solution (photo C. Fresillon).

A_P . To overcome this difficulty, Evans expressed the relative increment of apparent area as a function of the sucking pressure, compared to a well chosen reference state. For two pressures P_1 and P_2 , with $P_2 > P_1$, the relative increment $\Delta\alpha$ can be expressed as:

$$\Delta\alpha = \frac{A_{P_2} - A_{P_1}}{A_{P_1}}. \quad (2.3)$$

By introducing the real area A in equation 2.3, one ends up with:

$$\Delta\alpha = \frac{\frac{A}{A_{P_1}} - \frac{A}{A_{P_2}}}{\frac{A}{A_{P_2}}} = \frac{\frac{k_B T}{8\pi k_c} \ln \frac{\sigma_2}{\sigma_1}}{1 + \frac{k_B T}{8\pi k_c} \ln \frac{\sigma_{max}}{\sigma_2}}.$$

As the tension of a fluctuating phospholipid vesicle made of DOPC is about 10^{-7} N m^{-1} [104], the denominator is close to unity. Usually, one defines a reference state of vesicle suction corresponding to the minimal pressure for which an aspirated tongue of length L_0 can be measured in the micropipette, so that:

$$\Delta\alpha = \frac{k_B T}{8\pi k_c} \ln \frac{\sigma}{\sigma_{L_0}},$$

where σ_{L_0} is the membrane tension of the reference state.

By adding the membrane extension contribution, that we discussed previously, one ends up with a complete formula between $\Delta\alpha$ and σ , expressed as follows:

$$\Delta\alpha = \frac{k_B T}{8\pi k_c} \ln \frac{\sigma}{\sigma_{L_0}} + \frac{\sigma - \sigma_{L_0}}{K_A}. \quad (2.4)$$

Experimental procedure

Micropipettes were made from borosilicate glass capillaries GC100-15 tubing (Harvard apparatus Ltd., Kent, UK) using a pipette puller (Sutter instruments). A homemade microforge was used to tune their inner diameter to about $5 \mu\text{m}$. Pipettes were coated with β -casein and then filled with the isoosmotic glucose solution. The pipette was then driven to the observation field and brought in contact with a GUV. A negative suction pressure P_{in} was applied through the pipette, thanks to an hydrostatic device. The suction pressure leads to a deformation of the vesicle corresponding to an added membrane tension σ .

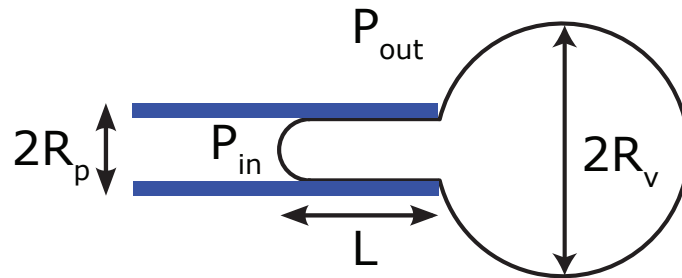


Figure 2.17: Scheme of a vesicle hold by a micropipette and different notations.

The difference of pressure $\Delta P = P_{out} - P_{in}$ inside and outside the vesicle is related to the tension σ . By applying two times the Laplace law:

$$\begin{aligned} P - P_{in} &= \frac{2\sigma}{R_p}, \\ P - P_{out} &= \frac{2\sigma}{R_v}, \end{aligned}$$

where P is the pressure inside the vesicle, P_{in} the pressure inside the micropipette, P_{out} the pressure in the solution, R_v is the vesicle radius and R_p is the pipette radius, one obtains:

$$\sigma = \frac{\Delta P R_p}{2 \left(1 - \frac{R_p}{R_v}\right)}.$$

For each membrane tension σ , we measure the corresponding apparent area increase, $\Delta\alpha$ compared to the reference state defined above. ΔL , R_v and R_p are obtained from image analysis and assuming that $R_v > 4 R_p$ and that the volume of the vesicle stays constant, we obtain the following expression for $\Delta\alpha$:

$$\Delta\alpha = \frac{\Delta L}{2R_p} \left(\left(\frac{R_p}{R_v}\right)^2 - \left(\frac{R_p}{R_v}\right)^3 \right) \quad (2.5)$$

The device allows building the tension versus area expansion curve, showing the two characteristic fluctuation and stretching regimes, as shown in Fig. 2.18, and as described in the literature [105]. The experimental data obtained can be fitted with equation 2.4 to extract the values of the bending modulus k_c and the stretching modulus K_A .

The tension value $\sigma \geq 0.7 \text{ mN m}^{-1}$ corresponds approximately to the transition between the two regimes. For this value of the tension most of the area hidden in the thermal fluctuations is unfolded.

Correction of the apparent area increase

During our irradiation experiments one measures an overall increase of the apparent surface area of a GUV submitted to a constant membrane tension, applied through

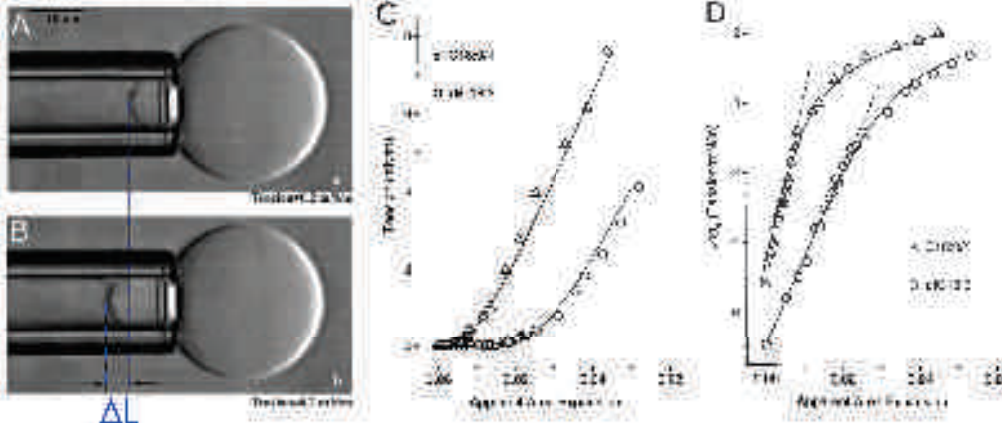


Figure 2.18: Typical vesicle aspiration experiment: as the tension is increased from 0.2 mN/m (A) to 6.2 mN/m (B), a longer tongue is sucked into the micropipette. (C) and (D) display the apparent area increase for several tensions applied, respectively in linear and log representations [106].

the micropipette device. At constant tension, a measure of area increase due to lipid peroxidation is also perturbed by the changes of the stretching modulus of the membrane. Here, we correct for such (minor) perturbations by considering first the Evans-Helfrich equation (Eq. 2.4) for $\Delta\alpha$, the apparent area increase of a membrane submitted to a given tension σ , as a function of its constitutive mechanical parameters, the bending modulus k_c and the elastic modulus K_A .

In the present case, the membrane is subjected to a constant tension σ , and after a time t of illumination, a fraction x_{ox} of the lipids have been peroxidized, leading to a relative area increase $x_{ox}\epsilon$, where ϵ is the relative molecular area increase, and to a decrease of both k_c and K_A . We have measured a linear decrease of K_A with x_{ox} and noticed, without being able for technical reasons to measure it precisely, a decrease in k_c . Then, Eq. (2.4) becomes, after an irradiation time t :

$$\Delta\alpha(x_{ox}) = \frac{k_B T}{8\pi k_c^{\text{eff}}(x_{ox})} \ln\left(\frac{\sigma}{\sigma_{L0}}\right) + \frac{\sigma - \sigma_{L0}}{K_A^{\text{eff}}(x_{ox})} + x_{ox}\epsilon \quad (2.6)$$

with $K_A^{\text{eff}}(x_{ox}) = K_A(1 - x_{ox}) + K_A^{ox}x_{ox}$, where K_A^{ox} is the bending modulus of a completely peroxidized vesicle that we have measured. The maximum error is expected for a fully peroxidized membrane. Assuming a decrease of a factor of four for k_c , $k_c^{ox} = 0.25 k_c$, similar to that measured for K_A , $K_A^{ox} = 0.25 K_A$, it follows that the

error on the relative area increase $\epsilon(x_{ox} = 1)$, is less than 1% for a membrane submitted to a tension $\sigma = 0.7 \text{ mN m}^{-1}$. One can notice that the relative error remains smaller than one percent if k_c^{ox} assumes values in the range $0.25 k_c < k_c^{ox} < k_c$.

2.4 Microscopy

2.4.1 Experimental setup

Irradiation and observation of giant vesicles were performed under an inverted microscope, TE2000 (Nikon, Japan), equipped with a 60X water immersion objective. Vesicles were irradiated with light from a HBO 103W Hg lamp of the microscope, with an excitation filter centered at 414 nm and a long pass filter (high transmission $> 98\%$ between 530 and 700 nm) was used to collect emission light (see Appendix A.3). Observation of the vesicles without irradiation was performed in phase-contrast and in DIC mode. All images were taken with a digital camera (Hamamatsu EM-CCD, Japan) at a rate of 8 frames per second, and analyzed using a homemade software.

2.4.2 Power measurement by chemical actinometry

In order to precisely know the number of photons reaching the samples, we use the ferrioxalate actinometer described by Hatchard and Parker [107]. We prepare a 0.15 M solution of ferrioxalate. We pipet $V_1 = 6 \text{ mL}$ of that solution and put it in the cylindrical cell made from a Teflon cylinder stuck to a round and thin glass slide (Fig. 2.19). Light irradiation is done during a certain time and we check that all light is absorbed by the solution. After irradiation, the solution is stirred for a minute. Then, we pipet $V_2 = 1 \text{ mL}$ from it, add 1.5 mL of buffer, 2 mL of the concentrated phenanthroline solution and fill up to $V_3 = 20 \text{ mL}$ with mQ water. The solution is kept in the dark until absorbance measurement at 510 nm.

Irradiation leads to iron reduction (+III to +II). We measure the number of Fe(II) produced under irradiation by complexing them with excess of 1,10-phenanthroline and measuring absorbance spectra. The experiment is repeated for several irradiation times (Fig. 2.20).

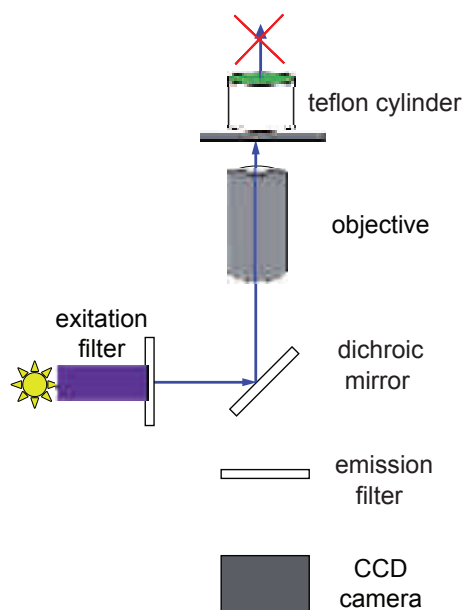


Figure 2.19: Scheme of the chemical actinometry setup allowing to measure the number of photons impinging the sample in the experiment conditions.

The absorbance at 510 nm (ΔA_{510}) is expressed as follows:

$$\Delta A_{510} = \frac{V_2 l \epsilon_{510} \phi_{act} N_{photons/t}}{N_A V_1 V_3} t_{irrad},$$

where $\epsilon_{510} = 1.1 \cdot 10^4 \text{ L mol}^{-1} \text{ cm}^{-1}$, l is the absorbing path length (1 cm), V_1 the total volume of the irradiated solution (6 mL), V_2 the volume of irradiated solution taken for titration (1 mL) and V_3 the final volume after dilution, ready for absorbance measurements (20 mL), $\phi_{act} = 1.12$ is the quantum yield of the actinometer at irradiation wavelength [107], t_{irrad} is the irradiation time and $N_{photons/t}$ is the number of photons per unit time arriving in the sample.

The value of $N_{photons/t}$ is extracted from the slope in Fig.2.20 and the power of the lamp is thus given by:

$$P = N_{photons/t} \frac{hc}{\lambda}.$$

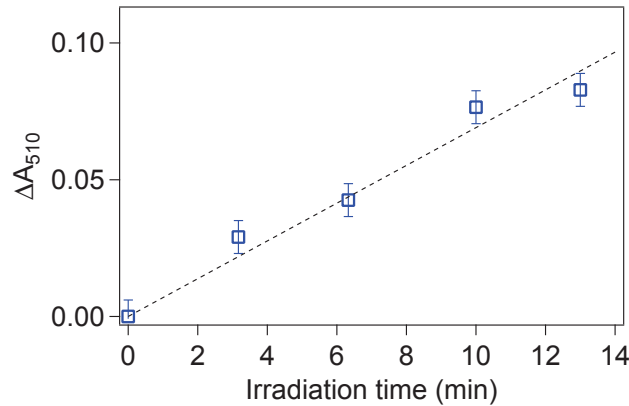


Figure 2.20: ΔA_{510} as a function of irradiation time for the 60X water immersion objective (\square)

The power per unit surface is simply obtained by dividing by the surface of the image of the diaphragm, so that $P = 10.8 \pm 1.4 \text{ W cm}^{-2}$ under a 60X objective at maximal irradiation intensity. Different optical densities dividing the power by a factor 2, 4, 8, 16 and 32 have been used.

2.4.3 Data analysis

The fluorescence light distribution of a vesicle image collected from the equator focal plane does not only contain light emitted from the equator. Indeed, the light is integrated over a certain depth, so that in the middle of the profile, the measured intensity is not zero (Fig. 2.21).

GUVs decorated with various surface concentrations of Chlorin-12 under continuous irradiation at 410 nm, show a typical fluorescence intensity decrease due to photobleaching (Fig. 2.22).

We checked for our experiments that the ratio of the total fluorescence of the image (I_{fluo}) divided by the square radius of the vesicle (R^2) is constant for vesicles of different sizes. We also made sure, by changing the focus (from the top to the bottom of the vesicle) of the microscope during the irradiation of a vesicle, that the fluorescence intensity decrease curves (due to photobleaching) are continuous and do not show any lag. This confirms that the emitted light collected is representative of the whole vesicle.

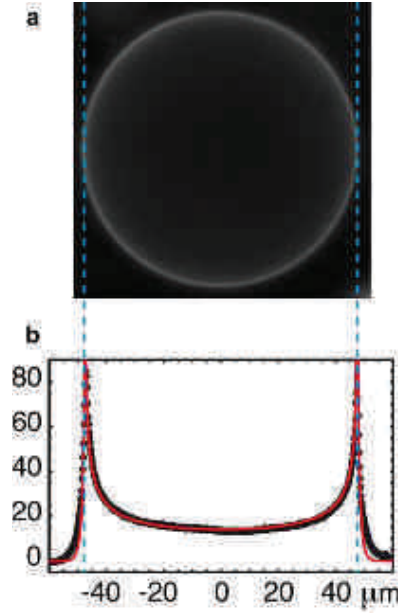


Figure 2.21: Fluorescence intensity profile of a GUV [108].

In order to correlate the collected fluorescence intensity and the production of $^1\text{O}_2$ species we noticed that for a given quantum yield for $^1\text{O}_2$ production ϕ_Δ , the cumulative fluorescence is directly proportional to the number of $^1\text{O}_2$ species produced since the beginning of the irradiation (Eq. 2.7). The constant of proportionality between emitted light intensity and singlet oxygen generation can be computed by noticing that the rate of singlet oxygen production Q is given by [109] $Q = \phi_\Delta \lambda P \sigma / hc$, where λ is the wavelength of the irradiation light (410 nm), P the power density, σ the cross section of absorbance, h the Planck's constant, and c the speed of light.

The total number of $^1\text{O}_2$ produced per lipid at time t , since the beginning of the irradiation, is given by:

$$\text{Total number of } ^1\text{O}_2(t) \text{ per lipid} = Q x_{Ch} \int_0^t I_{norm}(t') dt', \quad (2.7)$$

where x_{Ch} is the fraction of Chlorin-12 in the membrane and I_{norm} is the normalized fluorescence intensity.

Thus, we can compute the cumulative singlet oxygen production and display it

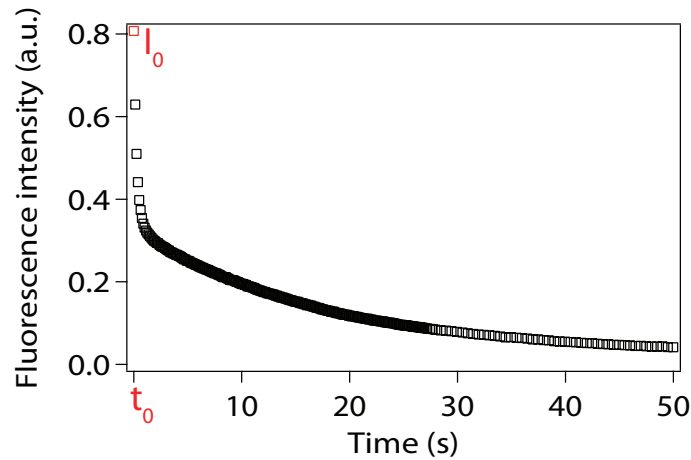


Figure 2.22: Fluorescence intensity decrease (in arbitrary units) of a POPC GUV containing 0.03 % Chlorin-12. The irradiation power is $P = 2.7 \text{ W cm}^{-2}$.

as a function of time (Fig. 2.23).

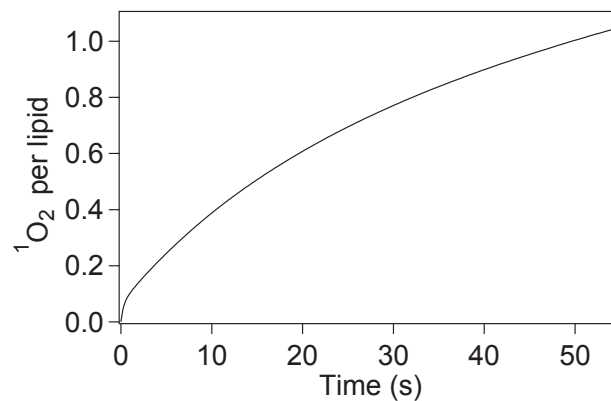


Figure 2.23: Cumulative singlet oxygen production of an irradiated POPC GUV containing 0.03 % Chlorin-12.

A note on the detected light signal: photobleaching of the Chlorin-12 molecules starts immediately when the irradiation is turned on, with a characteristic initial decay time smaller than one second. Thus, the intensity of the first image recorded by the camera was an intrinsic uncertainty related to illumination switch-on times and no triggering of image acquisition. To minimize error, we only selected experiments where illumination switch-on and beginning of photobleaching were captured during the acquisition time of the first image.

The associated relative area increase was measured on each vesicle by a direct analysis of the vesicle dimensions on the fluorescence images, for different irradiation times and further corrected for the associated K_A decrease as explained above.

Chapter 3

Chlorin-12: A new photosensitizer

In this study, $^1\text{O}_2$ was generated by a new synthesized photosensitizer, Chlorin-12, synthesized by the group of M. Baptista, USP, Brazil [17]. An aliphatic chain of twelve carbons was grafted on a Chlorin molecule (Fig. 3.1), designed such that self-aggregation is prevented. Indeed, fluorescence, resonant light scattering (RLS) and ^1H NMR experiments, as well as X-ray crystallography have demonstrated that the arrangements of Chlorin-12 prevent π -stacking interactions between macrocycles. Thus, this is a non-aggregating PS with high quantum yield of singlet oxygen generation (ϕ_Δ) and fluorescence (ϕ_F) [17].

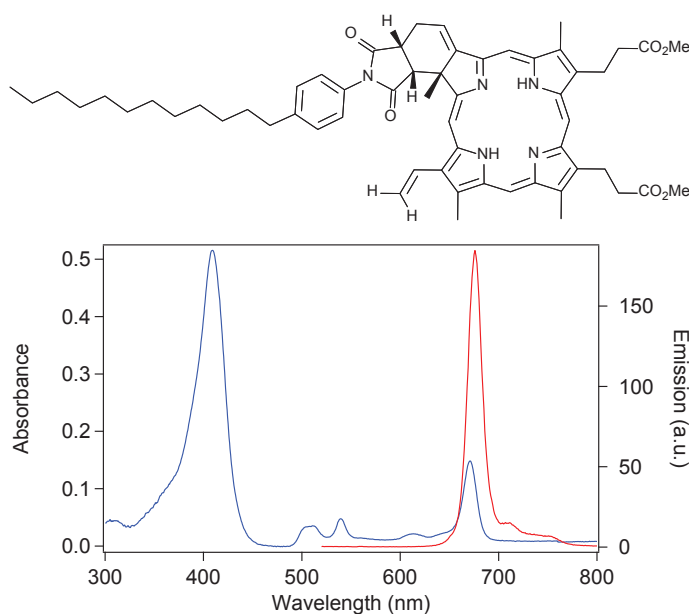


Figure 3.1: Chlorin-12 molecule and its absorption and emission spectra.

3.1 Photophysical and photochemical properties

3.1.1 Triplet state lifetime

We investigated the photochemical and photophysical properties of this PS in solution. The first essential step was to probe its excited states by using laser flash photolysis (LFP). It is a pump-probe technique, in which the sample is first excited by a strong laser pulse, leading to an increased population in the excited states of the molecules. Then, the absorption of light by the sample is recorded within short time intervals to monitor relaxation initiated by the pump laser pulse. More information about the setup used can be found in Appendix A.2.1. We obtain thus ΔAbs which is the difference of absorption compared to the molecules in the ground state (see Fig. 3.2). One can notice the presence of an excited state at 460 nm, corresponding to the triplet state.

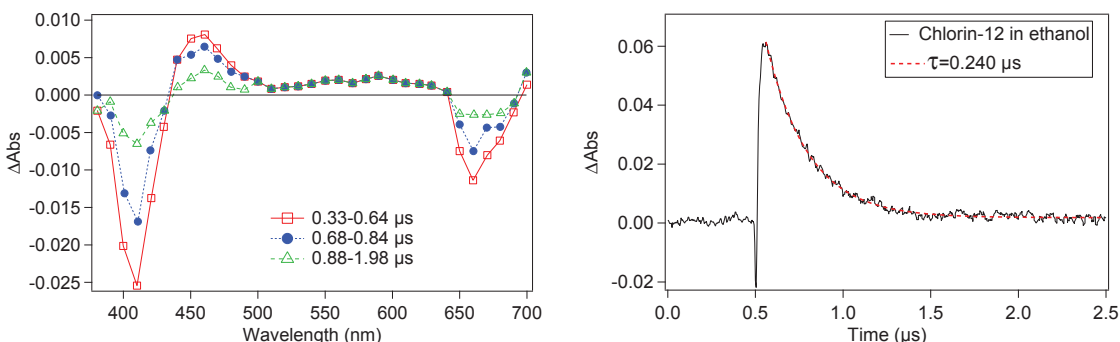


Figure 3.2: Left: ΔAbs spectra of Chlorin-12 in ethanol obtained by laser flash photolysis. The values of absorption are recorded within short time intervals. Presence of the triplet state is confirmed at 460 nm. Right: Triplet state lifetime measurement at 460 nm. The dashed curve corresponds to the exponential fit and gives $\tau_T = 0.240 \mu\text{s}$.

Decay of the triplet state could be measured at 460 nm (Fig. 3.2). It showed an exponential decrease with a characteristic time $\tau_T = 0.240 \mu\text{s}$ in ethanol.

3.1.2 Singlet Oxygen Luminescence (SOL) measurement

We also performed singlet oxygen lifetime measurements in deuterated ethanol. Fig. 3.3 shows $^1\text{O}_2$ production and decay after a short laser pulse excitation (see Appendix A.2.1). Such curves can be fitted [110] using:

$$n_{SO}(t) = \frac{A}{\tau_T^{-1} - \tau_{SO}^{-1}} (e^{-t/\tau_{SO}} - e^{-t/\tau_T}) \quad (3.1)$$

where $n_{SO}(t)$ is the number of singlet oxygen molecules, A a constant, τ_T the triplet state lifetime of the PS and τ_{SO} the singlet oxygen lifetime.

Using the triplet state lifetime $\tau_T = 0.240 \mu\text{s}$, the fit gives $\tau_{SO} = 16.5 \mu\text{s}$ in deuterated ethanol.

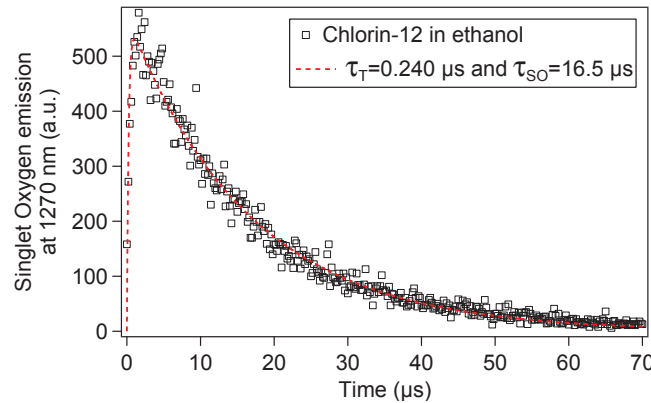


Figure 3.3: $^1\text{O}_2$ luminescence measurement at 1270 nm. Fit with Eq 3.1 leads to $\tau_{SO} = 16.5 \mu\text{s}$

The Chlorin-12 molecule is producing $^1\text{O}_2$ and has therefore the properties of a photosensitizer.

3.2 Chlorin-12 anchored in membranes

3.2.1 Homogeneous incorporation

Chlorin-12 has an amphiphilic character that can be clearly demonstrated by performing Langmuir-Blodgett compression measurements [111] at the air-water interface

where a stable film is formed (Fig. 3.4). The compression isotherms at 20°C show standard monolayer behavior for pressures in the range [5-40] mN m⁻¹.

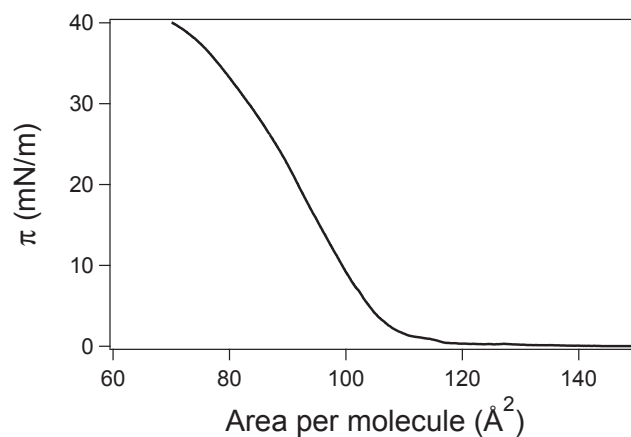


Figure 3.4: Langmuir isotherm of the Chlorin-12 molecule at 20°C.



Figure 3.5: Chlorin-12 containing giant vesicle, both in DIC mode (left) and in fluorescence (right). Colocalization of membrane and fluorescence shows effective Chlorin-12 anchoring.

Colocalization of the fluorescence light distribution with the bilayer position obtained from phase-contrast, bright-field or DIC images, shows that the photosensitizers are anchored in the giant vesicles bilayers (Fig. 3.5). Also, the homogeneous distribution of fluorescence proves that the sensitizer molecules are dispersed in the bilayer at optical length-scales. At the sub-optical lengths molecular dispersion in the bilayer is also supported by the similarity between the absorption light spectra of the probes anchored in small liposomes and the absorption spectra of free Chlorin in solution. The linear variation of the absorbance as a function of Chlorin-12 concentration also supports the non-aggregation nature of the molecule (Fig. 3.6).

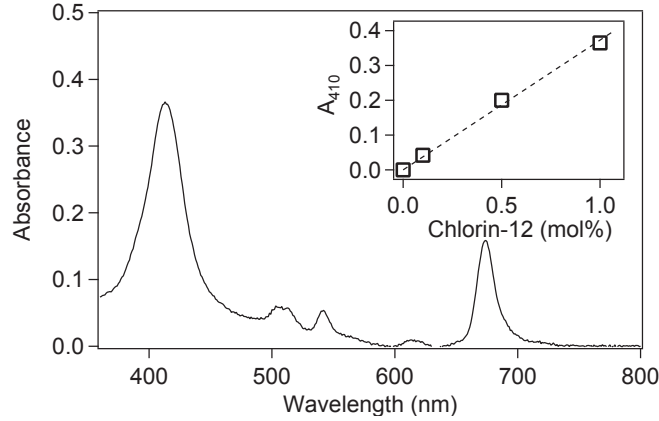


Figure 3.6: Absorption spectra of Chlorin-12 containing liposomes. The inset shows the linear evolution of the absorption peak at 410 nm as a function of Chlorin-12 concentration.

3.2.2 Singlet oxygen production

In order to achieve later on a quantitative study of photo-oxidation phenomena, we were interested in estimating the rate of singlet oxygen production of one photosensitizer. The rate of $^1\text{O}_2$ production Q per photosensitive molecule is given by [109]:

$$Q = \frac{\phi_{\Delta} \lambda P \sigma}{hc}, \quad (3.2)$$

where $\phi_{\Delta} = 0.63$ is the quantum yield of $^1\text{O}_2$ production of the photosensitive molecule, $\lambda = 410$ nm is the wavelength of the irradiation light, $P = 10.8 \pm 1.4$ W cm $^{-2}$ is the maximal irradiation power density measured by chemical actinometry (as described in 2.4.2), $\sigma_{410nm} = 2.1$ Å 2 is the cross section of absorbance, h is the Planck's constant, and c is the speed of light.

Thus, in our setup, each Chlorin-12 generates around 2950 $^1\text{O}_2$ s $^{-1}$ at maximal irradiation power. However, several neutral filters have been used to divide the power by a factor 2, 4, 8, 16 and 32, leading to a $^1\text{O}_2$ production divided by the same corresponding factors.

3.2.3 Chlorin-12 diffusion coefficient in fluid membranes

Once effective incorporation of the PS in the membrane has been achieved, one might wonder how these molecules homogenize with time. We decided to perform a FRAP (Fluorescence recovery after photobleaching) experiment to measure lateral diffusion of Chlorin-12 molecules in the bilayer. Some FRAP experiments allowing very precise measurements already exist [91]. Here, we do not need such a high precision and decided then to perform a FRAP measurement under the microscope.

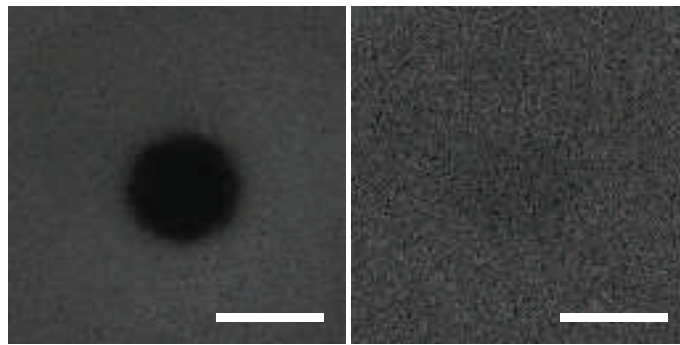


Figure 3.7: Fluorescence image of the supported bilayer made of POPC and Chlorin-12 (0.1 mol %) at $t = 11$ s, the photobleached region is black (left) and $t = 1700$ s, recovery occurred (right). The bar size is $40 \mu\text{m}$.

Supported bilayers made of POPC and containing a fraction of Chlorin-12 molecules (0.1 mol %) were made with the Langmuir-Blodgett deposition method (see 2.2.2). The sample was placed under microscope and a circular zone of area πa^2 was photobleached at maximal light intensity (Fig. 3.7). Then, the diaphragm was opened, and the lamp intensity lowered in order to record the fluorescence recovery. Images have been taken every 3 minutes, the lamp being turned off between each image capture. Intensity difference $F(t)$ between the non photobleached region $I(r>a,t)$ and the center of the photobleached region $I(r=0,t)$ can be plotted (Fig. 3.8) as a function of time.

Analysis of the fluorescence recovery (see Appendix A.1) shows that the Chlorin-12 molecules have a diffusion coefficient of $D \sim 0.3 \pm 0.1 \mu\text{m}^2\text{s}^{-1}$. This value is between the mobility of lipids in a gel state and in a fluid state bilayer. It is low considering a fluid membrane, as fluorescent lipid probes diffuse with typical values of $D \sim 2 - 20 \mu\text{m}^2\text{s}^{-1}$ [91]. As the concentration of Chlorin-12 used is low enough (0.1 mol %), this diffusion value cannot be explained by diffusion of small Chlorin-12

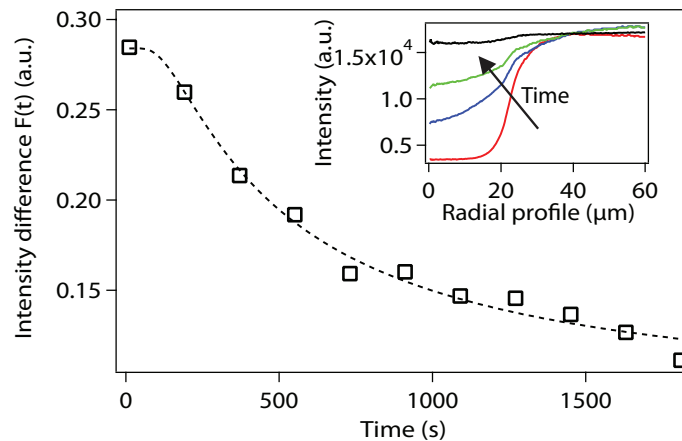


Figure 3.8: Intensity difference $F(t)$ between the non photobleached region and the center of the photobleached region. The intensity difference is lowering with time as the recovery takes place. The inset shows the radial profiles and their evolution with time.

aggregates. The shape of the molecule or a specific interaction with the substrate, which can reduce the mobility in the proximal leaflet, could explain such a low value. Nevertheless, a complete study of diffusion coefficient evolution with the Chlorin-12 concentration would be of interest here. However, this value is high enough to achieve an efficient homogenization of Chlorin-12 molecules in the conditions of our later studies.

3.3 Behavior under light exposure

Photobleaching of the photosensitizers is one of the limitations in PDT treatments. We already enumerated previously some of the different pathways leading to molecules bleaching. We decided to investigate how our system reacts under light irradiation by using two different setups: single GUVs under microscope and liposome solutions.

3.3.1 PS chemical modification and photobleaching

GUV under microscope

When Chlorin-12 containing vesicles made from POPC and DOPC are continuously irradiated under microscope, the emitted fluorescence decreases as a function of the irradiation time. Typical decay is displayed in Fig. 3.9 for different concentrations of Chlorin-12. The filters used were 414/46 nm for excitation and a long pass filter, above 519 nm, for emission (see Appendix A.3).

In various photobleaching studies, the fluorescence intensity decay is exponential, e.g. for PE-Porph [57]. With Chlorin-12, the decay shows a double exponential behavior at low concentrations of PS. More strikingly, at higher concentrations, the curve displays an intermediate plateau and in some cases, the intensity even increases before the final decrease. There is an evident effect of concentration on the photobleaching behavior.

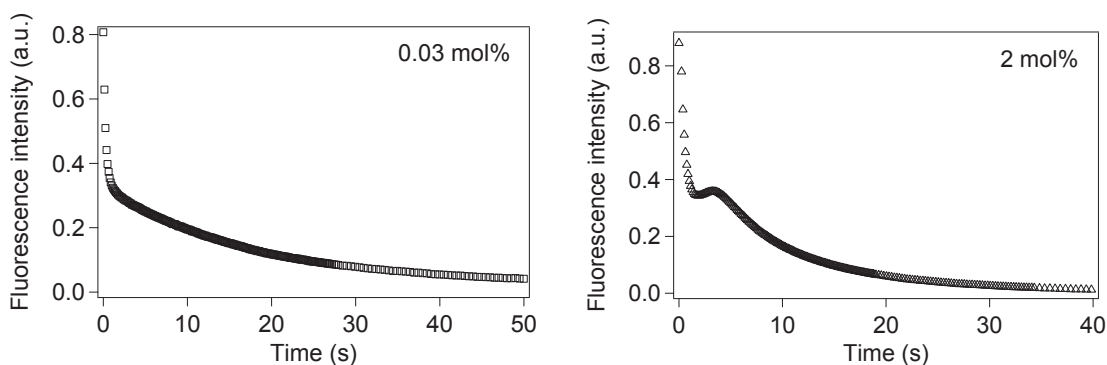


Figure 3.9: Fluorescence intensity decrease on Chlorin-12 containing GUVs. Left: Chlorin-12 concentration 0.03%. Right: Chlorin-12 concentration 2%, the curve shows a plateau.

To avoid the presence of any artifact here, we carefully checked that light was integrated over the whole vesicle (see 2.4.3).

Liposomes

We made POPC liposomes containing the same fraction of Chlorin-12 (1 mol%) and measured their absorption and emission spectra as a function of the irradiation time

(Fig. 3.10 and 3.11). A cuvette containing the liposome solution was placed into the spectrophotometer and continuously stirred. Here, irradiation is performed with a less powerful setup made of LEDs emitting at 405 nm. The measured power is 1.7 mW cm^{-2} .

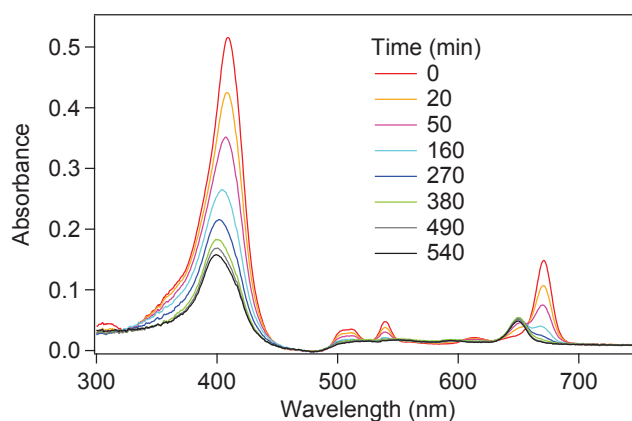


Figure 3.10: Absorption of POPC liposomes containing 1% Chlorin-12 for different irradiation time.

We observe in the absorption spectra that the peaks at 410 nm and 671 nm decrease whereas a new peak at 649 nm appears. The same effect was observed in the fluorescence spectra, where the peak at 676 nm decreases whereas a new peak at 653 nm appears. It seems that the Chlorin-12 molecules are either chemically modified or aggregate under irradiation. To reject the second hypothesis, we prepared a new sample and irradiated it until both peaks were present. Then, temperature was raised up to 70°C for several minutes: no change in the spectra was observed after heating.

In the following we refer Chlorin-12 as A molecule and its modified form as B.

At the end of the experiment, all A molecules are converted to B molecules and these B molecules start to photobleach. For intermediate times (between 50 and 490 minutes), an isobestic point is observed.

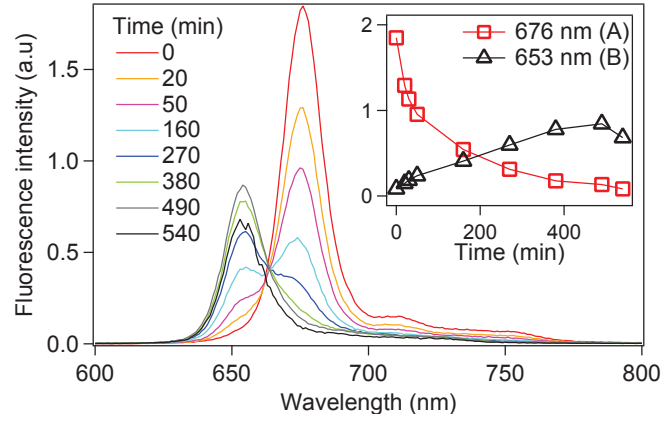


Figure 3.11: Fluorescence spectra evolution with irradiation time. The peak at 676 nm decreases while a peak at 653 nm appears. The inset shows evolution of the peaks at 676 and 653 nm. Excitation is performed in the main absorption band at 410 nm.

Comparison and kinetics

We propose a minimal model to explain the evolution of these spectra. At the beginning we have only Chlorin-12 molecules (A). Irradiation bleaches part of these molecules with a constant k_1 and modifies the other part into B molecules with a constant k_{on} . Then, these B molecules, which are still fluorescent bleach with a constant k_2 .

$$\begin{aligned}\frac{\partial c_A(t)}{\partial t} &= -(k_1 + k_{on})c_A(t), \\ \frac{\partial c_B(t)}{\partial t} &= -k_2c_B(t) + k_{on}c_A(t),\end{aligned}$$

with $c_A(0) = c_0$ and $c_B(0) = 0$.

The solutions are given by:

$$\begin{aligned}c_A(t) &= c_0 e^{-(k_1+k_{on})t}, \\ c_B(t) &= \frac{c_0 k_{on}}{k_2 - k_1 - k_{on}} (e^{-(k_1+k_{on})t} - e^{-k_2 t}).\end{aligned}\quad (3.3)$$

Thus, the fluorescence intensity is defined as:

$$I(t) = ac_A(t) + bc_B(t), \quad (3.4)$$

where a and b are the proportionality factors between fluorescence intensity and concentration for the species A and B respectively.

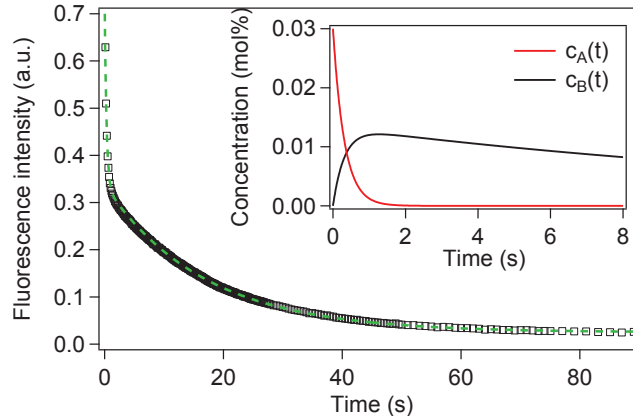


Figure 3.12: Fluorescence intensity decrease for a 0.03% Chlorin-12 containing POPC GUV (\square). The green dashed corresponds to the fit with Eq. 3.5. The inset shows the evolution of $c_A(t)$ (in red) and $c_B(t)$ (in black) as a function of time, obtained from the fit.

We can fit the intensity decrease in POPC GUVs with the formula:

$$I_{fitting} = cI(t) + d \quad (3.5)$$

where $I(t)$ is given by Eq 3.4. The constant c adjusts the I_0 because the fluorescence is in arbitrary units. The constant d adjusts the $I_{t \rightarrow \infty}$, which is very small, barely different from one curve to the other.

Our model explains well the fluorescence intensity decrease in a GUV with a low Chlorin-12 content, as displayed in Fig. 3.12. The values for the different parameters obtained from the fit are: $k_{on} = 1.4 \text{ s}^{-1}$, $k_1 = 1.8 \text{ s}^{-1}$, $k_2 = 0.06 \text{ s}^{-1}$ and $a = b = 1$. However, this model cannot explain the plateau observed at higher Chlorin-12 concentrations.

3.3.2 Re-absorption model

As there is an overlap between absorption and emission spectra for Chlorin-12 molecules (Fig. 3.13), light re-absorption between like molecules is found to occur. Fluorescence intensity should then be corrected accordingly.

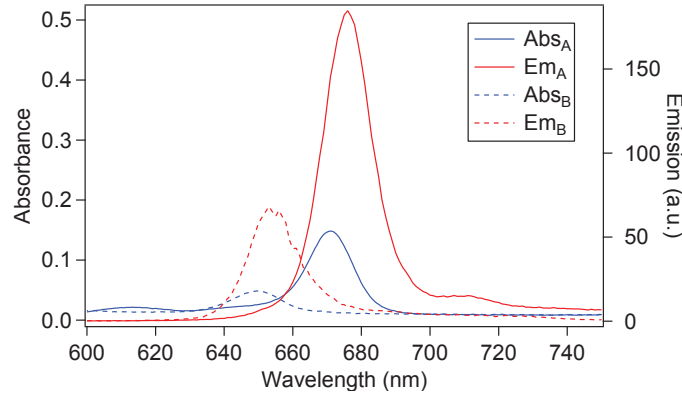


Figure 3.13: Absorption and emission spectra for A and B molecules in the region 600-750 nm. Spectra overlap can be easily noticed.

This overlap between emission and absorption can be calculated as follows. The couple AB for example, where B absorbs light emitted from A, is given by g_{BA} :

$$g_{BA} = \frac{\int_{\lambda_1}^{\lambda_2} Em_B(\lambda) Abs_A(\lambda) d\lambda}{\int_{\lambda_1}^{\lambda_2} Em_B(\lambda) d\lambda \int_{\lambda_1}^{\lambda_2} Abs_A(\lambda) d\lambda}.$$

The integration over the wavelength is done from $\lambda_1 = 600$ nm to $\lambda_2 = 800$ nm. We can get the different parameters g_{AB} , g_{BA} and g_{BB} as a function of g_{AA} (Table 3.1).

The value of the total fluorescence intensity emitted is then given by:

$$\begin{aligned} I(t) &= ac_A(t)(1 - (g_{AA}c_A(t) + g_{AB}c_B(t))) \\ &+ bc_B(t)(1 - (g_{BA}c_A(t) + g_{BB}c_B(t))) \end{aligned} \quad (3.6)$$

re-absorption factor	value (g_{AA} units)
g_{AA}	1
g_{BB}	1
g_{BA}	0.36
g_{AB}	0.06

Table 3.1: Values for the re-absorption factors in g_{AA} units.

where a and b are the proportionality factors between fluorescence intensity and concentration for the species A and B respectively, and g_{ii} ($i = A$ or B) is the so-called re-absorption factor.

We can again fit the intensity decrease in POPC GUVs containing different concentrations in Chlorin-12, with the equation 3.5, but using $I(t)$ which includes the re-absorption, given in Eq. 3.6 (see Fig. 3.14). The different parameters are k_1 , k_2 , k_{on} , g_{AA} , c_0 , a , b , c , d . By fitting the intensity decrease for the different Chlorin-12 concentrations, we could evaluate the parameters which are independent of the concentration change: k_1 , k_{on} , g_{AA} , a , b . By maintaining them constant, we can fit the curves by changing only c_0 , c , d and k_2 , as displayed in Table 3.2.

Parameter	Values from fit		
c_0	0.03	0.1	2
k_1 [s^{-1}]	1.8		
k_{on} [s^{-1}]	1.4		
g_{AA}	0.9		
a	1		
b	1		
k_2 [s^{-1}]	0.06	0.09	0.18
c	23.4	7.0	1.2
d	0.03	0.04	0.01

Table 3.2: Values for the different fit parameters for fluorescence intensity decrease for GUVs with different Chlorin-12 contents. The parameters k_1 , k_{on} , g_{AA} , a , b are maintained constant and c_0 is given by the molar concentration of Chlorin-12. The uncertainties on c , d and k_2 are smaller than 2%.

The order of magnitude of k_2 is conserved for the different concentrations. It

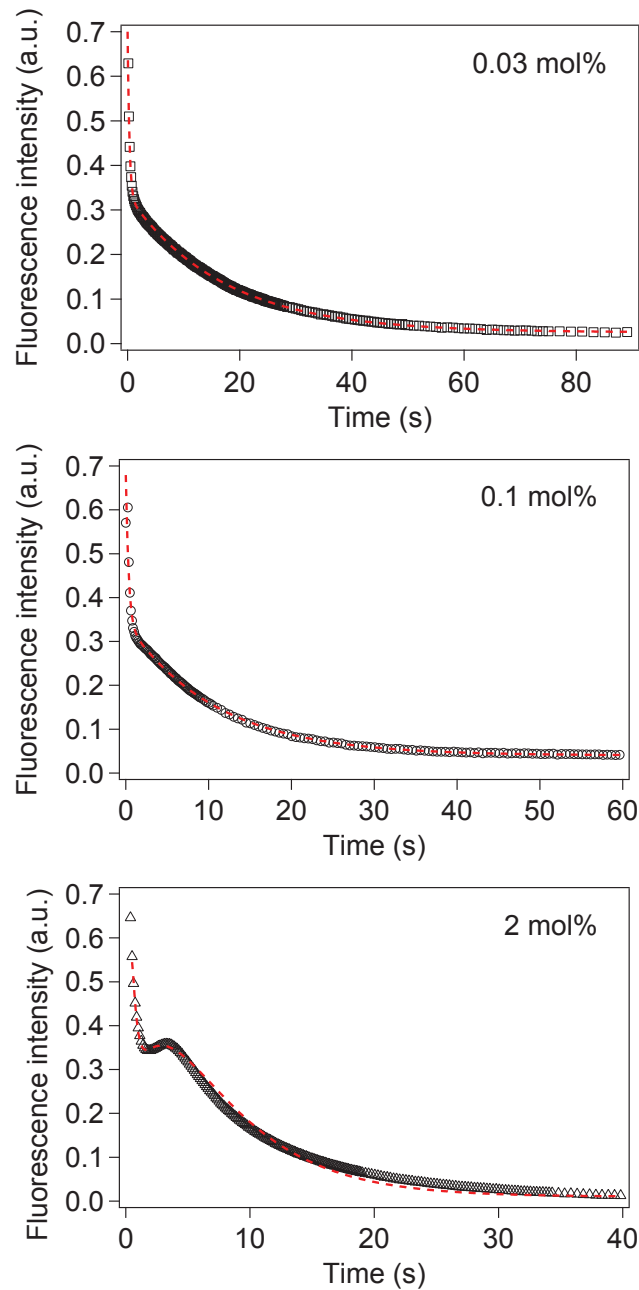


Figure 3.14: Fluorescence intensity decrease of POPC GUVs containing 0.03%, 0.1% and 2% of Chlorin-12. The dashed curves are the fit by formula given in Eq. 3.5.

increases slightly with Chlorin-12 content, that can be explained by a reaction between singlet oxygen and Chlorin-12, leading to an increased photobleaching. This simple model describes well the concentration effect, in particular the growing of a plateau with the PS concentration.

3.3.3 Discussion

Fig. 3.15 shows the time evolution of the fluorescence of liposomes and a single GUV. Please note that for liposomes the integrated fluorescence over the full spectrum was taken, while in the GUV experiment all the photons with a wavelength above 519 nm are captured by the camera. The two experimental curves superimpose nicely if the appropriate time scaling is applied.

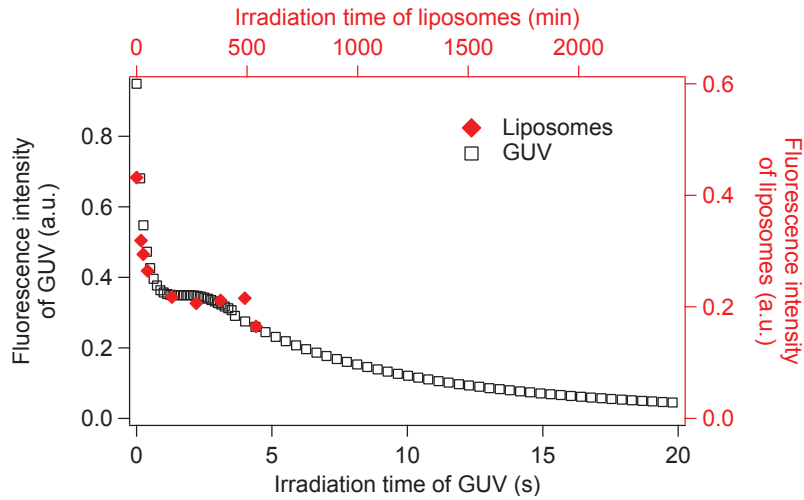


Figure 3.15: Fluorescence intensity decay as a function of irradiation time for POPC vesicles containing 1% of Chlorin-12: for a single GUV (\square) and for liposomes (\blacklozenge)

Indeed, the timescales are very different, due to a large difference in the irradiation powers. Knowing the irradiation power of the two setups: 1.7 mW cm^{-2} for liposomes irradiation and 2.7 W cm^{-2} for this particular GUV, we can compare:

$$\frac{P_{GUV}}{P_{liposomes}} \simeq \frac{2700}{1.7} \simeq 1600.$$

The times ($t^{A \rightarrow B}$) at which all A molecules disappeared were measured simply as corresponding to the extinction of the A peak. The ratio of these times in the two latter experiments gives:

$$\frac{t_{liposomes}^{A \rightarrow B}}{t_{GUV}^{A \rightarrow B}} \simeq \frac{490 \times 60}{5} \simeq 6000.$$

Even if the two ratios above are not identical, one can notice that they are of the same order of magnitude. The power of the LED setup is probably slightly overestimated as reflections at the water surface have not been taken into account.

According to this striking result, it appears that the size of the vesicles and the irradiation power do not change the intensity decrease behavior. Furthermore collective effects, that are only present in liposomes, can not explain the observed fluorescence time evolution. On the contrary, short length interaction (Energy transfer) would fit for both observations (Fig. 3.16). Indeed, in Förster resonant energy transfer, dipole/dipole interactions decay with the sixth power of the intermolecular distance and are not possible above a distance of 10 nm.

We can calculate the Förster radius from the spectral overlap by making several assumptions on the parameters required in the formula given in part 1.1.3, so that:

$$R_0 \simeq 0.2 \left(\kappa^2 \Phi_D n^{-4} \int_{\lambda_1}^{\lambda_2} I_D(\lambda) \epsilon_A(\lambda) \lambda^4 d\lambda \right)^{1/6}, \quad (3.7)$$

where the orientational factor for dipoles κ^2 is taken for randomly oriented molecules: $\kappa^2 = 2/3$, the fluorescence quantum yield of the donor is estimated around 0.2 following [17], the refractive index of the medium $n = 1.4$, the normalized fluorescence spectra and the molar extinction coefficient are taken from emission and absorption spectra and the integration is done from $\lambda_1 = 600$ nm to $\lambda_2 = 800$ nm.

We obtain $R_0 \sim 35$ Å, which is in the range where Förster energy transfer can occur.

The re-absorption model used above does not take into account an intermolecular distance threshold where transfer could occur or not. However, at low concentration of Chlorin-12 (0.03%), the concentrations of c_A and c_B are so small, that the second order terms $c_i c_j$ ($i, j = A$ or B) almost do not contribute to the intensity.

Energy transfer between like molecules is called energy migration and should not result in a change in fluorescence intensity and lifetime. To confirm or infirm these hypothesis, experience on fluorescence anisotropy should be performed as a function of Chlorin-12 concentration.

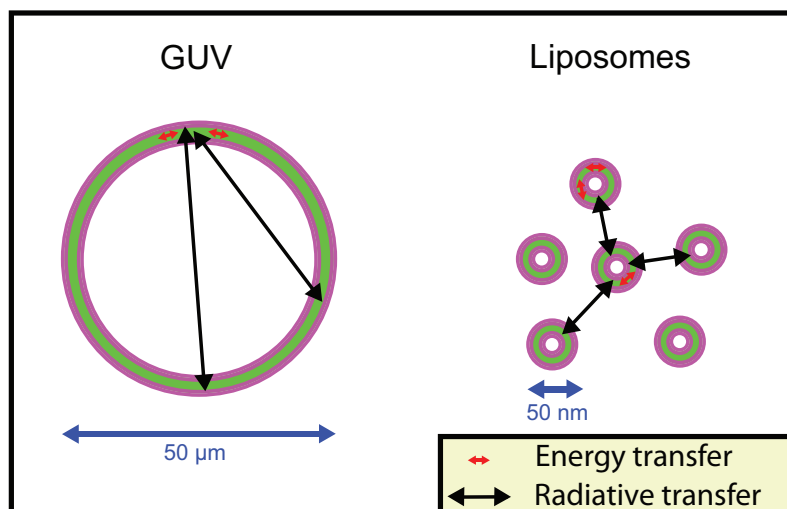


Figure 3.16: Scheme of the different possible interactions between Chlorin-12 molecules. Energy transfer occurs only on short distance between molecules ($\sim 1\text{-}10\ \text{nm}$), whereas light re-absorption can occur over much larger distances.

3.3.4 Singlet oxygen quantum yield

As the Chlorin-12 (A) molecules bleach and change to B molecules, we might wonder how the singlet oxygen production is affected. We measure the singlet oxygen production as a function of the absorption at $410\ \text{nm}$, for different irradiation times (Fig. 3.17). We can note a direct proportionality between singlet oxygen production and light absorption and this proves that the quantum yield of singlet oxygen production for B molecules is the same then for A molecules.

This result will be very important in the rest of the study, especially for a further quantification of singlet oxygen efficiency.

3.4 Conclusions

We designed a new original photosensitizer able to anchor in phospholipid membranes. The special features of this molecule allow high concentrations incorporation without any aggregation of the Chlorin-12.

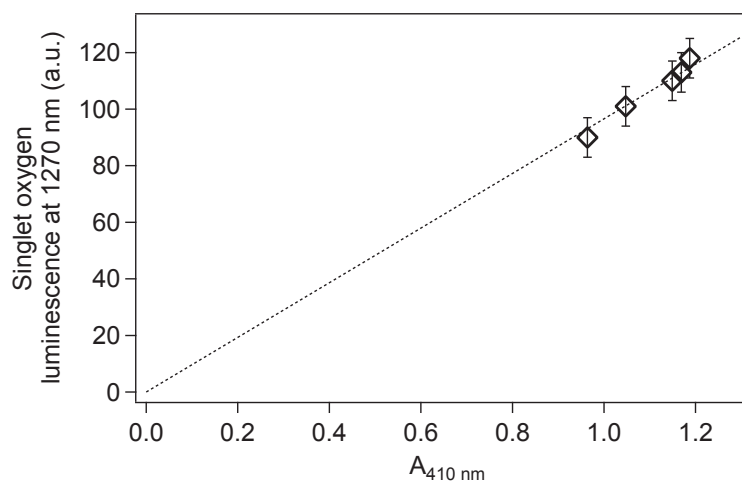


Figure 3.17: Singlet oxygen luminescence as a function of absorption at 410 nm.

Its photobleaching behavior is nevertheless complex, and it seems that a chemical modification happens under light irradiation. We analyzed this modification by doing absorption and emission spectra, but we are not able yet to establish its chemical structure. The accessible characteristics that we were able to investigate confirmed that its main light absorption and its fluorescence emission are slightly shifted to higher energies. However, the fluorescence and singlet oxygen quantum yields appear to stay constant upon this modification.

Further scrutiny of the structure of the so-called B molecule is clearly required, a task currently undertaken by our collaborators by NMR.

Chapter 4

Quantifying photo-oxidation in lipid bilayers

In this chapter, we study DOPC and POPC giant vesicles decorated by Chlorin-12. By combining a quantitative fluorescence analysis of the photosensitizing process with a micropipette control of the vesicle area increase, we show that full peroxidation of the lipids can be achieved, allowing thus to precisely measure the associated molecular and mechanical changes.

4.1 Hydroperoxidation of Giant Unilamellar Vesicles

We irradiate under an optical microscope, at 414 nm, Giant Unilamellar Vesicles (GUVs) of DOPC, a phospholipid with two mono-unsaturated carbon chains, or POPC, a second phospholipid with one saturated and one mono-unsaturated tail. The giant vesicles are decorated with a small fraction (0.03 % mol to 2 % mol) of Chlorin-12. Under irradiation, the photosensitizer Chlorin-12 generates singlet oxygen species $^1\text{O}_2$ that react with the chain double bonds, leading to the formation of the hydroperoxide group -OOH [68]. Migration of this hydrophilic group to the bilayer-water interface results in a larger molecular area per amphiphile as depicted in Fig. 4.1. As a consequence, GUVs exposed to photo-induced hydroperoxidation display phenomena characteristic of membrane area increase [57] such as enhanced fluctuations (see Fig. 4.2) followed by bud and tube formation (see Fig. 4.3).

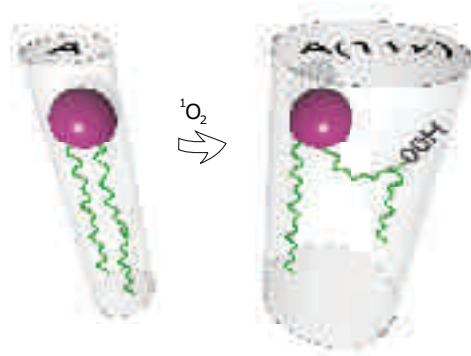


Figure 4.1: Schematics of the hydroperoxidation of a lipid with one unsaturated tail. Following a reaction with $^1\text{O}_2$, the double bond is converted into the organic hydroperoxide group $-\text{OOH}$, its migration to the bilayer surface leading to a relative increase ϵ of the molecular area of the converted lipid.

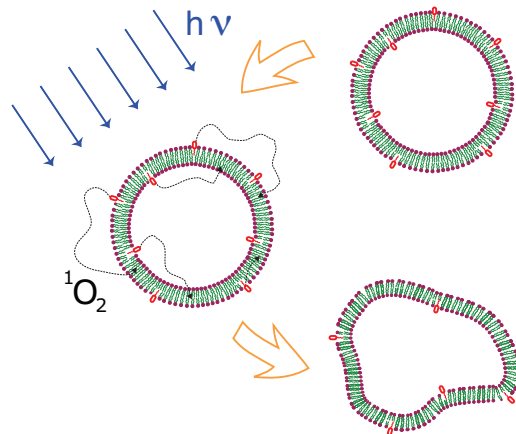


Figure 4.2: Irradiation of a vesicle decorated with the anchored photosensitizer Chlorin-12. The singlet oxygen species $^1\text{O}_2$ generated by the photosensitizers induce the conversion of the unsaturated lipids into their hydroperoxidized forms that have a larger molecular area. Under constant irradiation, as an increasing amount of lipids is converted, the total area of the GUV bilayer expands and the membrane displays large fluctuations followed by bud and tube formation.

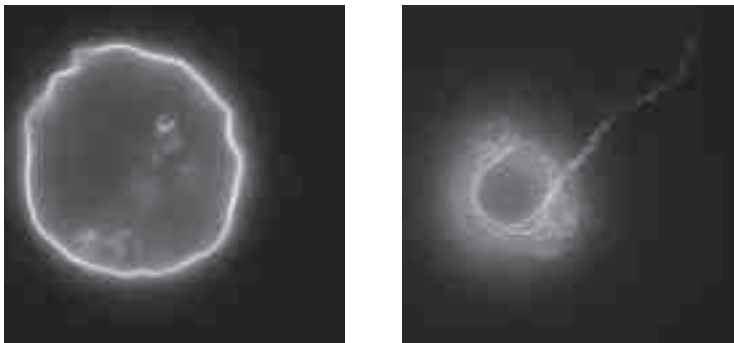


Figure 4.3: Different scenarios for irradiated DOPC giant vesicle containing 1% of Chlorin-12. Examples of fluctuations at the vesicle equator (on the left) and tubes production at the bottom of the vesicle (on the right).

4.2 Molecular area increase

4.2.1 Experimental setup

We measure concomitantly the increase of the vesicle bilayer area and the production of singlet oxygen. A micropipette setup coupled to an epi-fluorescence microscope allows to hold the giant vesicle with a small suction pressure, corresponding to a membrane tension of 0.7 mN m^{-1} , large enough to unfold the majority of membrane fluctuations without significantly stretching the bilayer, as explained in the Systems and Techniques section (2.3.4). The suction pressure is kept constant throughout the experiment. The analysis of the fluorescence microscopy images provides a measure for the total area of the membrane and for the amount of light emitted by the photosensitizers. Under irradiation at constant intensity a growing amount of membrane is sucked into the micropipette as depicted in Fig. 4.4.

4.2.2 Control Experiments

No delayed effects

We performed start-stop experiments on the Chlorin-12 decorated GUVs, hold by the micropipette, by irradiating the sample for about 5 seconds, and then observing the vesicles under the DIC observation mode for about 15 seconds (see Fig. 4.5). No delayed effects could be detected, after either stopping or restarting irradiation. Under our conditions, there is thus an instantaneous response of the vesicle area

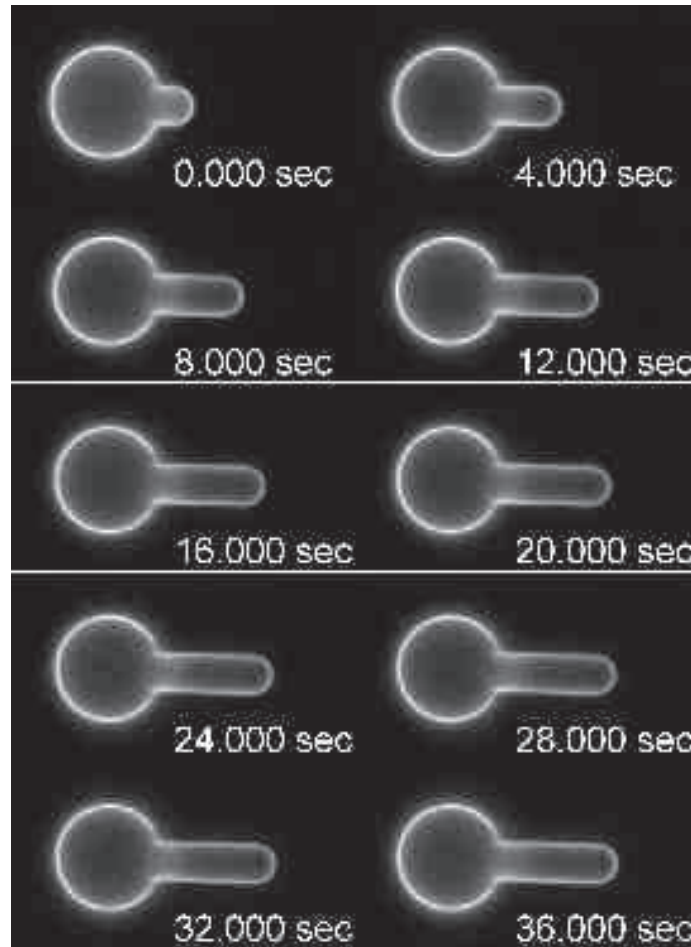


Figure 4.4: Snapshots of an irradiated GUV ($P = 1.3 \text{ W cm}^{-2}$) made from POPC + 1% of Chlorin-12. A constant tension of 0.7 mN m^{-1} is applied by the micropipette during the whole irradiation time. The excess area generated by oxidation is sucked by the micropipette allowing its precise measurement. The contrast of the image has been artificially increased to compensate for PS photobleaching.

expansion to the irradiation.

Unsaturated chains as targets

We also checked that the singlet oxygen reaction site is the unsaturation in the lipid chains. We formed GUVs made of DMPC (a lipid with two saturated chains of 14 carbons) and containing 1% of Chlorin-12 using the electroformation technique. The liquid/gel transition temperature of DMPC is 23°C . Thus, electroformation has been performed in an oven at 28°C . During the time needed to take the vesicles out

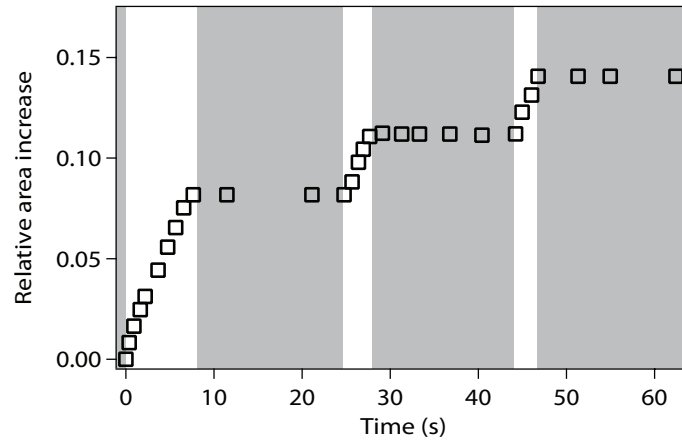


Figure 4.5: Relative area increase as a function of time, alternating irradiation (white region) and only observation (grey region) phases, for a DOPC vesicle containing 1% of Chlorin-12.

of the growing chamber and to observe them under microscope, phase transition to the gel state happened. Irradiation of the DMPC vesicles showed no effect. Indeed, the Chlorin-12 molecules followed the same bleaching behaviour, but we did not see any enhanced fluctuation or any tube formation. This is the reason why we did not use the micropipette here. A simple image analysis, using a 2π average radial profile was enough to extract the vesicle area evolution. Fig. 4.6 clearly shows no area increase. Phospholipid chain unsaturations are, in our experiments, the targets of $^1\text{O}_2$ molecules.

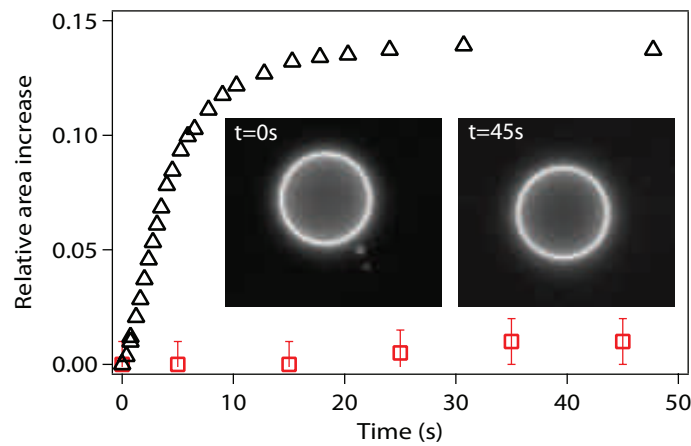


Figure 4.6: Evolution of the area increase in a DMPC vesicle with 1% of Chlorin-12 (□) under light irradiation and the corresponding fluorescence images, compared to the POPC vesicle showed before (Δ)

No membrane permeation

Our experiments clearly show that there is no membrane permeation taking place during the photooxidation. First, our oxidation experiments of GUVs submitted to a micropipette suction never showed any membrane rupture contrary to what has been observed in [16], corresponding to pore formation. Secondly, observation of GUVs under phase-contrast microscopy do not show any variation of the internal/external contrast, i.e. the sucrose/glucose asymmetry is conserved during photooxidation (images not shown).

4.2.3 Full lipid conversion

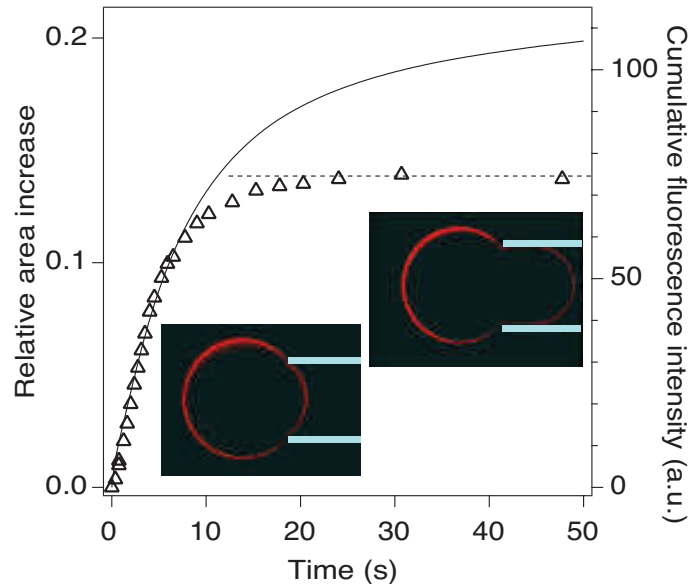


Figure 4.7: Relative area increase (left Y-axis) as a function of time for an irradiated ($P = 2.7 \text{ W cm}^{-2}$, here) POPC vesicle containing 2 % mol of the anchored photosensitizer Chlorin-12 (Δ). The relative area expansion was measured in a micropipette suction setup, as shown in the snapshot insets, at a constant membrane tension of 0.7 mN m^{-1} . The full curve (right Y-axis) shows in arbitrary units the cumulative light intensity emitted by the irradiated photosensitizers. Under these conditions, the relative area increases up to a saturation value displayed by the dotted line, where all the lipids have been converted to their hydroperoxide form. Error bars are smaller than the symbols size.

Experiments described here were done with high molar fractions of Chlorin-12, i.e. above 0.1%. A typical experiment is displayed in Fig. 4.7. After an initial

increase, the relative area expansion reaches a plateau. The full line in the figure displays the cumulated light intensity emitted by the photosensitizers, in arbitrary units. The cumulated intensity increases sub-linearly with time, due to probe bleaching, but a significant fraction of the probes has not yet been bleached when the area expansion curve reaches its plateau, suggesting that under these conditions all lipids have been converted into their hydroperoxide form. This hypothesis is further confirmed by experiments on the mechanical properties of hydroperoxidized membranes.

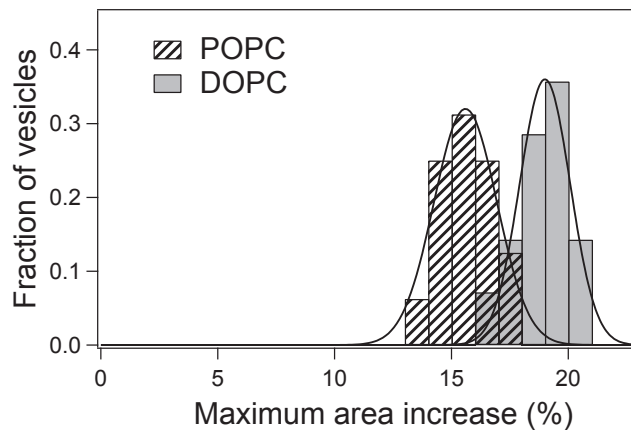


Figure 4.8: Histograms representing the distribution of values for the relative increase in molecular area for POPC and DOPC lipids in GUV bilayers. Plateau values were extracted from full hydroperoxidation experiments performed on 14 vesicles of DOPC and 16 of POPC. The curves represent Gaussian fits. The average values are 15.6% for POPC and 19.1% for DOPC.

We can define the fraction of oxidized lipids as follows:

$$x_{ox} = \frac{\text{relative increase}}{\text{saturation value}}.$$

For a fully peroxidized membrane, the fraction of oxidized lipids x_{ox} is then equal to 1.

Fig. 4.8 displays values for relative molecular area increase extracted from experiments performed under full conversion conditions. Histograms were built by analyzing 14 vesicles of DOPC and 16 of POPC. Values were also corrected by accounting for changes in the membrane stretching modulus as explained in 2.3.4.

4.2.4 Discussion

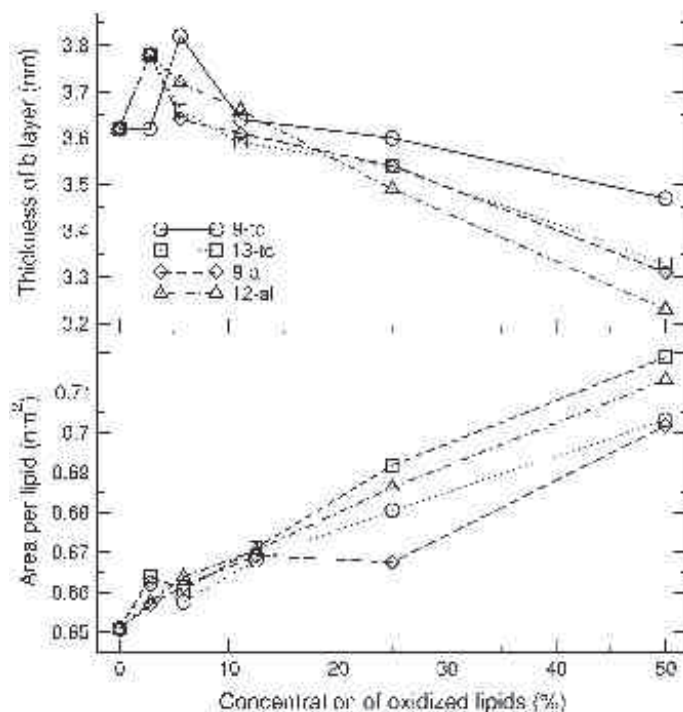


Figure 4.9: Values of membrane thickness decrease and lipid area increase as a function of the concentration of oxidized lipids in the membrane from simulations [56].

The formation of the -OOH group at positions 9 or 10 along the carbon chain [112] induces a clear change in the average molecular area of the lipid in the bilayer. Wong-ekkabut et al. [56] studied by molecular simulations the bilayer structure of oxidized PLPC lipids. PLPC has one unsaturated chain of 16 carbons and one chain of 18 carbons with two double bonds at positions 9 and 11. The simulations consider chains with hydrophilic hydroperoxide groups either at positions 9 or 13; they show that the -OOH moiety has a clear tendency to move towards the lipid-water interface leading to an increase of the average lipid area from 0.65 to 0.70 nm² in membranes carrying 50% of hydroperoxidized lipids (Fig. 4.9), corresponding to a relative increase of the molecular area per lipid of 16%. Our observed changes in the average molecular area of hydroperoxidized POPC depicted in the histogram of Fig. 4.8 are thus in very good agreement with those of the simulations, consistent with the similarities of the POPC and PLPC lipid structures. Strikingly, the relative area increase for bilayers assembled from DOPC, close to 19%, is only slightly larger than that of POPC, despite the presence of one unsaturated bond in both carbon chains of the lipid. This suggests that a fully hydroperoxidized DOPC bilayer has on average as many hydroperoxide groups in the vicinity of the bilayer-water interface

as the fully hydroperoxidized POPC bilayer.

4.3 Chlorin-12 concentration and irradiation power dependence

We repeated our irradiation experiments under tension for various values of the Chlorin-12 concentration and the irradiation power:

- Concentration range (mol%) [0.01%; 0.03%; 0.1%; 1%; 2%];
- Irradiation power [1/2; 1/4; 1/8; 1/16; 1/32] ($\times 10.8 \text{ W cm}^{-2}$).

4.3.1 Chlorin-12 concentration dependence

We measure the speed of area increase, from a linear fit of the relative area increase at short times (Fig. 4.10 Inset). The speed of area increase can then be plotted as a function of Chlorin-12 concentration. For low concentrations, between 0.01 and 0.1 %, its evolution is linear. For concentrations larger than 0.1 % a saturation is observed, which is attributed to self-quenching between Chlorin-12 molecules.

4.3.2 Irradiation power dependence and singlet oxygen depletion

Oxygen depletion is an important issue in clinical PDT, as hypoxia lowers considerably treatment efficiency. To check if in our experiments oxygen depletion plays a role, we decided to investigate, for vesicles containing high concentrations of Chlorin-12, how the speed of area increase depends on the irradiation power. Fig. 4.11 shows the proportionality between the speed of area increase and the irradiation power, even at high power, demonstrating that no oxygen depletion effects are present in our experiments.

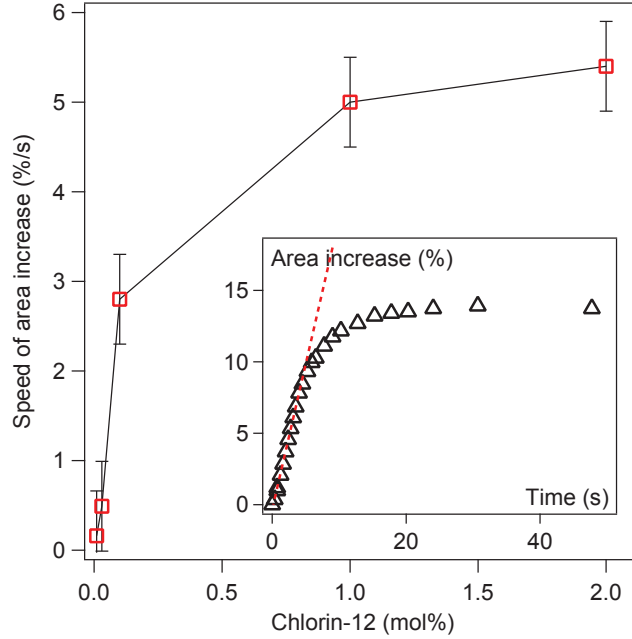


Figure 4.10: Speed of area increase as a function of Chlorin-12 concentration (\square). The inset shows a typical area increase curve as a function of time. The slope at short times (dashed curve) defines the speed of area increase.

The concentration of $^1\text{O}_2$ near the plane of the anchored sensitizers can be computed by solving the reaction-diffusion equation for the distribution of $^1\text{O}_2$ species:

$$\frac{\partial C_{SO}}{\partial t} = D \frac{\partial^2 C_{SO}}{\partial z^2} - \frac{C_{SO}}{\tau} + Q\Sigma\delta(z-b) \quad (4.1)$$

where C_{SO} is the singlet oxygen concentration profile, D the diffusion coefficient, z the distance away from the membrane, τ the $^1\text{O}_2$ lifetime, Q the rate of $^1\text{O}_2$ generation per sensitizer molecule and Σ the number of sensitizers per unit area. b is the distance between the $^1\text{O}_2$ generation plane and the membrane surface, of order of a fraction of nanometer. Eq. 4.1 supposes that singlet oxygen reactions with the unsaturated bonds only marginally perturb the distribution, a full description would require a sink term located at the average (negative) height of the double bond plane. The stationary solution of Eq. 4.1 reads:

$$C_{SO}(z) = \frac{Q\tau\Sigma}{2\ell_D} \exp\left\{-\frac{z}{\ell_D}\right\} \quad (4.2)$$

where $\ell_D = \sqrt{D\tau}$ is the diffusion length of $^1\text{O}_2$.

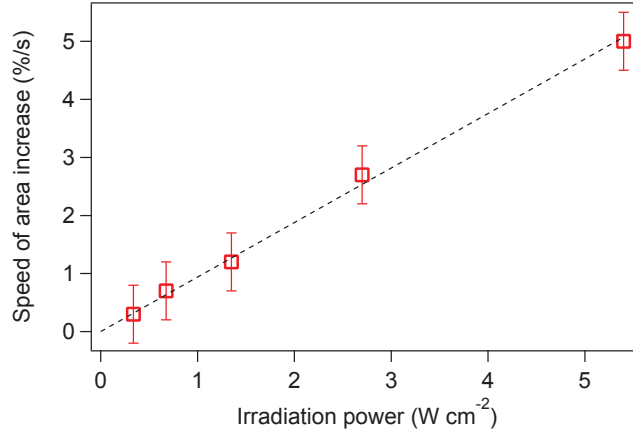


Figure 4.11: Speed of area increase as a function of irradiation power, for POPC vesicles containing 1% of Chlorin-12. The dashed curve represents a linear fit.

Close to the generating wall there is thus a concentration of singlet oxygen given by $C_{SO}(z=0) = 0.5Q\tau\Sigma\ell_D^{-1}$. Under the strongest irradiation conditions that we used ($P = 5.4 \text{ W cm}^{-2}$) and for the highest Chlorin-12 molar fraction of 2 %, where $Q = 1480 \text{ s}^{-1}$, $\ell_D = 100 \text{ nm}$, $\tau = 4 \mu\text{s}$, $\Sigma = 3.1 \times 10^{-2} \text{ nm}^{-2}$, we have $C_{SO}(z=0) = 1.6 \mu\text{M}$. In principle the planar localization of the sensitizers can lead to oxygen depletion if the sensitizer surface density Σ is too large. A higher bound value for Σ_{\max} can be estimated based on the comparison between the concentration of singlet oxygen at the surface $C_{SO}(z=0)$ and the concentration of molecular oxygen in solution C_{O_2} , giving a maximum number of sensitizers per unit surface $\Sigma_{\max} = 2C_{O_2}\ell_DQ^{-1}\tau^{-1}$. For densities larger than Σ_{\max} , oxygen depletion effects become important. Equivalently we can define the maximum sensitizer fraction $f_{\max} = \Sigma_{\max}S_0$ where S_0 is the area of one lipid molecule. Under our conditions where $S_0 = 0.65 \text{ nm}^2$, and $C_{O_2} = 250 \mu\text{M}$, we get $\Sigma_{\max} = 4.6 \text{ nm}^{-2}$ and $f_{\max} \sim 3$. In our case, where $f \sim 2 \times 10^{-2} \ll 3$, $^1\text{O}_2$ generation should thus not be limited by oxygen depletion effects.

4.4 Efficiency of the hydroperoxidation reaction

Each singlet oxygen molecule generated by a given sensitizer starts a diffusion path in the solution, in the immediate vicinity of the lipid bilayer, say at a vertical distance $b \sim 2 \text{ nm}$ from the average plane of the unsaturated bonds where an oxidation reaction can take place. A simple estimate based on the diffusion coefficient and decay time of singlet oxygens predicts that a fraction $1 - b/\ell_D \sim 98\%$ of generated $^1\text{O}_2$ species visits at least once the potential reaction sites, only a marginal fraction

escapes directly into solution where it decays. In practice, one can thus measure the reaction efficiency by comparing the number of singlet oxygens available per lipid and the number of double bonds converted into an hydroperoxide form.

4.4.1 Efficiency per unsaturated bond: a well defined binary process

Given the known irradiation power, sensitizer cross-section for light absorption and quantum yield for $^1\text{O}_2$ production, our experiments allow to quantitatively measure the number of singlet oxygen species generated by the anchored Chlorin-12 probes, provided that one uses low enough molar fractions of photosensitizers to preclude self-quenching. Under these conditions, prevailing in our case for photosensitizer molar fractions smaller than 0.1 % mol of Chlorin-12, the emitted fluorescence intensity and the amount of generated $^1\text{O}_2$ species is proportional to probe density (see part 2.4.3). Each Chlorin-12 molecule generates then an average of 740 $^1\text{O}_2$ molecules per second, under experimental conditions ($P = 2.7 \text{ W cm}^{-2}$) of Fig. 4.12.

Fig. 4.12 shows typical results for a POPC vesicle with 0.03 % mol of Chlorin-12. The squares in the figure correspond to the fraction of oxidized lipids obtained by dividing the measured values of relative area expansion by the average values of the corresponding plateaus measured above. Here, only about 25 % of lipid is oxidized before all probes are bleached. The full line in the figure shows the cumulative number of singlet oxygen species per lipid generated in a time t in this experiment. The inset of Fig. 4.12 demonstrates the striking proportionality between singlet oxygen production and area increase, allowing to extract, from the slope of the curve, the efficiency η of the reaction, as the fraction of generated $^1\text{O}_2$ species that oxidize one unsaturated bond. Efficiency values obtained from an average over three different experiments give $\eta_{\text{POPC}} \simeq 0.21 \pm 0.03$. Similar measurements performed on giant vesicles made from DOPC lipids provide comparable values $\eta_{\text{DOPC}} \simeq 0.19 \pm 0.01$. In this sensitizing geometry, roughly one out of five singlet oxygens generated by the anchored photosensitizers react with a double bond. We found similar values for the efficiency η in experiments with 0.1 % mol of probe where phenomena such as probe self-bleaching and oxygen depletion can be safely circumvented. Strikingly comparable efficiency values are also obtained for the DOPC lipids, showing that the reaction between a $^1\text{O}_2$ and a double bond is a well-defined binary process that is virtually not perturbed by the the presence of other neighboring unreacted un-

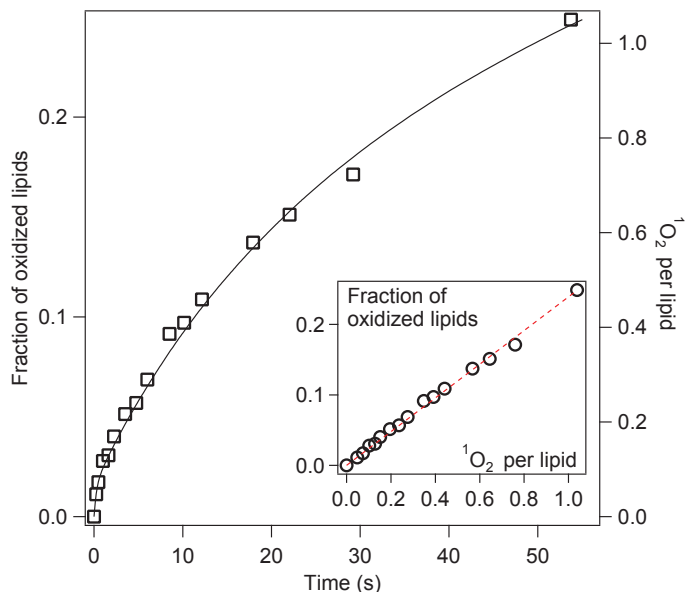


Figure 4.12: Fraction of hydroperoxidized lipids (\square , left Y-axis) as a function of time for an irradiated POPC vesicle containing 0.03 % mol of the anchored photosensitizer Chlorin-12. The full curve (right Y-axis) shows the cumulative number of $^1\text{O}_2$ per lipid produced in a time t . The efficiency of the reaction, measured by the number of $^1\text{O}_2$ species required to hydroperoxidize each POPC unsaturated bond can be read from the ratio of the scales in the left and right Y-axis or, alternatively, by the slope of the curve in the inset where the striking proportionality between oxygen production and lipid peroxidation is demonstrated. Error bars are smaller than the symbols size.

saturations or hydroperoxidized groups.

4.4.2 Comparison with bulk reaction constants

The efficiency values for the reactions between the double bonds and the $^1\text{O}_2$ species were obtained here from a two-dimensional distribution of photosensitizers. A comparison with the bulk reaction constants from the literature [113] can nevertheless be attempted by recognizing that the anchored photosensitizers generate an average concentration of $^1\text{O}_2$ species close to the membranes given by $C_{SO} = 0.5\Sigma Q\tau\ell_D^{-1}$, where Q is the number of $^1\text{O}_2$ generated per photosensitizer per unit time, Σ the number of photosensitizers per unit surface and τ the $^1\text{O}_2$ lifetime. The factor 0.5 relies on the assumption that $^1\text{O}_2$ molecules distribute evenly on both sides of

the probe plane. In a binary reaction between $^1\text{O}_2$ species at a concentration C_{SO} and double bonds of concentration C_{DB} one creates $k_{HP}C_{DB}C_{SO}$ hydroperoxide species per unit time $dC_{HP}/dt = k_{HP}C_{DB}C_{SO}$. Associating m , the initial slope of the curve in Fig. 4.12 with the value for the relative rate production of -OOH groups, $m = C_{DB}^{-1}dC_{HP}/dt|_{t=0}$ one has $k_{HP} = m \times C_{SO}^{-1}$. For the case of Fig. 4.12, $m = 0.036$, with $Q = 740 \text{ s}^{-1}$, $\ell_D = 100 \text{ nm}$, $\tau = 4 \text{ }\mu\text{s}$ and $\Sigma = 4.7 \times 10^{-4} \text{ nm}^{-2}$, we get a reaction constant $k_{HP} \simeq 3 \times 10^6 \text{ M}^{-1}\text{s}^{-1}$, in close agreement with literature values ($k_{HP} \sim 10^5\text{-}10^7 \text{ M}^{-1} \text{ s}^{-1}$) for the binary reaction between $^1\text{O}_2$ and mono and di-saturated carbon chains in methanol [113]. Thus, the planar distribution of the anchored sensitizers does not appear to perturb the microscopic mechanisms of the photo oxidation reaction. Instead, it dramatically reduces the total amount of photosensitizer required to fully oxidize the lipid double bonds. This can be better stressed by noticing that the singlet oxygen concentration C_{SO} achieved in this anchoring geometry would require a bulk concentration C_b of the same sensitizer of the order of $C_b = 0.5\Sigma\ell_D^{-1} \sim 25 \text{ }\mu\text{M}$!

4.4.3 Evolution at high Chlorin-12 contents

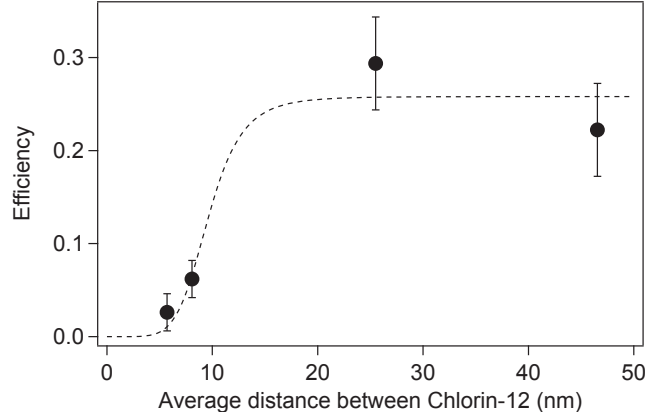


Figure 4.13: POPC hydroperoxidation efficiency as a function of the average distance between to Chlorin-12 molecules. The dashed line is a fit with Förster's formula (Eq. 4.3).

As shown previously, for a concentration of photosensitizer above 0.1%, some quenching effects occur. Here, we calculated the POPC hydroperoxidation efficiency for the whole range of photosensitizer concentrations tested. Error bars are bigger for low concentration experiments, because area increase measurements and fluorescence emission analysis were performed on different days with different vesicles.

The efficiency, as defined up to now, decreases dramatically at high Chlorin-12 concentrations, especially when the intermolecular distance between two Chlorin-12 gets lower than 10 nm. The reaction constant between singlet oxygen and double bonds does not have any reason to decrease, even at high concentrations. The best explanation here is that the correlation between fluorescence emission and singlet oxygen production is no longer valid. One can attempt a fit with Förster's formula:

$$\eta_{(R)} = \eta_{\infty} \left(1 - \frac{R_0^6}{R^6 + R_0^6}\right) \quad (4.3)$$

where R is the average distance between two Chlorin-12 molecules and R_0 the Förster radius.

The fit gives a Förster radius of 9 ± 1 nm, which is at the high limit for energy transfer. According to literature, the value should be between 1 and 10 nm in solution. It is much higher than the one that we estimated in part 3.3.3 from the spectral overlaps. The 2D geometry imposed by the membrane could probably change slightly the expression for energy transfer. Some models have been developed for acceptor molecules within the membrane and donors in the external solution [114] and both donors and acceptor within the membrane [115], but, to our knowledge, Förster energy transfer between like molecules anchored in a membrane have not been studied yet.

4.5 Modifications of the mechanical properties of the membrane

Achieving different degrees of lipid conversion from their native, non-oxidized form to their hydroperoxidized counterpart, while preserving membrane integrity, allows preparing GUVs that contain different fractions of oxidized phospholipids. Since the membrane impermeability with respect to sugars is also maintained for all fractions of hydroperoxide content, as observed from the preservation of the optical contrast, one can measure using the suction micropipette technique the stretching modulus of the membrane as a function of the conversion degree.

4.5.1 Preliminary observations

Fig. 4.14 shows the full area-tension curves for a non-oxidized DOPC ($x_{ox} = 0$) vesicle and an irradiated one characterized by $x_{ox} = 0.33$. Fitting the curves as explained in 2.3.4, allows to extract the bending modulus k_c and the stretching modulus K_A of the membrane. For the non-oxidized vesicle, we obtain $k_c = 16 \pm 1 k_B T$ and $K_A = 200 \pm 14 \text{ mN m}^{-1}$, in agreement with literature [106]. For the oxidized one, one measures $k_c = 10 \pm 1 k_B T$ and $K_A = 110 \pm 6 \text{ mN m}^{-1}$.

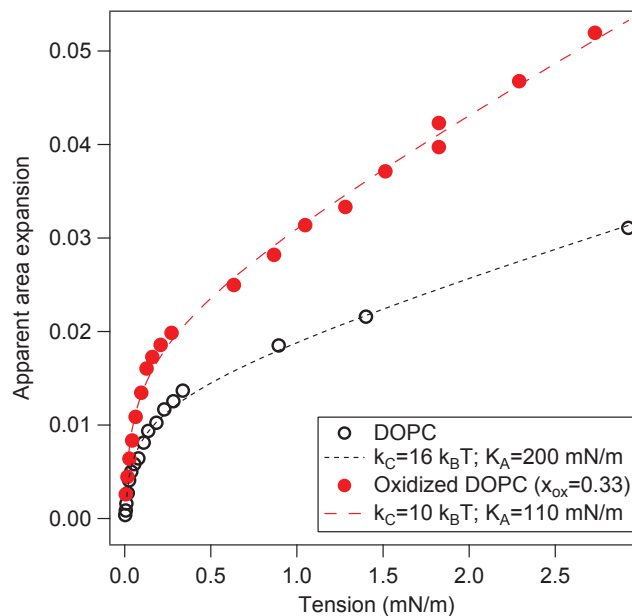


Figure 4.14: Apparent area expansion as a function of tension for a DOPC vesicle (\circ) and for a partially oxidized DOPC vesicle (\bullet) ($x_{ox} = 0.33$). The dashed curves are standard fits [105,116] to the data that allows extracting both the curvature and the stretching modulus.

Recently, Bouvrais et al. [117] showed that incorporation of fluorophores, even at low molar fractions, may change the membrane mechanical properties, especially the bending modulus. The effect of six commonly used probes (LAURDAN, TR-DPPE, Rh-DPPE, DiIC18, Bodipy-PC and NBD-PC) on the bending elasticity of a POPC bilayer was investigated prior to any irradiation. Small changes were observed compared to pure POPC bilayers when 2 mol% of Rh-DPPE, Bodipy-PC or NBD-PC are added in POPC membranes. Also, non reproducible bending elasticities were measured for Rh-DPPE containing GUVs, which was attributed to photo-induced peroxidation processes. In our case, area-tension curves do not display any difference

for POPC bilayers containing up to 2 mol% of Chlorin-12, as long as no irradiation occurs. If there are small changes in the mechanical properties due to the presence of the photosensitizer, these changes are within the error bars of our experiments.

Ayuyan et al. [15] found that some GUVs showed lipid rafts before irradiation for lipid compositions where no phase separation should occur. They attributed this effect to lipid peroxidation during electroformation with ITO slides. However, the amount of oxidized lipids was estimated to be less than 1 mol %. Our results obtained for the non-irradiated vesicles argue in the sense that GUV electroformation does not (or only slightly) lead to lipid peroxidation.

4.5.2 Stretching modulus evolution upon oxidation

We investigated the mechanical properties of irradiated GUVs by measuring their stretching modulus upon photo-induced peroxidation. Fig. 4.15 displays the results obtained for both DOPC and POPC giant vesicles. Bilayers of native lipids exhibit stretching moduli K_A of order of 200 mN m^{-1} , in close agreement with published data for the same two systems [106]. Fully oxidized bilayers of POPC have a stretching modulus of 50 mN m^{-1} while DOPC bilayers with 35% of hydroperoxidized lipids have a stretching modulus of 150 mN m^{-1} . These results are consistent with a linear variation of the modulus as a function of the conversion rate. The figure also shows stretching modulus measurements performed on Giant Vesicles electroformed from POPC-OOH, the hydroperoxidized form of POPC, that we have prepared independently, by methods described in the Appendix A.2.2. K_A values for 100% POPC-OOH vesicles are close to 50 mN m^{-1} , confirming that full conversion is reached under our irradiation conditions with 2 mol% of probe content. K_A values for a 50:50 mixture of POPC-OOH:POPC also support that the stretching modulus follows a linear variation with the fraction of POPC-OOH.

Membrane disruption, pore formation and increased membrane permeability have been reported in many of the experiments that have previously dealt with bilayer oxidation [11,16]. Our experiments show however that such membrane modifications should not be associated with lipid hydroperoxidation. Indeed, full conversion of the double bonds into their -OOH form does not disrupt the membrane nor induce an increased permeability with respect to sugar content in GUVs. Moreover, standard electroformation methods can be used to make GUVs of 100% POPC-OOH

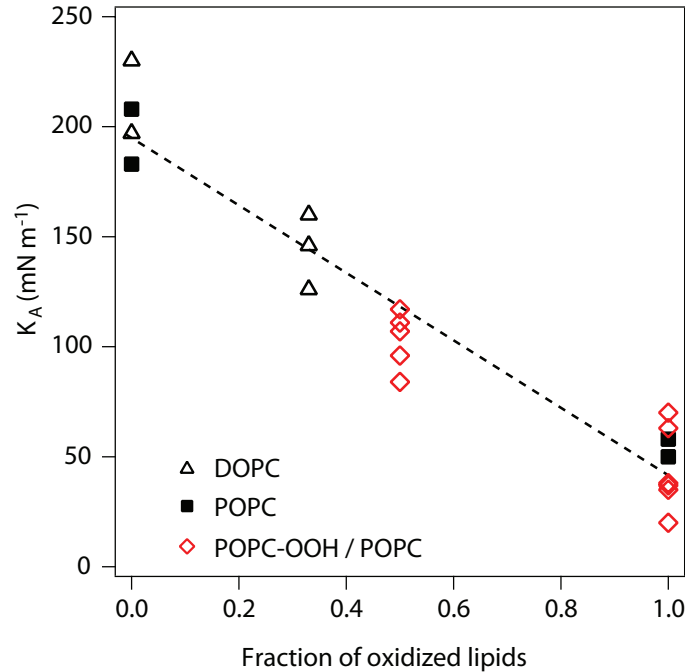


Figure 4.15: The value of the membrane stretching modulus K_A as a function of the fraction of oxidized lipids for DOPC (■), POPC (△) and POPC-OOH containing (◇) vesicles. The dashed straight line is a guide to the eyes.

lipids, with mechanical properties similar to those of membranes that have been oxidized in situ. In particular, bilayers made from 100% of hydroperoxidized POPC display a factor four decrease of their stretching modulus, from $K_A = 200 \text{ mN m}^{-1}$ down to $K_A = 50 \text{ mN m}^{-1}$, irrespective of the hydroperoxidation method.

4.5.3 Discussion

The decrease of membrane stretching modulus cannot be ascribed to a variation in membrane thickness only. Indeed, for a plate of a given Young modulus E , the stretching modulus is proportional to the membrane thickness h , $K_A \sim Eh$ [118]. At constant Young modulus, one would require an unlikely decrease of the membrane thickness by a factor four in order to explain the observations. Instead, numerical simulations [56] where a membrane thinning of 10% is observed for bilayers with 50% of hydroperoxidized lipid, show that the -OOH groups are statistically distributed along the membrane thickness, with a marked density at the lipid-water interface. This migration of the -OOH group to the bilayer interface and the as-

sociated structural changes translate into modified mechanical properties. Indeed, one heuristically describes the bilayer self-assembled structure as the result from a simple balance between the interfacial energy of the lipid-water interface, that tends to reduce the area per lipid and thus thicken the membrane, and the lipid-chain and lipid-head repulsion that tend to increase the area per lipid and thus reduce the membrane thickness [119]. Within this picture of bilayer assembly, the reduction of the stretching modulus implies that the assembling free-energy as a function of the area per molecule has a shallower minimum for POPC-OOH than for POPC lipids. These lower contributions to the free energy in the oxidized bilayer can have a double origin: not only is enrichment of the tail/water interface by the hydrophilic -OOH groups likely to lower its interfacial free energy, but a larger vertical bilayer compressibility is also expected to result from the reduction of vertically aligned carbon chains. This is further supported by the observed similarities between DOPC and POPC values measured for the relative area increase and for the stretching modulus reduction. Indeed, those similarities show, in agreement with numerical simulations [56], that not all the -OOH groups migrate to the interface but that the nature of their statistical distribution is an intrinsic property of the hydroperoxidized bilayer that results from a balance between the affinity of the -OOH for the lipid-water interface and the costs associated with changes in chain conformation.

4.6 Conclusion

Giant Unilamellar Vesicles, that can be directly imaged and manipulated under an optical microscope, have developed as valuable biomimetic tools to study the photophysical and photochemical factors controlling the uptake of photosensitizers in lipid membranes and the related modifications induced by $^1\text{O}_2$ oxidation [11, 16, 57]. Complementary to studies in small liposomes [120], results from GUVs provide direct information on the physical transformations associated with lipid peroxidation. In this chapter we have shown that relative changes in the lipid molecular area can be directly correlated with singlet oxygen generation, thus allowing an in situ measurement of the efficiency of the binary reaction between double bonds and $^1\text{O}_2$ species. The lipid changes result also in a reduction of the stretching elasticity of the bilayer that we have quantified. Our measurements, based on a new photosensitizer probe that anchors in the bilayer without aggregating, provide a coherent and precise scenario for lipid hydroperoxidation in lipid bilayers of both POPC and DOPC.

Single oxygens are generated in the close vicinity of the bilayer, from where they

start a random trajectory that penetrates the bilayer with a probability close to unit. One out of five $^1\text{O}_2$ molecules will react with a double bond before it decays, leading to the formation of a -OOH group at position 9 or 10 along the unsaturated chain. The hydrophilic character of the -OOH group increases its probability to seat at the lipid-water interface, and provides thus a driving force that changes the average chain conformation and the hydrophobic nature of the lipid-water interface. The resulting changes in chain conformation induce an increase of roughly 15 % of the lipid molecular area. The combined modifications of chain conformations and -OOH density at the lipid-water interface lead to a reduction by a factor four of the bilayer stretching modulus. In spite of the modifications of the lipid molecular structure, the self-assembled bilayer is not destroyed, it retains instead its integrity and its impermeability with respect to sucrose or to glucose.

Our experimental geometry for the evaluation of lipid peroxidation, based on Giant Unilamellar Vesicles decorated with anchored sensitizers is a flexible and quantitative tool that can address many of the open questions in this field. It is well adapted, for instance, to quantify the protecting role of antioxidants and to study the mechanisms by which the unsaturated bonds can be protected from a reaction with singlet oxygen. Most importantly, this experimental geometry can also deal with more complex and bio-relevant lipid bilayers made from lipid mixtures and proteins, a first step towards the understanding of the role of lipid oxidation in signaling cascades.

Chapter 5

Complementary studies

We present in this chapter two complementary studies dealing with membrane oxidation. Sodium azide is a common singlet oxygen quencher, often used in bulk systems, a proof that some effect, if reduced or suppressed by this molecule, is caused by $^1\text{O}_2$ moieties. However, using a $^1\text{O}_2$ quencher when the generating sources are close to the oxidation targets implies a different scenario that we describe in the first part of this chapter. The second part compares the behaviors of unsaturated lipids and their hydroperoxidized form in monolayers to that in bilayers. We will also discuss the instability of unsaturated lipids at the water-air interface.

5.1 Effect of a singlet oxygen quencher

Anti-oxidants are molecules able to avoid oxidation phenomena in living systems. They are advertised for their health beneficial and incorporate formulations. The family of anti-oxidants is very large. Some molecules (for example α -TOH) can give an electron to radical species, stopping the chain reaction in type I processes. Different types of $^1\text{O}_2$ quenchers can also be used, as unsaturated molecules, able to react with $^1\text{O}_2$ and competing then with living tissues or other molecules that de-activate $^1\text{O}_2$ by physical quenching.

5.1.1 Bulk quencher inefficient against surface generated $^1\text{O}_2$.

According to literature, sodium azide (NaN_3) is an efficient physical quencher that can react both with some photosensitizer triplet states or directly with $^1\text{O}_2$ [121]. However, in our work, by adding NaN_3 in our samples, we still observed GUV hydroperoxidation. Fig. 5.1 compares typical oxidation curves in presence and absence of NaN_3 . The relative area increases with the same speed and in the final state, the maximum area increases are identical (Fig. 5.2). Quenching effects, if any, are weak, below error bars.

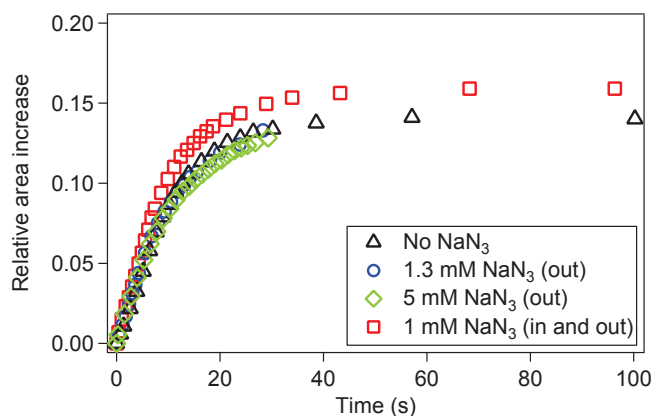


Figure 5.1: Relative area increase of GUVs made from POPC and 2 mol% of Chlorin-12, under irradiation. The curve behavior is not altered by adding NaN_3 in the glucose solution (out) or in both sucrose and glucose solutions (in and out).

In their previous work, Riske et al. [57] claimed that 1 mM of NaN_3 is completely preventing vesicle oxidation (see Fig. 5.3), but we clearly see a vesicle, even out of focus, that clearly shows enhanced fluctuations under irradiation. It could be that the main vesicle is relaxing excess area in tube formation, which is difficult to observe in phase-contrast.

These observations raise some questions about the mechanisms involved in $^1\text{O}_2$ quenching by NaN_3 . There are two possibilities to stop singlet oxygen reactions. The first possibility for the quencher is to react with the triplet state of the photosensitizer and thus decrease its lifetime. Another option is to react directly with the singlet oxygen.

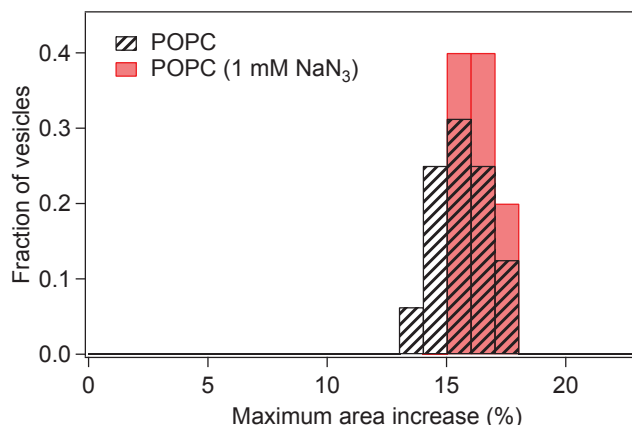


Figure 5.2: Histograms representing the distribution of the maximum area increase. With or without NaN_3 , the area saturates at the same values.

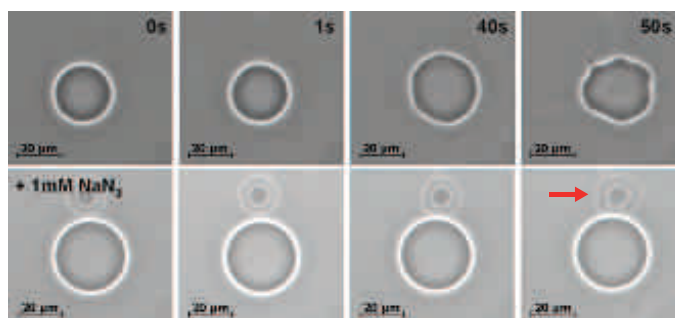


Figure 5.3: Effect of sodium azide (NaN_3) on GUVs made of POPC containing 5% of PE-porph [57]. The sequence shown on top was obtained in the absence of sodium azide, and clear morphological changes are observed as a result of irradiation. The sequence at the bottom was obtained in the presence of 1 mM NaN_3 , and almost no changes are detected, in the vesicle located in the foreground. However, the vesicle in the background shows enhanced fluctuations upon irradiation (our red arrow).

5.1.2 Triplet state lifetime

First, we measured the triplet state lifetime of Chlorin-12 diluted in ethanol, using Flash Photolysis (see part 3.1.1). Measurements could not be done in Chlorin-12 containing liposomes because of light scattering effects. By increasing the NaN_3 bulk concentration up to 10 mM, no change in Chlorin-12 triplet state is observed (Fig. 5.4). We can thus conclude that azide does not react directly with the triplet state of Chlorin-12.

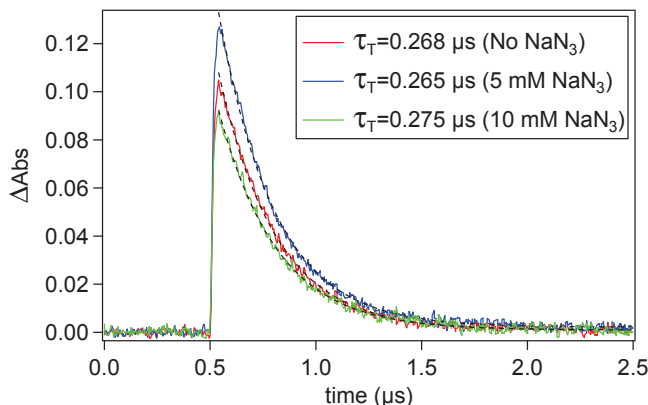


Figure 5.4: Evolution of the Chlorin-12 triplet state lifetime for different azide concentrations.

5.1.3 Singlet oxygen Lifetime

We then checked to which extent does NaN_3 directly affect the $^1\text{O}_2$ lifetime. We observed that azide changes $^1\text{O}_2$ lifetime in ethanol (Fig. 5.5). By fitting the exponential decrease of singlet oxygen luminescence, we get $\tau_{SO} = 16.5 \mu\text{s}$ without NaN_3 and $\tau_{SO} = 3.7 \mu\text{s}$ with 1 mM of NaN_3 . As defined by:

$$\tau_Q^{-1} - \tau^{-1} = K_Q[Q],$$

where τ is the singlet oxygen lifetime in absence of quencher, τ_Q is the singlet oxygen lifetime in presence of the quencher, $[Q]$ is the quencher concentration and K_Q is the experimental quenching rate constant, we can estimate $K_{Q=\text{azide}} = 2 \cdot 10^8 \text{ M}^{-1} \text{ s}^{-1}$. Note that at very short times ($t < 1 \mu\text{s}$) one can see the initial increase of $^1\text{O}_2$ signal, corresponding to the Chlorin-12 triplet state decay.

In liposomes (Fig. 5.6), the results display a larger noise. We were not able to record the singlet oxygen increase at low times, as in ethanol solutions. Each curve exhibits a very fast decrease ($t \ll 1 \mu\text{s}$) that we are not able to interpret and that might correspond to some experimental artifact [41, 42]. We extract the lifetimes at longer times: $\tau_{SO} = 19 \mu\text{s}$ without NaN_3 and $\tau_{SO} = 1.5 \mu\text{s}$ with 1 mM of NaN_3 , leading to $K_{\text{azide}} = 6 \cdot 10^8 \text{ M}^{-1} \text{ s}^{-1}$ for liposomes in D_2O , in agreement with literature [122, 123].

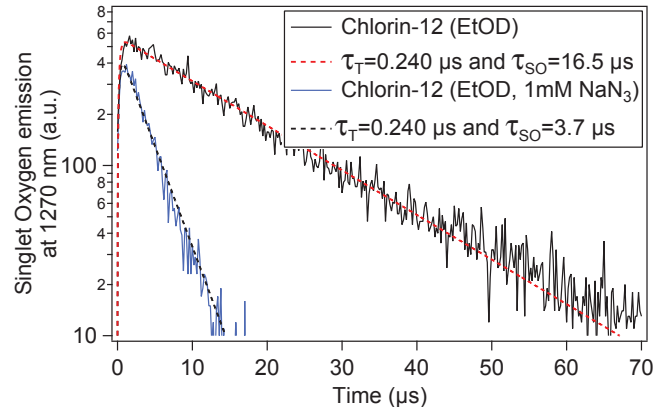


Figure 5.5: Singlet oxygen luminescence at 1270 nm as a function of time for Chlorin-12 molecules in ethanol, with and without azide.

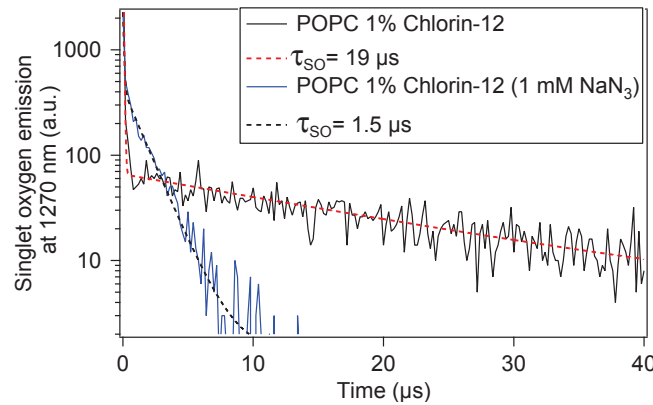


Figure 5.6: Singlet oxygen luminescence at 1270 nm as a function of time for POPC liposomes containing 1% Chlorin-12, with and without azide.

5.1.4 Simple model based on diffusion

The decrease of singlet oxygen lifetime in the presence of NaN_3 for liposomes containing Chlorin-12 is in apparent contradiction with the absence of any effect in GUVs. In order to understand this contradiction, we compute a simple model for the singlet oxygen concentration profiles in the vicinity of the membrane. We assume that the bilayer has a thickness $2e = 5$ nm and is flat, which is a good approximation if one compares typical GUV sizes (~ 50 μm) to the singlet oxygen diffusion length (~ 100 nm). As the bilayer is symmetric, we only consider half of the bilayer.

We assume that singlet oxygen is created at the water-bilayer interface, at a dis-

tance e from the bilayer center and it is consumed in the region of the C=C double bonds, at a distance $e/2$ from the bilayer center. The $^1\text{O}_2$ species also have a defined lifetime τ , depending on the solvent in which they evolve. Slightly changing the position of the generation and reaction planes does not significantly change our results.

We write the diffusion equation in the two media (Equations 5.1 and 5.2): from 0 to e corresponding to the monolayer and from e to $+\infty$ corresponding to the water outside the vesicle (figure 5.7):

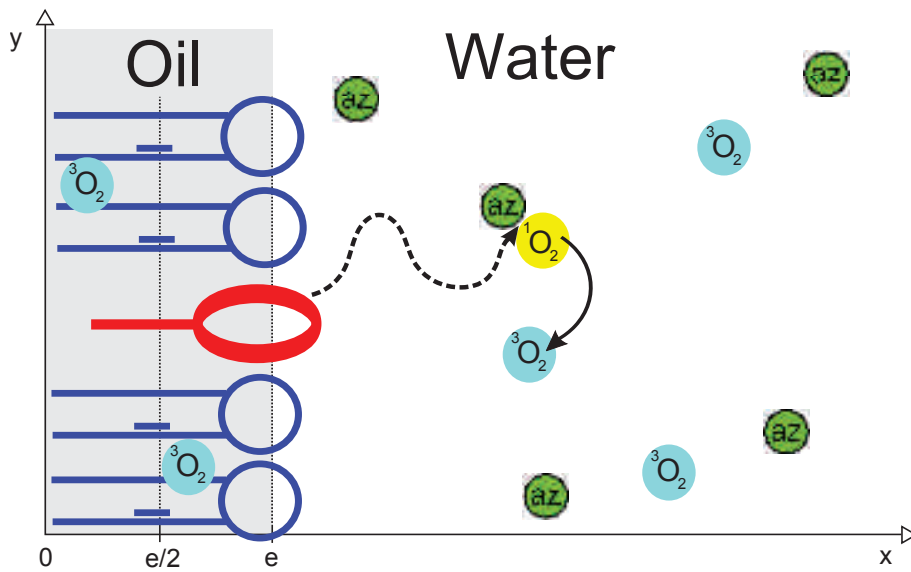


Figure 5.7: Representation of the system.

$$\frac{\partial c(x,t)}{\partial t} = D_w \nabla^2 c(x,t) - \frac{c(x,t)}{\tau_w} + q \delta(x-e) f(t), \quad (5.1)$$

$$\frac{\partial c(x,t)}{\partial t} = D_o \nabla^2 c(x,t) - \frac{c(x,t)}{\tau_o} - K_{uns} c_{uns} c(x,t) \delta(x-e/2), \quad (5.2)$$

where $c(x,t)$ is the singlet oxygen concentration, D_w and D_o are respectively the diffusion coefficient of singlet oxygen in water and in the membrane (oil), τ_w and τ_o are respectively the singlet oxygen lifetime in water and in oil, $q \times f(t)$ is the creation term, K_{uns} is the reaction constant of hydroperoxidation, and c_{uns} the concentration of unsaturations in the membrane. In a first approximation, we assume that c_{uns} is constant, and we define k as $k = K_{uns} \times c_{uns}$.

Coefficient	Value
e	2.5 nm
D_w	$2 \times 10^{-9} \text{ m}^2\text{s}^{-1}$ [34, 124]
D_o	$1 \times 10^{-9} \text{ m}^2\text{s}^{-1}$ [34, 124]
τ_w	4 μs [110]
τ_o	15 μs [125]

Table 5.1: Values of the different parameters used from the literature.

We can solve by Laplace Transform the system of equations (5.1) and (5.2), using the values taken from the literature for the different constants, coefficients and lifetimes (Table 5.1). NaN_3 is only present in the water and not in the membrane [28]. Its presence (at a concentration of 1 mM) decreases the lifetime of singlet oxygen in water by a factor 4, according to $K_{azide} = 6 \cdot 10^8 \text{ M}^{-1} \text{ s}^{-1}$, so that $\tau_w(1 \text{ mM } \text{NaN}_3) = 1 \mu\text{s}$. The lifetime in the membrane (τ_o) is not affected by NaN_3 .

The value of k is taken from the bulk efficiency in part 4.4.2. We have $k = k_{HP} \sigma_{uns} = K_{uns} c_{uns}$, with $k_{HP} = 3 \times 10^6 \text{ M}^{-1} \text{ s}^{-1}$ and $\sigma_{uns}^{-1} = 65 \text{ \AA}^2$. Thus, $k \simeq 1/130 \text{ m s}^{-1}$.

5.1.5 Singlet oxygen distribution under continuous irradiation

Using continuous irradiation, i.e. $f(t) = 1$, we can compute the singlet oxygen distribution next to the membrane. In order to simplify the model, we don't take into account neither the bleaching of the Chlorin-12 nor the fact that c_{uns} is not constant for longer times (because the number of non-oxidized lipids available decreases). For the stationary case, the singlet oxygen concentration distribution is calculated and displayed in Fig. 5.8.

Without azide, reaction of singlet oxygen with unsaturations decreases the singlet oxygen concentration. By comparing the case where no reaction occurs between $^1\text{O}_2$ and unsaturations ($k = 0$) and the case where one $^1\text{O}_2$ out of five reacts ($k = 1/130$), we notice that the concentration is divided almost by a factor two at $e/2$.

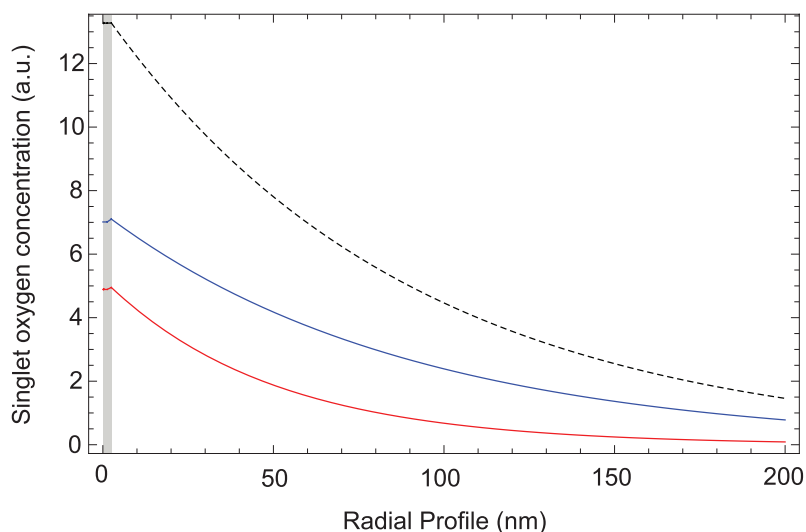


Figure 5.8: Singlet oxygen concentration (u.a.) as a function of the distance to the membrane for a continuous irradiation. Dashed curve: $k = 0$, without NaN_3 ; in blue: $k = 1/130$, without NaN_3 , in red: $k = 1/130$, with 1 mM of NaN_3 . The gray region represents half of the bilayer.

By comparing the profiles for $k = 1/130$ with and without NaN_3 , one can notice that the effect of NaN_3 is not as strong as expected, and in the membrane the singlet oxygen concentration is not even divided by a factor two. However, according to our experimental resolution, such a decrease of singlet oxygen generation should be easily detectable in micropipette experiments.

Experiments on GUVs with azide were always done at high Chlorin-12 molar fractions (2 mol%), chosen to maximize the peroxidation effects and therefore better observe the quencher efficiency. We have already shown in part 4.3.1 that for such high Chlorin-12 contents, a quenching effect is lowering the oxidation effect upon irradiation. If NaN_3 is acting according to our model, it will decrease by less than a factor 2 the singlet oxygen concentration, which is not enough to leave the saturation regime (Fig. 5.9). The speed of area increase will then be comparable to the one at 1 mol% of Chlorin-12, which is almost the same than at 2 mol% due to the saturation effect. It will thus remain unchanged and within the experimental error bars.

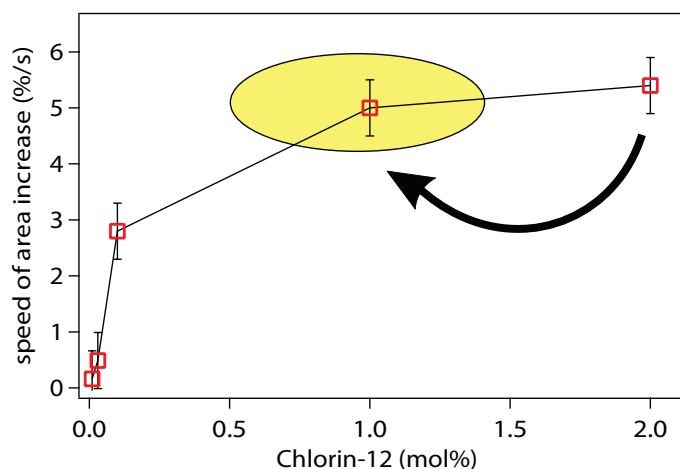


Figure 5.9: Speed of area increase as a function of the Chlorin-12 concentration in the vesicle. Above 0.1 mol%, the value saturates due to a quenching effect. A 2 mol% containing vesicle under irradiation will then behave like a less concentrated one, with only a slightly difference in the speed of area increase, not detectable due to the error of the measurement.

5.1.6 Conclusion

In this part, we studied the effect of a well known quencher, NaN_3 , on our system. It appears that NaN_3 has no effect on Chlorin-12 triplet state, even at high quencher concentrations. However, NaN_3 clearly decreases $^1\text{O}_2$ lifetime, with a reaction constant in good agreement with the literature.

The proximity between the planes of singlet oxygen generation and reaction sites explains well why azide in the bulk solution is less efficient to prevent lipid oxidation than in systems where the PS is distributed in the bulk as well. However, it can not completely explain the total inefficiency of the quencher on GUVs composed from POPC and 2% of Chlorin-12. The full explanation lies on the quenching effect at high concentrations of Chlorin-12, completely hiding the protective effect of azide. Complementary experiments should be done, using lower concentrations in Chlorin-12, in order to be out of the saturation regime and to quantify the protective effect of NaN_3 upon lipid peroxidation.

5.2 A monolayer study

Phospholipid bilayers are found in cells and cell organelles but monolayers are seldom encountered in nature. However, they play an important role in the lung. Indeed, the inner sides of the lung alveoli are recovered from a lipid monolayer, in order to decrease the surface tension and thus the Laplace pressure, and to avoid lung collapse.

We investigated the properties of oxidized monolayers and compared them with bilayers. This study raised some questions about monolayers stability. Indeed, by comparing different POPC isotherm from the literature, we were never able to find two identical ones. Therefore, we started a preliminary work on monolayer stability and we will discuss the effects of oxidative damage on POPC and DOPC monolayers induced by species present in the air.

5.2.1 Isotherms of POPC/POPC-OOH mixtures

We performed Langmuir isotherms on pure POPC, pure POPC-OOH and mixtures of these two molecules (see Fig. 5.10). Precautions were taken in order to avoid oxidation of the monolayers exposed to laboratory air (see below). POPC-OOH shows values of area per molecule (APM) which are much larger than POPC.

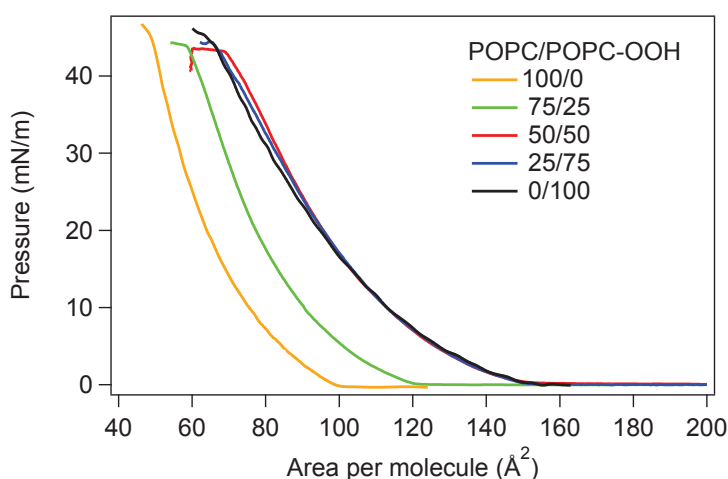


Figure 5.10: Langmuir isotherms at 20°C of monolayers made of mixtures of POPC and its hydroperoxidized form POPC-OOH.

Defining $\Delta A/A$ as:

$$\frac{\Delta A}{A} = \frac{APM_{POPC-OOH} - APM_{POPC}}{APM_{POPC}},$$

we measure $\Delta A/A \sim 50\%$, in agreement with the observations of van den Berg et al. [27] who compared PLPC monolayers with PLPC-OOH monolayers. Fig. 5.11 represents the evolution of $\Delta A/A$ as a function of the pressure Π . This relative area difference is decreasing while the pressure increases. For the maximum pressure that we can achieve, $\Delta A/A$ decreases to 27%. Thus, whatever the pressure, $\Delta A/A$ remains larger than the relative area increase measured in fully oxidized POPC bilayers ($\sim 15\%$).

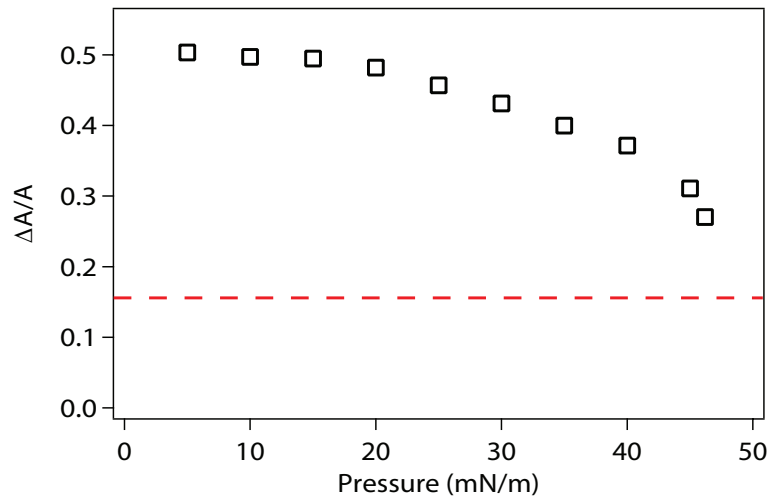


Figure 5.11: $\Delta A/A$ as a function of the pressure Π (\square). The dashed line corresponds to the relative area difference between POPC and POPC-OOH in bilayers.

It is difficult to compare results in monolayers and bilayers. Nevertheless, several studies reveal that for a certain pressure, around 30-35 mN/m, the hydration state of both monolayer and bilayer systems is identical and structural parameters of these systems are comparable [119,126]. However, depending on the properties one focuses on, the monolayer / bilayer equivalence occurs at different pressures. In the case of relative area increase between POPC and its hydroperoxidized form POPC-OOH, there is no pressure value that allows to reach the monolayer / bilayer equivalence. The use of monolayers to predict bilayer properties seems reasonable only if bilayers can be treated as two back-to-back monolayers interacting non-specifically as two slabs [127].

Another intriguing result is obtained with the mixtures isotherms (Fig. 5.10). As expected, increasing the fraction of POPC-OOH, shifts the isotherms to larger area per molecules. However for POPC-OOH fractions higher than 50 %, the isotherms saturate: further replacing a POPC by its oxidized form does not change the average area per molecule. This observation supports the view that there would be an average number of -OOH groups able to stay at the interface. Collective behavior is certainly at play here and a statistical model or numerical simulations work would be of great interest to explain these observations.

5.2.2 Lipids at air-water interface: isotherm evolution

Usually, in order to study a solvent free monolayer of phospholipids, one needs to wait a certain time for solvent evaporation before starting the compression of the film. This time delay varies in the literature from 4 to 30 minutes [128, 129], probably depending on the solvent used to prepare the lipid solution. Controversial reports on POPC monolayer isotherms under the same experimental conditions raise some questions about lipid stability at the air-water interface. We decided to further investigate this phenomenon and we thus started a preliminary study on lipid monolayer stability.

Stability of lipids

In order to study the evolution of the isotherms with time, we performed isotherm cycles, which correspond in several series of compression-extension of the lipid film. The first experiment was done on a POPC monolayer, at laboratory air and with a Langmuir trough thermalized at 20°C, by compressing the film until a maximum pressure $\Pi = 20$ mN/m to stay far from the monolayer collapse and thus avoid material loss in the water subphase. Fig. 5.12 shows the evolution of such a monolayer as a function of cycle number. One can notice that the isotherm is shifted to the larger area per molecules and that its shape is changing with time. Such a shift can be explained either by creation of matter or external pollution depositing on the interface, or by the modification of the molecules which are already present at the interface. Another striking fact is that the evolution saturates after a certain time, strongly supporting the last hypothesis. The saturation takes place for an area increase per lipid of about 20 % at $\Pi = 20$ mN/m.

In order to rule out the first possibility and to confirm the last one, we performed

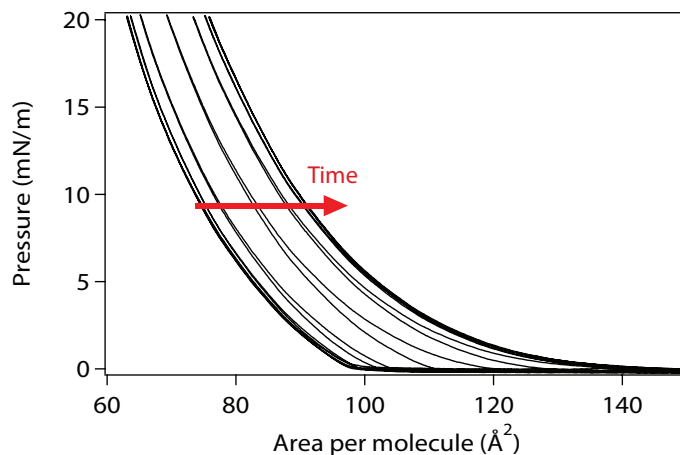


Figure 5.12: Isotherm cycles of a pure POPC monolayer. The isotherm is shifted to higher area per molecules as a function of the time. A saturation is observed after a time $t \sim 230$ min.

the same experiments with DSPC, a saturated lipid with chains of 18 carbons and the synthesized molecule POPC-OOH (see Appendix A.2.2) that we already used in the previous studies. The cycles were comparable for these two molecules and superposed perfectly (data not shown). In order to simplify the representation, we display evolution of the area per molecule for a pressure of 20 mN/m in Fig. 5.13. The curves show a small drift to lower area per molecule, which is a typical signature of the trough used for the study. This drift is also present for POPC, but hidden by the area increase.

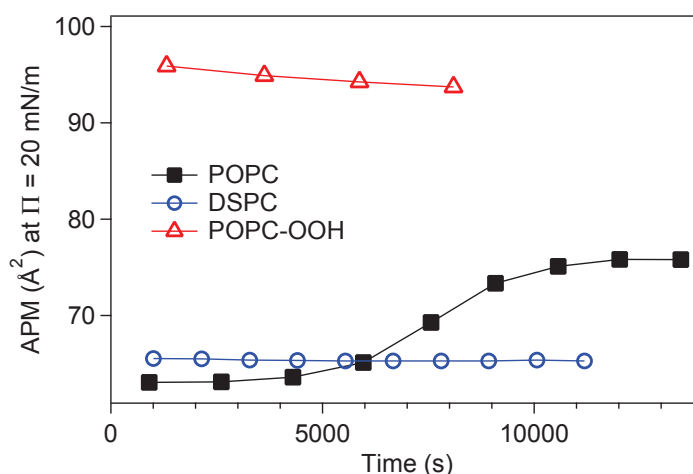


Figure 5.13: Area per molecule for $\Pi = 20$ mN/m as a function of time for POPC (■), DSPC (○) and POPC-OOH (△).

As saturated lipids and already oxidized lipids show no change, these observations argue strongly for lipid oxidation while exposed at laboratory air. The kinetic of the modification changes slightly from a day to another, depending probably on the air quality.

Controlled atmospheres

We performed the same experiments under controlled atmospheres in order to find out which compound present in the air is responsible for this oxidation. Fig. 5.14 shows the results obtained by performing the same cycles in atmospheres of N_2 and O_3 . One can easily notice that under nitrogen atmosphere no shift of the curves is observed. However, in an ozone atmosphere, the isotherm shifts to the larger area per molecule and saturates strikingly at the same values that for laboratory air. The isotherms of oxidized monolayers under laboratory air and ozone show exactly the same behavior and superpose perfectly, strongly supporting the sens that lipid oxidation takes place by an oxidative species present in the air. The area increase, which can be extrapolated by taking into account a linear drift for the experiment under ozone atmosphere, gives a value of about 21 % at $\Pi = 20$ mN/m. This value is much lower than the difference between POPC and POPC-OOH discussed above, showing that hydroperoxidation, if present, might not be the only process at play; formation of cleaved lipids, like aldehydes or acids [51,53] might also take place.

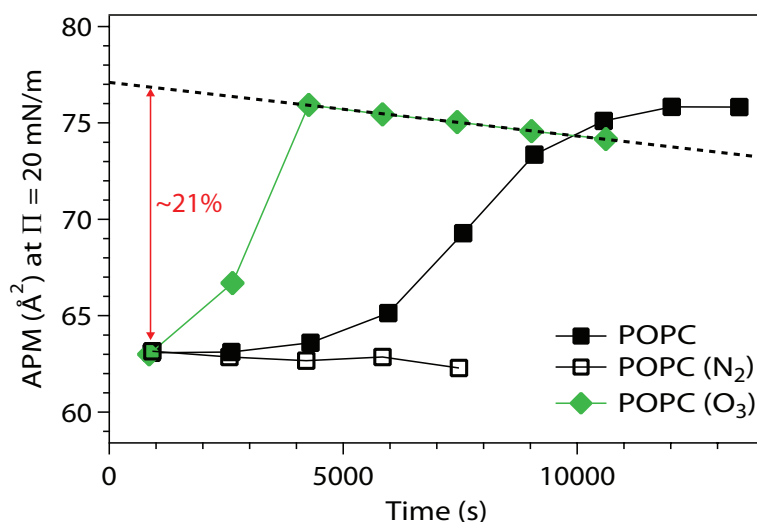


Figure 5.14: Area per molecule for $\Pi = 20$ mN/m as a function of time for POPC under different atmospheres: normal laboratory air (\blacksquare), O_3 (\blacklozenge) and N_2 (\square).

Using an ozone detector, the measured ozone concentration in the laboratory air was typically in the order of magnitude of the values measured by the ASPA (a public agency for air quality control) in Strasbourg Nord, $[O_3] < 0.050$ ppm. In comparison, we measured an ozone concentration of several ppm for our experiment under ozone atmosphere. Thus, the increased kinetics in Fig. 5.14 for the oxidation are in agreement with a higher ozone concentration. Besides, the same saturation value obtained in both cases strongly argues for ozone induced oxidation. However, a complete laboratory air analysis would be necessary to be sure that other species are not competing as well in the oxidation process.

DOPC: A special case

As already evoked in the work of Liljeblad et al. [59], DOPC monolayers are not stable at the water-air interface. Indeed, Fig. 5.15 shows an isotherm cycle for DOPC under laboratory air. The isotherms shift to smaller area per molecule, confirming that DOPC leaves the interface. One can also notice a change in the isotherm shape. We repeated the experiment under an enriched nitrogen atmosphere, which slowed down the process. However, no quantitative study of this slowdown has been performed yet. The inset of Fig. 5.15 shows the kinetics of the area per lipid for $\Pi = 20$ mN/m under laboratory air and N_2 .

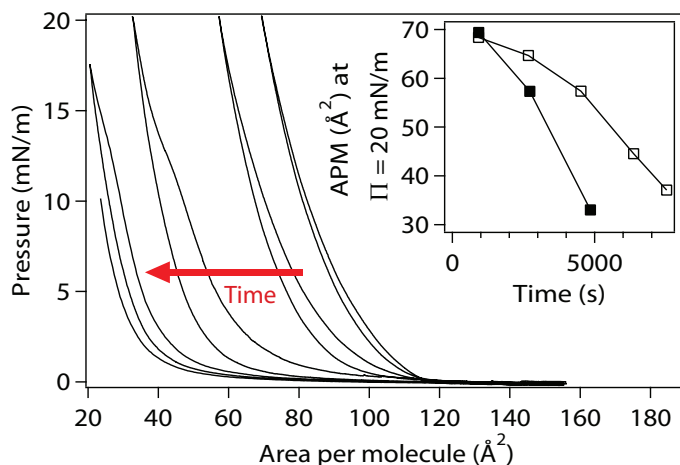


Figure 5.15: Isotherm cycles of a pure DOPC monolayer. The isotherm is shifted to lower area per molecules as a function of the time. The inset shows the evolution of the area per molecule for $\Pi = 20$ mN/m as a function of time for DOPC under different atmospheres: normal laboratory air (■) and N_2 (□).

5.2.3 Conclusion

We compared in this part the average area per molecule in monolayers of POPC and its oxidized form POPC-OOH. The relative area difference revealed values much larger than the ones obtained in bilayers, independently of the pressure Π . An interesting behavior of mixtures of these two species has been observed in monolayers. Apparently, there is a maximum number of -OOH groups able to stay at the interface. This observation can be related to our measurement of area increase in DOPC bilayers versus POPC bilayers for full oxidation: though DOPC has two unsaturations, its area increase is far from the double value of POPC. A common answer to the two observations might therefore be that not all hydroxyl groups are able to seat at the interface.

We also studied the stability of unsaturated lipids on the water-air interface. This stability is fast compromised for both POPC and DOPC, which are rapidly oxidized under laboratory air. By comparing the area per molecule of the oxidation products for POPC, one can notice that they do not correspond to POPC-OOH and probably correspond to cleaved lipids, according to literature. However, oxidized forms of POPC stay at the interface. In the case of DOPC, oxidation and probable cleavage of the two chains induces a loss of DOPC from the interface.

General conclusion

We studied in this work the oxidation effect of the new hydrophobically modified photosensitizer Chlorin-12 that anchors in phospholipid membranes. The molecule was designed to avoid π -stacking and therefore to allow the incorporation in the membrane without any aggregation. Its photobleaching behavior is nevertheless complex, and it appears that a conformational or chemical modification happens under light irradiation. We analyzed this modification by following the absorption and emission spectra, where its main light absorption and its fluorescence emission peaks are slightly shifted to higher energies. However, the fluorescence and singlet oxygen quantum yields appear to stay constant upon this modification. At high Chlorin-12 contents, some quenching effects appear, that we tried to explain using two different models: trivial light re-absorption and dipole/dipole energy transfer. The first one shows a good agreement with our observations, however supplementary experiments on fluorescence anisotropy would be required for confirmation.

Giant Unilamellar Vesicles (GUVs), that can be directly imaged and manipulated under an optical microscope, have developed as valuable biomimetic tools to study the photophysical and photochemical factors controlling the uptake of photosensitizers in lipid membranes and the related modifications induced by $^1\text{O}_2$ oxidation.

Anchoring of the photosensitizer seems to avoid any reaction between its excited triplet state and the unsaturations present in the lipid chains, favoring then only “clean” reactions of $^1\text{O}_2$ on carbon-carbon double bonds. This will exclusively lead to phospholipid hydroperoxidation, avoiding the cleavage of the lipid chains and other oxidation by-products. Singlet oxygens are generated in the close vicinity of the bilayer, from where they start a random trajectory that penetrates the bilayer with probability close to unit. Their chances to react with a double bond before they decay are high, leading to the formation of a -OOH group at position 9 or 10 along the unsaturated chain. The hydrophilic character of the -OOH group increases its probability to seat at the lipid-water interface, and provides thus a driving force that

changes the average chain conformation and the hydrophobic nature of the lipid-water interface. The resulting changes in chain conformation induce an increase of the lipid molecular area of ~15 % for POPC and ~19 % for DOPC. In spite of the modifications of the lipid molecular structure, the self-assembled bilayer is not destroyed, it retains instead its integrity and its impermeability with respect to sucrose or to glucose.

We show that the relative changes in the lipid molecular area can be directly correlated with singlet oxygen generation, thus allowing an in situ measurement of the efficiency of the binary reaction between double bonds and $^1\text{O}_2$ species. Indeed, one out of five $^1\text{O}_2$ will react on a double bond.

The combined modifications of chain conformations and -OOH density at the lipid-water interface lead to a reduction by a factor four of the bilayer stretching modulus, an important result for discussing protein insertion in oxidized membranes and other mechanisms of cell function.

Our measurements provide a coherent and precise scenario for lipid hydroperoxidation in lipid bilayers of both POPC and DOPC and our experimental geometry for the evaluation of lipid peroxidation, based on GUVs decorated with anchored sensitizers is a flexible and quantitative tool that can address many of the open questions in this field. As a perspective, it will be able to deal with more complex and bio-relevant lipid bilayers made from lipid mixtures and proteins, a first step towards the understanding of the role of lipid oxidation in signaling cascades.

Our technique is also well adapted, for instance, to quantify the protecting role of antioxidants and to study the mechanisms by which the unsaturated bonds can be protected from a reaction with singlet oxygen. We studied in our system the effect of a well known physical quencher, sodium azide, which appeared to be completely inefficient. Its presence did not modify the photosensitizer triplet state lifetime, however $^1\text{O}_2$ lifetime was decreased as expected from the literature.

By solving the diffusion equations for $^1\text{O}_2$ inside and outside the bilayer, we could compute the $^1\text{O}_2$ concentration profiles away from the membrane. A close position of singlet oxygen creation and reaction sites explains only partly the quencher inefficiency, as azide is not present in the membrane. A complete explanation is provided by the saturation in speed of area increase at high Chlorin-12 content, hiding the protective role of azide. Complementary experiments should be done, using lower concentrations in Chlorin-12, in order to be out of the saturation regime and to quantify the protective effect of azide upon lipid peroxidation.

Finally, we studied the stability of unsaturated lipids at the water-air interface. This stability is quickly compromised for both POPC and DOPC, which are rapidly oxidized under laboratory air, explaining the controversial isotherms found in literature. By comparing the area per molecule of the oxidation products for POPC, one can notice that they do not correspond to its hydroperoxidized form and probably correspond to cleaved lipids, in agreement with literature. However, oxidized forms of POPC stay at the interface. Whereas, in the case of DOPC, oxidation and probable cleavage of the two chains induces a loss of DOPC from the interface.

The intriguing behavior of mixtures of POPC and its hydroperoxide form POPC-OOH would need a thermodynamic model or some numerical simulations work to be explained.

Appendix

A.1 Analysis of the FRAP under microscope

Let us note $\mathcal{I}_b(\mathbf{r})$ the intensity needed to achieve the photobleaching. In our case, we will first assume that the photobleaching beam is cylindrical as indicated by our profiles:

$$\begin{aligned}\mathcal{I}_b &= \mathcal{I}_0 \text{ for } |r| \leq a, \\ \mathcal{I}_b &= 0 \text{ for } |r| \geq a.\end{aligned}$$

We suppose that photobleaching leads to a fluorescent marker concentration $c(\mathbf{r}, t = 0) = c_0 e^{-K * \mathcal{I}_b}$. In order to describe the time evolution of the fluorophore concentration, we decompose the profile in Fourier series as follows:

$$c(\mathbf{r}, t = 0) = \frac{S}{(2\pi)^2} \int d^2\mathbf{q} \tilde{c}(q, t = 0) e^{j\mathbf{q}\cdot\mathbf{r}}, \quad (\text{A.3})$$

$$\tilde{c}(q, t = 0) = \frac{1}{S} \int d^2\mathbf{r} c(\mathbf{r}, t = 0) e^{-j\mathbf{q}\cdot\mathbf{r}}. \quad (\text{A.4})$$

If we assume that this concentration evolves according to the diffusion equation:

$$\frac{\partial c(\mathbf{r})}{\partial t} = D \nabla^2 c(\mathbf{r}). \quad (\text{A.5})$$

In the reciprocal space, we obtain:

$$\frac{\partial \tilde{c}(q, t)}{\partial t} = -q^2 D \tilde{c}(q, t) \quad (\text{A.6})$$

each mode q evolves with a characteristic time $\tau_q = (Dn^2q^2)^{-1}$ like:

$$\tilde{c}(q, t) = c_0 A_n(K, 0) e^{-Dn^2q^2t} \quad (\text{A.7})$$

we have then a complex concentration profile. Then, we read this signal with a reading signal \mathcal{I}_ℓ . We can calculate the fluorescence profile, assuming that it is proportional to the concentration in fluorophore and in the reading intensity:

$$F(\mathbf{r}, t) \propto c(r, t) \mathcal{I}(r). \quad (\text{A.8})$$

Finally, we will assume that the reading beam is constant in the photobleached region (diaphragm totally open).

We start to calculate the FT of the concentration profile:

$$\begin{aligned} c(r, t = 0) &= c_0 e^{-K\mathcal{I}_0} \text{ for } |r| \leq a, \\ c(r, t = 0) &= c_0 \text{ for } |r| \geq a, \end{aligned}$$

that writes:

$$\begin{aligned} c(q, t = 0) &= \frac{1}{S} \int_0^{+\infty} r dr \int_{-\pi}^{\pi} d\theta c(r, t = 0) e^{-jqr \cos \theta} \\ &= \frac{2\pi c_0 a}{Sq} (1 - e^{-K\mathcal{I}_0}) J_1(qa) \end{aligned} \quad (\text{A.9})$$

where J_0 and J_1 are the 0th and 1st order Bessel functions.

If we now calculate the fluorescence intensity in $r = 0$, we have:

$$\begin{aligned} F(r = 0, t) &= c(r = 0, t) \mathcal{I}_{\ell,0} \\ \frac{F(r = 0, t)}{\mathcal{I}_{\ell,0} c_0 (1 - e^{-K\mathcal{I}_0})} &= \int_0^{+\infty} J_1(x) e^{-\frac{Dt}{a^2} x^2} dx. \end{aligned} \quad (\text{A.10})$$

We can then plot that curve and compare it to experimental data to get D .

A.2 Synthesized molecules

A.2.1 Photosensitizer

Synthesis and characterization

The photosensitizer Chlorin-12 was synthesized with protoporphyrin IX diester (42.3 mmol) and excess of 4-dodecylphenyl maleimide, by Diels-Alder reactions according to the procedure described in the literature. It was purified using column chromatography (silica) followed by preparative TLC (silica), using a 50:1 mixture of $\text{CHCl}_3/\text{AcOEt}$ as eluant, which furnished two pure isomers. The two isomers have a R_f of 0.55 and 0.68, the combined product of both isomers yield 72% (29.6 mmol). The compound that we named Chlorin-12 was the second of the isomers characterized by $^1\text{H-NMR}$, COSY, ESI-MS and UV-Vis.

ESI-MS-TOF, m/z 933.5321 calculated for $\text{C}_{58}\text{H}_{70}\text{N}_5\text{O}_6^+(\text{MH}^+)$; found 933.5329

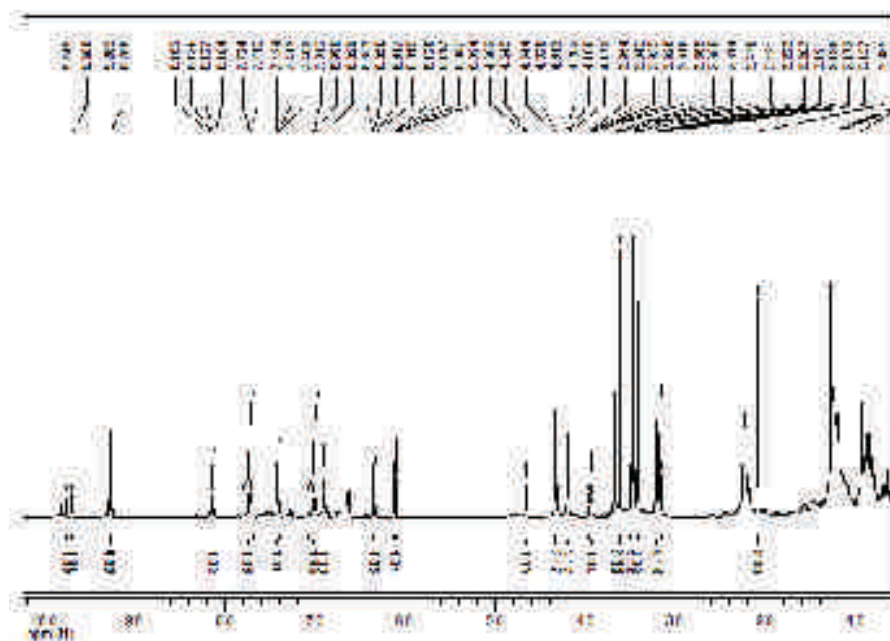


Figure A.16: $^1\text{H-NMR}$ (500 MHz) in CDCl_3 of Chlorin-12.

$2^1,2^2$ [*N,N*-dicarbonyl-*N*-(4-dodecylphenyl)]-8,12-bis[2-(methoxycarbonyl)ethyl]-2,7,13,17-tetramethyl-18-vinyl-2,2¹,2²,2³-tetrahydrobenzo[*b*]porphyrin. ^1H NMR (CDCl_3 , 500 MHz), δ (ppm): -2.45 (br s, 2H, H-21 and H-23); 0.9-1.27 (m,

p-alkyl group); 2.08 (s, 3H, CH₃-2⁵), 3.17 (t, 2H, $J = 8.0$ Hz, H-12²), 3.21 (t, 2H, $J = 8.0$ Hz, H-8²); 3.42 (s, 3H, CH₃-13¹); 3.47 (s, 3H, CH₃-7¹); 3.45-3.48 (m, 2H, H-2^{3 α} and H-2^{3 β}); 3.61 (s, 3H, CH₃-17¹), 3.91-3.95 (m, 1H, H-2²) 3.65 and (s, 3H, 12⁴); 3.66(s, 3H, 8⁴);4.18 (t, 2H, $J = 8.0$ Hz, H-12¹); 4.32 (t, 2H, $J = 8.0$ Hz, H-8¹); 4.65 (d, 1H, $J = 8.5$ Hz, H-2¹); 6.10 (dd, 1H, $J = 11.5$ and 1.5 Hz, H-18^{2 α}); 6.33 (dd, 1H, $J = 18.0$ and 1.5 Hz, H-18^{2 β}); 6.99-7.01 (m, 2H, H-2⁹ and 2¹³); 7.41 (t, $J = 5.0$ Hz, 1H, H-2⁴); 7.73-7.70 (m, 2H, H-2¹⁰ and H-2¹²); 8.13 (dd, 1H, $J = 18.0$ and 11.5 Hz, H-18¹); 9.26 (s, 1H, H-5); 9.28 (s, 1H, H-20); 9.68 (s, 1H, H-10), 9.74 (s, 1H, H-15).

Quantum yield determination

The detection of the near infrared emission of the singlet oxygen molecule at 1270 nm is a standard method to determine ¹O₂ quantum yield ϕ_{Δ} . Both the liposomes solution and the acetonitrile solution of Chlorin-12 that was used as a standard ($\phi_{\Delta} = 0.7$), exhibit an absorbance value close to 0.02 (1 cm path length) at 640 nm. A Continuum Surelite III Nd:YAG laser was used as the excitation source operating at 532 nm (5 ns, 10 Hz) to pump a dye laser (DCM 2-(2-(4-(dimethylamino)phenyl)-6-methyl-4H-pyran-4-ylidene)-propanedinitrile in ethanol) emitting at 640 nm. The singlet oxygen emission at 1270 nm was detected at right angle by a liquid nitrogen cooled photomultiplier (Hamamatsu R5509). The value $\phi_{\Delta} = 0.63$ was calculated by measuring and comparing the emissions of sample and standard, correcting also for the refraction index differences (acetonitrile 1.344, deuterium oxide 1.328) and for the ¹O₂ lifetimes (acetonitrile 60 μ s, liposomes in deuterium oxide 16 μ s) [41].

Laser Flash Photolysis

Laser flash photolysis data were obtained with an applied photophysics system composed of a Nd:YAG laser (Spectron Laser System, Warwickshire, UK), operating at 355 nm, delivering pulses with ~ 30 mJ/pulse and ~ 10 ns (full width at half maximum), and a pulsed 150 W Xe lamp. Control electronics and a Hewlett-Packard model 54510B digitizing oscilloscope interfaced to a PC were used for data capture.

A.2.2 Hydroperoxidized lipid POPC-OOH

The hydroperoxide form of POPC, that we designate by POPC-OOH, was produced through irradiation of POPC in a methylene blue (MB) solution as follows. 80 mg of POPC was dissolved in 5 mL of chloroform, to which one added 1 mL of a 0.3 mM methanol solution of MB. This mixture was kept in an ice bath and stirred continuously. The irradiation was performed with a tungsten lamp (500 W) for 8h. The mixture of solvent was evaporated and 1 mL of methanol HPLC grade was added. The products were separated and analyzed in a HPLC-MS system consisting of shim-pack prep ODS column (150 x 4.6 mm, 5 mm), coupled to an Esquire ESI-MS spectrometer. The product that was characterized as POPC hydroperoxide was eluted during 7 min in a 1 mL/min flux and resulted in a m/z 792.7.

A.3 Microscope filters

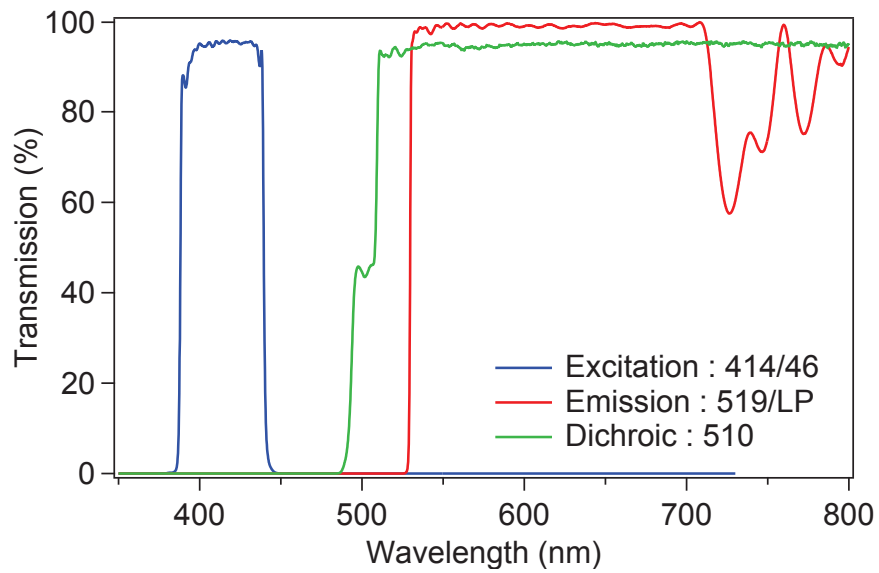


Figure A.17: Fluorescence filters used in all the experiments.

A.4 Vesicles formation

A.4.1 GUV electroformation

A well known technique to prepare a large amount of GUVs is the electroformation method [84]. GUVs of POPC and DOPC containing different molar fractions x_{Ch} of Chlorin-12 in the range [0.0003-0.02], were grown using this method. Briefly, 5 μ L of a 1 mg/mL lipid/Chlorin-12 chloroform solution were spread and dried on the surfaces of two conductive glasses coated with Indium Tin Oxide (ITO), which were then separated by a 2 mm thick Sigillum wax frame (Vitrex, Denmark) with their conductive sides facing each other. This electroswelling chamber was filled with 0.1 M sucrose solution and connected to an alternating power generator at 1 V with a 10 Hz frequency for 4 h.

The vesicle solution was removed from the chamber and diluted 5 times into a 0.1 M glucose solution. This created a sugar asymmetry between the interior and the exterior of the vesicles. The osmolarities of the sucrose and glucose solutions were measured with a cryoscopic osmometer Osmomat 030 (Gonotec, Berlin, Germany) and carefully matched to avoid osmotic pressure effects. The vesicle solution was placed in an observation chamber.

A.4.2 Liposome extrusion

POPC liposomes (SUVs) containing Chlorin-12 were prepared as follows. The two components were first diluted at the desired composition in chloroform, then spread onto a test tube. After letting the solvent evaporate, the film was hydrated in H₂O or D₂O, depending on the experiment. The resulting opalescent solution was extruded through a 100 nm pore diameter membrane (Avanti Lipids, USA), leading to a clear solution that was studied with dynamic light scattering. The results exhibited a narrow hydrodynamic radius of 100 nm for the liposomes in the solution.

Bibliography

- [1] Ames BN, Shigenaga MK, Hagen TM (1993) Oxidants, antioxidants, and the degenerative diseases of aging. *Proc Natl Acad Sci U S A* 90:7915–22.
- [2] Halliwell B, Gutteridge JMC (2007) *Free radicals in biology and medicine* (Oxford University Press, Oxford), 4th ed edition.
- [3] Crockett EL (2008) The cold but not hard fats in ectotherms: consequences of lipid restructuring on susceptibility of biological membranes to peroxidation, a review. *J Comp Physiol B* 178:795–809.
- [4] Deigner HP, Hermetter A (2008) Oxidized phospholipids: emerging lipid mediators in pathophysiology. *Curr Opin Lipidol* 19:289–94.
- [5] Sohal RS, Weindruch R (1996) Oxidative stress, caloric restriction, and aging. *Science* 273:59–63.
- [6] Gomer CJ (2010) *Photodynamic therapy: methods and protocols*, Methods in molecular biology (Springer, New York) Vol. 7651, 1st ed edition.
- [7] Grossweiner LI, Jones LR, Grossweiner JB, Rogers BHG (2005) *The science of phototherapy: an introduction* (Springer, Dordrecht).
- [8] Ochsner M (1997) Photophysical and photobiological processes in the photodynamic therapy of tumours. *J Photochem Photobiol B* 39:1–18.
- [9] Valenzano DP (1987) Photomodification of biological membranes with emphasis on singlet oxygen mechanisms. *Photochem Photobiol* 46:147–160.
- [10] Megli FM, Sabatini K (2003) Epr studies of phospholipid bilayers after lipoperoxidation. 1. inner molecular order and fluidity gradient. *Chem Phys Lipids* 125:161–172.
- [11] Caetano W, et al. (2007) Photo-induced destruction of giant vesicles in methylene blue solutions. *Langmuir* 23:1307–1314.

- [12] Jacob RF, Mason RP (2005) Lipid peroxidation induces cholesterol domain formation in model membranes. *J Biol Chem* 280:39380–39387.
- [13] Soto-Arriaza MA, Sotomayor CP, Lissi EA (2008) Relationship between lipid peroxidation and rigidity in l-alpha-phosphatidylcholine-dppc vesicles. *J Colloid Interface Sci* 323:70–74.
- [14] Borst JW, Visser NV, Kouptsova O, Visser AJ (2000) Oxidation of unsaturated phospholipids in membrane bilayer mixtures is accompanied by membrane fluidity changes. *Biochim Biophys Acta* 1487:61–73.
- [15] Ayuyan AG, Cohen FS (2006) Lipid peroxides promote large rafts: effects of excitation of probes in fluorescence microscopy and electrochemical reactions during vesicle formation. *Biophys J* 91:2172–2183.
- [16] Heuvingh J, Bonneau S (2009) Asymmetric oxidation of giant vesicles triggers curvature-associated shape transition and permeabilization. *Biophys J* 97:2904–2912.
- [17] Uchoa A, et al. (2011) Chlorin photosensitizers sterically designed to prevent self-aggregation. *The Journal of Organic Chemistry* 76:8824–32.
- [18] Valeur B (2001) *Molecular Fluorescence: Principles and Applications*. (Wiley-VCH Verlag GmbH).
- [19] Förster T (1959) Transfer mechanisms of electronic excitation. *Disc Far. Soc.* 27:7–17.
- [20] Kuhn H, Borchert A (2002) Regulation of enzymatic lipid peroxidation: The interplay of peroxidizing and peroxide reducing enzymes. *Free Radical Biology and Medicine* 33:PII S0891–5849(02)00855–9.
- [21] Eichenberger K, Böhni P, Winterhalter KH, Kawato S, Richter C (1982) Microsomal lipid peroxidation causes an increase in the order of the membrane lipid domain. *FEBS Lett* 142:59–62.
- [22] Wratten ML, et al. (1992) Structural and dynamic effects of oxidatively modified phospholipids in unsaturated lipid membranes. *Biochemistry* 31:10901–10907.
- [23] Drobnies AE, van der Ende B, Thewalt JL, Cornell RB (1999) Ctp : phosphocholine cytidyltransferase activation by oxidized phosphatidylcholines correlates with a decrease in lipid order: A h-2 nmr analysis. *Biochemistry* 38:15606–15614.

- [24] Megli FM, Sabatini K (2003) Respiration state iv-generated ros destroy the mitochondrial bilayer packing order in vitro. an epr study. *Febs Letters* 550:185–189.
- [25] Drobnies AE, et al. (2002) Ctp : phosphocholine cytidyltransferase and protein kinase c recognize different physical features of membranes: differential responses to an oxidized phosphatidylcholine. *Biochimica Et Biophysica Acta-biomembranes* 1564:PII S0005–2736(02)00404–2.
- [26] Ricciarelli R, Zingg JM, Azzi A (2001) Vitamin e: protective role of a janus molecule. *Faseb Journal* 15:2314–2325.
- [27] van den Berg JJ, Op den Kamp JA, Lubin BH, Kuypers FA (1993) Conformational changes in oxidized phospholipids and their preferential hydrolysis by phospholipase a2: a monolayer study. *Biochemistry* 32:4962–7.
- [28] Girotti AW (1998) Lipid hydroperoxide generation, turnover, and effector action in biological systems. *J Lipid Res* 39:1529–1542.
- [29] Dougherty TJ, et al. (1978) Photoradiation therapy for the treatment of malignant tumors. *Cancer Res* 38:2628–2635.
- [30] Nseyo UO, et al. (1998) Photodynamic therapy (pdt) in the treatment of patients with resistant superficial bladder cancer: A long term experience. *Journal of Clinical Laser Medicine & Surgery* 16:61–68.
- [31] Wilson BC, Patterson MS (2008) The physics, biophysics and technology of photodynamic therapy. *Phys Med Biol* 53:R61–109.
- [32] Cruchten SV, Broeck WVD (2002) Morphological and biochemical aspects of apoptosis, oncosis and necrosis. *Anat Histol Embryol* 31:214–223.
- [33] Schmitt JM, Kumar G (1998) Optical scattering properties of soft tissue: a discrete particle model. *Applied Optics* 37:2788–2797.
- [34] Tsushima M, Tokuda K, Ohsaka T (1994) Use of hydrodynamic chronocoulometry for simultaneous determination of diffusion-coefficients and concentrations of dioxygen in various media. *Analytical Chemistry* 66:4551–4556.
- [35] Skovsen E, Snyder JW, Lambert JDC, Ogilby PR (2005) Lifetime and diffusion of singlet oxygen in a cell. *J Phys Chem B* 109:8570–8573.
- [36] Finlay J (2003) Ph.D. thesis (University of Rochester, Rochester, NY).

- [37] VanStaveren HJ, Marijnissen HPA, Aalders MCG, Star WM (1995) Construction, quality assurance and calibration of spherical isotropic fibre optic light diffusers. *Lasers In Medical Science* 10:137–147.
- [38] Diamond KR, Patterson MS, Farrell TJ (2003) Quantification of fluorophore concentration in tissue-simulating media by fluorescence measurements with a single optical fiber. *Applied Optics* 42:2436–2442.
- [39] Farrell TJ, Wilson BC, Patterson MS, Olivo MC (1998) Comparison of the in vivo photodynamic threshold dose for photofrin, mono- and tetrasulfonated aluminum phthalocyanine using a rat liver model. *Photochemistry and Photobiology* 68:394–399.
- [40] Dysart JS, Singh G, Patterson MS (2005) Calculation of singlet oxygen dose from photosensitizer fluorescence and photobleaching during mthpc photodynamic therapy of mll cells. *Photochemistry and Photobiology* 81:196–205.
- [41] Jarvi MT, Niedre MJ, Patterson MS, Wilson BC (2006) Singlet oxygen luminescence dosimetry (sold) for photodynamic therapy: Current status, challenges and future prospects. *Photochemistry and Photobiology* 82:1198–1210.
- [42] Jarvi MT, Niedre MJ, Patterson MS, Wilson BC (2011) The influence of oxygen depletion and photosensitizer triplet-state dynamics during photodynamic therapy on accurate singlet oxygen luminescence monitoring and analysis of treatment dose response. *Photochem Photobiol* 87:223–234.
- [43] Jarvi MT, Patterson MS, Wilson BC (2012) Insights into photodynamic therapy dosimetry: simultaneous singlet oxygen luminescence and photosensitizer photobleaching measurements. *Biophys J* 102:661–671.
- [44] Robertson CA, Evans DH, Abrahamse H (2009) Photodynamic therapy (pdt): a short review on cellular mechanisms and cancer research applications for pdt. *J Photochem Photobiol B* 96:1–8.
- [45] Buytaert E, Dewaele M, Agostinis P (2007) Molecular effectors of multiple cell death pathways initiated by photodynamic therapy. *Biochim Biophys Acta* 1776:86–107.
- [46] Smith G, McGimpsey WG, Lynch MC, Kochevar IE, Redmond RW (1994) An efficient oxygen independent two-photon photosensitization mechanism. *Photochem Photobiol* 59:135–139.

- [47] Khurana M, et al. (2007) Quantitative in vitro demonstration of two-photon photodynamic therapy using photofrin (r) and visudyne (r). *Photochemistry and Photobiology* 83:1441–1448.
- [48] Chen J, et al. (2004) Protease-triggered photosensitizing beacon based on singlet oxygen quenching and activation. *J Am Chem Soc* 126:11450–11451.
- [49] Geiger PG, Korytowski W, Lin F, Girotti AW (1997) Lipid peroxidation in photodynamically stressed mammalian cells: use of cholesterol hydroperoxides as mechanistic reporters. *Free Radic Biol Med* 23:57–68.
- [50] Pratt DA, Mills JH, Porter NA (2003) Theoretical calculations of carbon-oxygen bond dissociation enthalpies of peroxy radicals formed in the autoxidation of lipids. *J Am Chem Soc* 125:5801–10.
- [51] Wadia Y, Tobias DJ, Stafford R, Finlayson-Pitts BJ (2000) Real-time monitoring of the kinetics and gas-phase products of the reaction of ozone with an unsaturated phospholipid at the air-water interface. *Langmuir* 16:9321–9330.
- [52] Thompson KC, et al. (2010) Reaction of a phospholipid monolayer with gas-phase ozone at the air-water interface: measurement of surface excess and surface pressure in real time. *Langmuir* 26:17295–17303.
- [53] Lai CC, Yang SH, Finlayson-Pitts BJ (1994) Interactions of monolayers of unsaturated phosphocholines with ozone at the air-water interface. *Langmuir* 10:4637–4644.
- [54] Kerdous R, Heuvingh J, Bonneau S (2011) Photo-dynamic induction of oxidative stress within cholesterol-containing membranes: shape transitions and permeabilization. *Biochim Biophys Acta* 1808:2965–2972.
- [55] Cwiklik L, Jungwirth P (2010) Massive oxidation of phospholipid membranes leads to pore creation and bilayer disintegration. *Chemical Physics Letters* 486:99 – 103.
- [56] Wong-Ekkabut J, et al. (2007) Effect of lipid peroxidation on the properties of lipid bilayers: a molecular dynamics study. *Biophys J* 93:4225–36.
- [57] Riske KA, et al. (2009) Giant vesicles under oxydative stress induced by a membrane-anchored photosensitizer. *Biophysical Journal* 97:1362–1370.
- [58] Khandelia H, Mouritsen OG (2009) Lipid gymnastics: evidence of complete acyl chain reversal in oxidized phospholipids from molecular simulations. *Biophys J* 96:2734–2743.

- [59] Liljeblad JFD, Bulone V, Tyrode E, Rutland MW, Johnson CM (2010) Phospholipid monolayers probed by vibrational sum frequency spectroscopy: instability of unsaturated phospholipids. *Biophys J* 98:L50–L52.
- [60] Khabiri M, Roeselova M, Cwiklik L (2012) Properties of oxidized phospholipid monolayers: An atomistic molecular dynamics study. *Chemical Physics Letters* 519-520:93 – 99.
- [61] Mojzisoava H, Bonneau S, Maillard P, Berg K, Brault D (2009) Photosensitizing properties of chlorins in solution and in membrane-mimicking systems. *Photochem Photobiol Sci* 8:778–787.
- [62] Lavi A, Weitman H, Holmes RT, Smith KM, Ehrenberg B (2002) The depth of porphyrin in a membrane and the membrane's physical properties affect the photosensitizing efficiency. *Biophys J* 82:2101–2110.
- [63] Dror SB, et al. (2009) The localization and photosensitization of modified chlorin photosensitizers in artificial membranes. *Photochem Photobiol Sci* 8:354–361.
- [64] Minnes R, Weitman H, You Y, Detty MR, Ehrenberg B (2008) Dithiaporphyrin derivatives as photosensitizers in membranes and cells. *J Phys Chem B* 112:3268–3276.
- [65] Bronshtein I, et al. (2004) Porphyrin depth in lipid bilayers as determined by iodide and parallax fluorescence quenching methods and its effect on photosensitizing efficiency. *Biophys J* 87:1155–1164.
- [66] Gomes A, Fernandes E, Lima JLFC (2005) Fluorescence probes used for detection of reactive oxygen species. *J Biochem Biophys Methods* 65:45–80.
- [67] Haluska CK, et al. (2011) Photo-activated phase separation in giant vesicles made from different lipid mixtures. *Biochim Biophys Acta* 1818:666–672.
- [68] Pashkovskaya A, et al. (2010) Light-triggered liposomal release: membrane permeabilization by photodynamic action. *Langmuir* 26:5726–5733.
- [69] Leverett LB, Hellums JD, Alfrey CP, Lynch EC (1972) Red blood cell damage by shear stress. *Biophys J* 12:257–273.
- [70] Singer S, Nicolson G (1972) The fluid mosaic model of the structure of cell membranes. *Science* 175:720–731.

- [71] Israelachvili JN (1977) Refinement of the fluid-mosaic model of membrane structure. *Biochim Biophys Acta* 469:221–225.
- [72] Simons K, Ikonen E (1997) Functional rafts in cell membranes. *Nature* 387:569–572.
- [73] Ohvo-Rekilä H, Ramstedt B, Leppimäki P, Slotte JP (2002) Cholesterol interactions with phospholipids in membranes. *Prog Lipid Res* 41:66–97.
- [74] Simons K, Toomre D (2000) Lipid rafts and signal transduction. *Nat Rev Mol Cell Biol* 1:31–39.
- [75] Israelachvili JN (1992) *Intermolecular and Surface Forces* (Elsevier).
- [76] Tardieu A, Luzzati V, Reman FC (1973) Structure and polymorphism of the hydrocarbon chains of lipids: A study of lecithin-water phases. *J. Mol. Biol.* 75:711–718.
- [77] Woodward J, Zasadzinski J (1997) High-resolution scanning tunneling microscopy of fully hydrated ripple- phase bilayers. *Biophysical Journal* 72:964–976.
- [78] Eeman M, Deleu M (2010) From biological membranes to biomimetic model membranes. *Biotechnologie agronomie societe et environnement* 14:719–736.
- [79] Jähnig F (1996) What is the surface tension of a lipid bilayer membrane? *Biophys J* 71:1348–1349.
- [80] Richter RP, Brisson AR (2005) Following the formation of supported lipid bilayers on mica: a study combining afm, qcm-d, and ellipsometry. *Biophys J* 88:3422–3433.
- [81] Stidder B, Fragneto G, Roser SJ (2005) Effect of low amounts of cholesterol on the swelling behavior of floating bilayers. *Langmuir* 21:9187–9193.
- [82] Malaquin L, Charitat T, Daillant J (2010) Supported bilayers: combined specular and diffuse x-ray scattering. *Eur Phys J E Soft Matter* 31:285–301.
- [83] Roux D, Bellocq AM (1985) *Physics of Amphiphiles* eds edited by DeGiorgio V, Corti M (North-Holland , Amsterdam).
- [84] Angelova M, Dimitrov D (1986) Liposome electroformation. *Faraday Discussions* 81:303–11.
- [85] Quéméneur F (2010) Ph.D. thesis.

- [86] Mouritsen OG (2005) *Life - as a matter of fat: the emerging science of lipidomics* (Springer, Berlin).
- [87] Sackmann E (1995) *Handbook of Biological Physics*, eds Lipowsky R, Sackmann E (Elsevier Science B.V.), pp 213–303.
- [88] Vaz WL, Clegg RM, Hallmann D (1985) Translational diffusion of lipids in liquid crystalline phase phosphatidylcholine multibilayers. a comparison of experiment with theory. *Biochemistry* 24:781–786.
- [89] Vaz WL, Hallmann D, Clegg RM, Gambacorta A, De Rosa M (1985) A comparison of the translational diffusion of a normal and a membrane-spanning lipid in l alpha phase 1-palmitoyl-2-oleoylphosphatidylcholine bilayers. *Eur Biophys J* 12:19–24.
- [90] Schneider MB, Chan WK, Webb WW (1983) Fast diffusion along defects and corrugations in phospholipid p beta, liquid crystals. *Biophys J* 43:157–165.
- [91] Scomparin C, Lecuyer S, Ferreira M, Charitat T, Tinland B (2009) Diffusion in supported lipid bilayers: influence of substrate and preparation technique on the internal dynamics. *Eur Phys J E Soft Matter* 28:211–220.
- [92] Webb W (1976) Applications of fluorescence correlation spectroscopy. *Quarterly Reviews of Biophysics* 9:49–68.
- [93] Benda A, et al. (2003) How to determine diffusion coefficients in planar phospholipid systems by confocal fluorescence correlation spectroscopy. *Langmuir* 19:4120–4126.
- [94] Schmidt T, Schütz GJ, Baumgartner W, Gruber HJ, Schindler H (1996) Imaging of single molecule diffusion. *Proc Natl Acad Sci U S A* 93:2926–2929.
- [95] Gurtovenko AA, Onike OI, Anwar J (2008) Chemically induced phospholipid translocation across biological membranes. *Langmuir* 24:9656–9660.
- [96] Al-Abdul-Wahid MS, Evanics F, Prosser RS (2011) Dioxygen transmembrane distributions and partitioning thermodynamics in lipid bilayers and micelles. *Biochemistry* 50:3975–3983.
- [97] Olbrich K, Rawicz W, Needham D, Evans E (2000) Water permeability and mechanical strength of polyunsaturated lipid bilayers. *Biophys J* 79:321–327.
- [98] Dimova R, et al. (2006) A practical guide to giant vesicles. probing the membrane nanoregime via optical microscopy. *J Phys Condens Matter* 18:S1151–S1176.

-
- [99] Safran S (1994) *Statistical Thermodynamics of Surfaces, Interfaces and Membranes* (Addison-Wesley, Reading, MA).
- [100] Helfrich W (1973) Elastic properties of lipid bilayers: Theory and possible experiments. *Zeitschrift für Naturforschung* 28C:693.
- [101] Canham PB (1970) The minimum energy of bending as a possible explanation of the biconcave shape of the human red blood cell. *J Theor Biol* 26:61–81.
- [102] Helfrich W, Servuss RM (1984) Undulations, steric interactions and cohesion of fluid membranes. *Nuovo Cimento D* 3:137.
- [103] Staykova M, Holmes DP, Read C, Stone HA (2011) Mechanics of surface area regulation in cells examined with confined lipid membranes. *Proc Natl Acad Sci U S A* 108:9084–9088.
- [104] Pécrciaux J, Döbereiner HG, Prost J, Joanny JF, Bassereau P (2004) Refined contour analysis of giant unilamellar vesicles. *Eur Phys J E Soft Matter* 13:277–290.
- [105] Evans, Rawicz (1990) Entropy-driven tension and bending elasticity in condensed-fluid membranes. *Phys Rev Lett* 64:2094–2097.
- [106] Rawicz W, Olbrich K, McIntosh T, Needham D, Evans E (2000) Effect of chain length and unsaturation on elasticity of lipid bilayers. *Biophys J* 79:328–339.
- [107] Hatchard CG, Parker CA (1956) A new sensitive chemical actinometer. ii. potassium ferrioxalate as a standard chemical actinometer. *Proceedings of the Royal Society of London. Series A. Mathematical and Physical Sciences* 235:518–536.
- [108] Mertins O, da Silveira NP, Pohlmann AR, Schröder AP, Marques CM (2009) Electroformation of giant vesicles from an inverse phase precursor. *Biophys J* 96:2719–26.
- [109] Busch NA, Yarmush ML, Toner M (1998) A theoretical formalism for aggregation of peroxidized lipids and plasma membrane stability during photolysis. *Biophys J* 75:2956–2970.
- [110] Hackbarth S, Schlothauer J, Preuss A, Röder B (2010) New insights to primary photodynamic effects—singlet oxygen kinetics in living cells. *J Photochem Photobiol B* 98:173–179.

- [111] Petty MC (1996) *Langmuir-Blodgett films: an introduction* (Cambridge University Press, Cambridge).
- [112] Stratton SP, Liebler DC (1997) Determination of singlet oxygen-specific versus radical-mediated lipid peroxidation in photosensitized oxidation of lipid bilayers: effect of beta-carotene and alpha-tocopherol. *Biochemistry* 36:12911–20.
- [113] Wilkinson F, Brummer J (1981) Rate constants for the decay and reactions of the lowest electronically excited singlet state of molecular oxygen in solution. *J. Phys. Chem. Ref. Data* 10:809–999.
- [114] Shaklai N, Yguerabide J, Ranney HM (1977) Interaction of hemoglobin with red blood cell membranes as shown by a fluorescent chromophore. *Biochemistry* 16:5585–5592.
- [115] Fung BK, Stryer L (1978) Surface density determination in membranes by fluorescence energy transfer. *Biochemistry* 17:5241–5248.
- [116] Fournier JB, Ajdari A, Peliti L (2001) Effective-area elasticity and tension of micromanipulated membranes. *Phys. Rev. Lett.* 86:4970–4973.
- [117] Bouvrais H, Pott T, Bagatolli LA, Ipsen JH, Méléard P (2010) Impact of membrane-anchored fluorescent probes on the mechanical properties of lipid bilayers. *Biochim Biophys Acta* 1798:1333–1337.
- [118] Landau L, Lifshitz E (1986) *Theory of Elasticity, 3rd* (Pergamon Press, Oxford, UK).
- [119] Marsh D (1996) Lateral pressure in membranes. *Biochim Biophys Acta* 1286:183–223.
- [120] Hoebeke M (1995) The importance of liposomes as models and tools in the understanding of photosensitization mechanisms. *Journal of Photochemistry and Photobiology B: Biology* 28:189–196.
- [121] Girotti AW (2001) Photosensitized oxidation of membrane lipids: reaction pathways, cytotoxic effects, and cytoprotective mechanisms. *J Photochem Photobiol B* 63:103–113.
- [122] Hall RD, Chignell CF (1987) Steady-state near-infrared detection of singlet molecular oxygen: a stern-volmer quenching experiment with sodium azide. *Photochem Photobiol* 45:459–464.

-
- [123] Lindig BA, Rodgers MAJ (1981) Rate parameters for the quenching of singlet oxygen by water-soluble and lipid-soluble substrates in aqueous and micellar systems. *Photochemistry and Photobiology* 33:627–634.
- [124] Baier J, Maier M, Engl R, Landthaler M, Bäuml W (2005) Time-resolved investigations of singlet oxygen luminescence in water, in phosphatidylcholine, and in aqueous suspensions of phosphatidylcholine or ht29 cells. *J Phys Chem B* 109:3041–3046.
- [125] Ehrenberg B, Anderson JL, Foote CS (1998) Kinetics and yield of singlet oxygen photosensitized by hypericin in organic and biological media. *Photochem Photobiol* 68:135–140.
- [126] Brewer J, Bernardino de la Serna J, Wagner K, Bagatolli LA (2010) Multiphoton excitation fluorescence microscopy in planar membrane systems. *Biochim Biophys Acta* 1798:1301–1308.
- [127] Nagle J, Tristram-Nagle S (2000) Structure of lipid bilayers. *BBA Biomembranes* 1469:159–195.
- [128] Kouzayha A, Besson F (2005) Gpi-alkaline phosphatase insertion into phosphatidylcholine monolayers: phase behavior and morphology changes. *Biochem Biophys Res Commun* 333:1315–1321.
- [129] Matti V, et al. (2001) Characterization of mixed monolayers of phosphatidylcholine and a dicationic gemini surfactant ss-1 with a langmuir balance: effects of dna. *Biophys J* 81:2135–2143.



Georges WEBER

Modifications photo-induites de membranes modèles

Résumé

Ce travail est basé sur l'intuition que seul de nouveaux systèmes biomimétiques permettant un contrôle de la localisation spatiale des phénomènes d'oxydation peuvent conduire à une compréhension profonde de l'oxydation des lipides dans les cellules eucaryotes. Nous avons donc développé un nouveau type de molécule photosensible pouvant être ancré dans des Vésicules Géantes Unilamellaires (GUVs). Nous montrons dans cette étude que, pour le cas particulier de l'hydroperoxydation, contrôler la distribution spatiale permet une sélection des réactions d'oxydation, ce qui nécessite également une adaptation des stratégies de traitement antioxydant. En association avec de nouvelles techniques pour la quantification des événements d'oxydation, ces nouveaux modèles fournissent un scénario complet des mécanismes d'hydroperoxydation, de la production des espèces réactives ($^1\text{O}_2$) aux modifications physiques et chimiques induites dans les bicouches auto-assemblées. Nous montrons que les GUVs sont capables de survivre lorsque tous les lipides sont hydroperoxydés, confirmant que l'intégrité de la membrane est conservée dans ces conditions d'oxydation. Notre expérience permet de mesurer avec une bonne précision : l'augmentation d'aire produite sous hydroperoxydation, les modifications des propriétés mécaniques de la membrane, ainsi que l'efficacité d'hydroperoxydation. Pour une compréhension approfondie, les modifications moléculaires sous oxydation ont été étudiées à l'interface eau-air en utilisant des monocouches de lipides.

Phospholipide, membrane, oxydation, micropipette, photo-thérapie

Résumé en anglais

Our contribution to research in the area of lipid oxidation in eukariotic cells is based on the central intuition that progress can only be achieved in new biomimetic membrane systems where the spatial localization of the oxidation events might be controlled and monitored. Accordingly, we have developed new photosensitizer agents that can be anchored in Giant Unilamellar Vesicles (GUVs). It is important to stress that progress in the control of the spatial distribution of oxidation allows for a selection of the oxidation pathways, as we show in this study for the particular case of hydroperoxidation, and therefore constrains anti-oxidant strategies. In association with new tools for the quantification of the oxidation events, these new models have provided a complete scenario for the hydroperoxidation mechanisms, from the production of the oxidant species ($^1\text{O}_2$) to the final chemical and physical modifications induced on the self-assembled bilayers. We report that GUVs are able to survive full hydroperoxidation, showing that membrane integrity can be preserved under these oxidation conditions. Our experimental setup allows to measure the relative area increase produced upon peroxidation, the associated change in mechanical properties of the membrane and also the hydroperoxidation efficiency, all of them with good precisions. Further insights into the molecular modifications under oxidation have been studied at the air –water interface, using lipid monolayers.

Phospholipid, membrane, oxidation, micropipette, photo-therapy